Simulation des mouvements du sol à distances locales et télésismiques en milieu hétérogène : méthode et applications

Stéphane Gaffet

OBSERVATOIRE DE GRENOBLE

ET

INSTITUT DE RECHERCHES INTERDISCIPLINAIRES DE GÉOLOGIE ET DE MÉCANIQUE

THÈSE

présentée à

L'UNIVERSITÉ JOSEPH FOURIER DE GRENOBLE

pour obtenir le grade de

DOCTEUR

Mention : PHYSIQUE

Spécialité : Géophysique

par

Stéphane GAFFET

SUJET

SIMULATION DES MOUVEMENTS DU SOL À DISTANCES RÉGIONALES ET TÉLÉSISMIQUES EN MILIEU HÉTÉROGÈNE - MÉTHODE ET APPLICATIONS -

---

Soutenue le 25 Juin 1990 devant la Commission d'Examen

MM.	M. CAMPILLO	Président
	P.-Y. BARD	Rapporteur
	B. MASSINON	Rapporteur
	M. BOUCHON	Directeur de thèse
	F. SÁNCHEZ-SESMA	Examinateur
	J. VIRIEUX	Examinateur

OBSERVATOIRE DE GRENOBLE

ET

INSTITUT DE RECHERCHES INTERDISCIPLINAIRES DE GÉOLOGIE ET DE MÉCANIQUE

THÈSE

présentée à

L'UNIVERSITÉ JOSEPH FOURIER
DE GRENOBLE

pour obtenir le grade de

DOCTEUR

Mention : PHYSIQUE

Spécialité : Géophysique

par

Stéphane GAFFET

SUJET

SIMULATION DES MOUVEMENTS DU SOL À DISTANCES RÉGIONALES ET TÉLÉSISMIQUES EN MILIEU HÉTÉROGÈNE - MÉTHODE ET APPLICATIONS -

---

Soutenue le 25 Juin 1990 devant la Commission d'Examen

MM.	M. CAMPILLO	Président
	P.-Y. BARD	Rapporteur
	B. MASSINON	Rapporteur
	M. BOUCHON	Directeur de thèse
	F. SÁNCHEZ-SESMA	Examinateur
	J. VIRIEUX	Examinateur

A Sophie,

Quelques critiques qui n'étaient pas une troupe immense m'ont beaucoup aidé; c'est à eux que vont mes remerciements:

tout particulièrement à Michel Bouchon, qui a su m'encourager, me conseiller, et qui m'a guidé au cours de ce travail,

à Guy Perrier, à Bernard Massinon, sans qui la réalisation de cette thèse n'aurait pas été possible, et pour leur confiance lorsqu'ils m'ont acceuilli dans leurs laboratoires,

à Jean-Louis Plantet, à Michel Campillo, pour les discussions fructueuses que nous avons eues,

à Fransisco Sánchez-Sesma, à Jean Virieux, et à Pierre-Yves Bard pour l'honneur qu'ils me font d'être dans mon jury.

Je remercie l'équipe de sismologie qui à l'I.R.I.G.M. m'a permis de faire nombre de calculs sur le CRAY-2 du C.C.V.R., calculs sans lesquels une part de ce travail ne serait pas. Enfin, je remercie tous ceux que j'ai oubliés et qui se reconnaîtront parmi les critiques.

" *Faute de soleil, sache mûrir dans la glace* "

H. Michaux

Table des matières

• I - Introduction générale •

IV • *Source location and valley shape effects on the P-SV near displacement field using a boundary integral equation-discrete wavenumber representation method.*

V • *Far field effects due to geological structures located in the vicinity of buried explosions.*

• Perspectives •

I - Introduction générale

La modélisation, en tant que moyen d'isoler formes et structures des milieux de propagation réels pour en décrire la contribution dans les signaux reçus à quelques dizaines et quelques milliers de kilomètres de la source, permet d'ajuster avec toujours plus de précision les simulations numériques aux faits réels. Les modèles utilisés s'affinent à mesure des possibilités de résolution des méthodes numériques, possibilités qui vont de pair avec la puissance toujours accrue des calculateurs. Les méthodes de modélisation des signaux sismiques sont des outils devenus extrêmement puissants qui permettent de disséquer les structures pour en analyser, en comprendre et de plus en plus tendent à en prédire les effets.

Que dire du plan d'étude? Que dire des buts à atteindre? Peut-être un leitmotiv: comprendre ce que l'on observe. Les fonctions de transfert des sites où l'on reçoit et d'où sont émis les signaux sismiques prennent une grande importance lorsqu'elles viennent à modifier le contenu spectral des ondes enregistrées. Ces modifications se caractérisent essentiellement par des amplifications et des atténuations dans certaines bandes de fréquences ainsi que par la génération d'ondes diffractées par les hétérogénéités présentes dans les sites émetteurs et récepteurs. Dans le cas d'événements lointains, le contenu de l'information concernant la source peut également être modifié lors de sa propagation dans le manteau ou dans le noyau - Nous n'étudierons pas ces modifications dans la suite du travail.

Pour un mécanisme au foyer connu, les modifications d'amplitudes induites par les sites émetteurs et récepteurs peuvent fausser le calcul de différents paramètres qui concernent la source (*e.g.* dimensions, moment sismique, fonction source). On a alors recours, lorsqu'elles sont disponibles, aux informations de plusieurs capteurs sur un large éventail de distances et d'azimuts, espérant avoir statistiquement une meilleure estimation des paramètres - Nous déterminerons dans le cas de sources isotropes vues en champ télésismique un ordre de grandeur des variations d'amplitudes et leurs conséquences sur la détermination des paramètres qui quantifient ces sources.

Si les modifications d'amplitudes du champ incident sont importantes pour la connaissance de la source, la diffraction du champ incident peut générer un deuxième champ d'ondes dont la principale caractéristique est une longue durée associée à de fortes accélérations, cocktail qui peut devenir extrêmement meurtrier (Mexico, le 19 Septembre 1985; San Salvador, le 10 Octobre 1986) - Le travail présenté ici apportera un certain nombre d'éléments pour la compréhension de ces phénomènes.

Le plan d'étude comporte deux parties imbriquées. La première consiste à développer des méthodes de calcul de sismogrammes synthétiques pour des milieux de propagation latéralement hétérogènes. Le point de départ des méthodes décrites est la formulation donnée par Bouchon et Aki (1977) des potentiels de déplacements décrits par Lamb (1904) pour des forces appliquées dans un espace infini. Nous commencerons donc par décrire une méthode qui permet de calculer les sismogrammes pour des sources ponctuelles placées dans un milieu homogène et élastique à deux dimensions dont la surface est irrégulière. Cette méthode sera décrite au chapitre II dans le cas *P-SV*. La deuxième méthode sera décrite dans le cas *SH* au chapitre III et dans le cas *P-SV* au chapitre IV pour le calcul de sismogrammes synthétiques dans des milieux à stratifications non planes et pour des bassins dont le remplissage sédimentaire est irrégulier. Cette deuxième formulation sera utilisée en parallèle avec le théorème de réciprocité au chapitre V pour évaluer l'apport de la diffraction aux alentours de la source dans les sismogrammes observés à distances télésismiques.

En appliquant ces méthodes, la deuxième partie explore par simulation les effets de la diffraction dans une bande de fréquences allant jusqu'à *5* Hz pour des signaux d'une durée de quelques secondes. Cette exploration décrit une série de phénomènes à prendre en compte pour expliquer certaines amplifications et certaines formes de sismogrammes. Pour des distances d'observation de l'ordre d'une dizaine de kilomètres, nous analyserons les variations du champ de déplacement dues aux irrégularités de la topographie aux alentours des capteurs. Ceci fera l'objet du chapitre II. Ces irrégularités topographiques, que l'on appelle aussi hétérogénéités parce qu'elles perturbent ici le paysage d'un milieu idéal dont la surface serait plane, modifient, à la réception, le contenu fréquentiel des champs de déplacement issus d'événements lointains ou

d'événements proches. Les signaux provenant d'événements télésismiques sont compris comme une succession de fronts d'onde localement plans, d'incidences différentes, étant entendu que plusieurs fronts d'onde peuvent arriver simultanément - Nous étudierons plus particulièrement l'action de deux types de fronts d'onde (*i.e.* en compression et en cisaillement) incidents sur des hétérogénéités de surface, en fonction de la raideur des reliefs et de la position des stations, sur les différences d'amplifications des déplacements à la surface du sol et sur la nature des ondes qui composent ces déplacements. Le champ d'ondes émis par une source proche du récepteur est plus complexe lorsque l'on ne peut plus assimiler la source à un point. Aussi une source proche sera en première approximation considérée comme la superposition linéaire des contributions des différents points sources la constituant. Il faut alors tenir compte du diagramme de radiation de chaque point source et définir une loi de fonctionnement de ces sources primaires les unes par rapport aux autres - Nous étudierons les différentes réponses d'un relief soumis au champ de déplacement émis par une de ces sources, ponctuelle et isotrope, en l'occurence la source considérée sera une explosion.

Puis nous quitterons la surface irrégulière sur un espace homogène pour explorer différents milieux dont le sous-sol est hétérogène sous une surface plane; ceci fera l'objet des chapitres III et IV. La sélection de différents modes de propagation dans un bassin suivant le type d'onde plane qui le sollicite sera mis en évidence, l'effet de défocalisation de l'énergie sur une zone anticlinale du fond d'un bassin clairement montré ainsi que le seront l'amplification des ondes de surface et leur dispersion sur le rebord du bassin où le milieu de propagation s'amincit. Dans les chapitres précédents nous nous serons attachés à décomposer le plus possible les effets de diffraction que l'on peut rencontrer pour des événements proches du récepteur et dans un milieu hétérogène ou lors de la réception de signaux télésismiques par des stations ancrées sur des structures hétérogènes.

En éloignant le point d'observation à plusieurs milliers de kilomètres de la source, en supposant avoir un site de réception privilégié parfaitement homogène et infini (*i.e.* sans surface), les structures géologiques dans l'environnement de la source peuvent encore fortement modifier le contenu des signaux reçus à distances télésismiques. Ce sujet est développé au chapitre V - Ce chapitre étudiera plus particulièrement une série

de signaux sismiques (composante radiale) provenant de tirs nucléaires expérimentés dans la région centrale du champ de tir de Yucca Flat au Nevada et qui sont enregistrés en France. L'évolution des sismogrammes avec la complexité du milieu de tir sera décrite et nous établirons une série de corrections à apporter aux magnitudes en fonction de la localisation des explosions dans le bassin. Nous verrons ainsi l'apport de telles corrections sur l'estimation des énergies de tirs. En l'absence de valeurs connues de ces énergies, ce chapitre exposera les conséquences que peuvent avoir sur l'estimation des énergies le fait d'utiliser un événement de référence pour des tirs situés dans un milieu dont la structure est irrégulière.

- II -

Effects of two-dimensional topographies using the discrete wavenumber-boundary integral equation method in P-SV cases

Stéphane Gaffet and Michel Bouchon.

J. Acoust. Soc. Am. **85**, 2277-2283

Résumé

L'effet de la topographie sur les déplacements perçus en surface est étudié dans le cas d'ondes planes incidentes *P* ou *SV* ainsi que pour des explosions. La formulation de la méthode de discrétisation des nombres d'onde associée aux équations intégrales aux frontières est explicitée puis appliquée au problème de la diffraction de champs d'ondes élastiques par des hétérogénéités de surface. Les amplitudes du champ diffracté, essentiellement constitué d'ondes *P* de surface et d'ondes de Rayleigh, dépendent fortement de la raideur du relief. En étudiant la génération d'ondes de surface par des explosions effectuées à proximité d'une colline, nous montrons que ces ondes sont d'autant plus présentes dans les sismogrammes et d'autant plus amplifiées que les tirs sont effectués à l'intérieur du relief.

II.1 - Introduction

The diffraction of acoustic or elastic waves by an irregular topography has been studied using a variety of approaches. The complete solution for a surface of arbitrary shape has been obtained using finite-difference, finite-element methods (Boore, 1972; Smith, 1975; Ilan, 1977; Zahradnik and Urban, 1984) and boundary integral equation formulations (Wong and Jennings, 1975; Sills, 1978; Sánchez-Sesma and Rosenblueth, 1979; England *et al.* 1980; Sánchez-Sesma, 1981; Sánchez-Sesma *et al.*, 1982; Shah *et al.*, 1982; Bouchon, 1985; Kawase and Aki, 1988). One of the major problems encountered with boundary integral equation techniques is the removal of singularities which often occur when surface source distributions are used to represent the diffracted wave field (Peek and Kausel, 1983). One way to remove these singularities is to use the discrete wavenumber method (Bouchon and Aki, 1977) to evaluate the Green's functions (Bouchon, 1985; Kawase and Aki, 1988; Campillo and Bouchon, 1985; Bouchon, 1987; Campillo, 1987; Paul and Campillo, 1988). In the present work we extend the formulation previously introduced to study the scattering of *SH*-waves by an irregular topography (Bouchon, 1985), to the case of incident *P*- and *SV*-waves. We study the response of a ridge shaped topography and investigate the effect of the surface steepness on the diffracted wave field. We also consider the case of an explosion located in the vicinity of the irregular surface.

II.2 - Method

Following Helmholtz, the displacement $\vec{u}$ may be written as a derivative of a scalar potential ϕ and of a vector potential $\vec{\psi}$, representing respectively the compressional and the shear wave fields:

$$\vec{u} = \vec{\nabla}\,(\phi) + r\vec{o}t\,(\vec{\psi})$$

In a two-dimensional vertical cartesian coordinate system this relation becomes

$$u = \partial\phi / \partial x - \partial\psi / \partial z$$
$$w = \partial\phi / \partial z + \partial\psi / \partial x$$

The expressions of the compressional displacement potentials for horizontal (h) and vertical (v) line forces $Q_h.\exp(i\omega t)$ and $Q_v.\exp(i\omega t)$ acting at a point $(x_o,\ z_o)$ of an infinite homogeneous elastic space are given by Lamb (1904):

$$\phi_h\ (x, z) = \frac{Q_h.\ exp\,(i\,\omega t)}{4\pi\omega^2\rho}\ .\ \int_{-\infty}^{+\infty} \frac{k}{\nu}.\ exp\,[-i\,\nu\,|z - z_o\,|].\ exp\,[-ik\,(x - x_o)].dk$$

$$\phi_v\ (x, z) = \frac{Q_v.\ exp\,(i\,\omega t)}{4\pi\omega^2\rho}.\ sgn\,(z - z_o)\ .\ \int_{-\infty}^{+\infty} exp\,[-i\,\nu\,|z - z_o\,|].\ exp\,[-ik\,(x - x_o)].dk$$

with $\nu^2 = \omega^2/\alpha^2 - k^2$, $\gamma^2 = \omega^2/\beta^2 - k^2$, $\mathrm{Im}(\nu) \le 0$, $\mathrm{Im}(\gamma) \le 0$. $sgn\,(z - z_o) = 1$ if $z \ge z_o$, $sgn\,(z - z_o) = -1$ otherwise. ω denotes the angular frequency. α and β are the compressional and the shear wave velocities and ρ is the density. Similarly, the shear displacement potentials for horizontal (h) and vertical (v) line forces are:

$$\psi_h\ (x, z) = -\ \frac{Q_h.\ exp\,(i\,\omega t)}{4\pi\omega^2\rho}.\ sgn\,(z - z_o)\ .\ \int_{-\infty}^{+\infty} exp\,[-i\,\gamma\,|z - z_o\,|].\ exp\,[-ik\,(x - x_o)].dk$$

$$\psi_v\ (x, z) = \frac{Q_v.\ exp\,(i\,\omega t)}{4\pi\omega^2\rho}\ .\ \int_{-\infty}^{+\infty} \frac{k}{\gamma}.\ exp\,[-i\,\gamma\,|z - z_o\,|].\ exp\,[-ik\,(x - x_o)].dk$$

Rather than evaluate numerically these integrals, Bouchon and Aki (1977) introduce an horizontal spatial periodicity L, of the forces. The potentials are then multiplied by the spatial Fourier transform of the Dirac distribution $\delta_L(x)$. Thus a potential written

$$\phi\,(x,\,z) = K\,(\omega).\int_{-\infty}^{+\infty} f\,(k,\,x,\,z)\,dk\,,\ \text{becomes}$$

$$\phi\,(x,\,z) = 2\pi K\,(\omega)/L\ .\sum_{n=-\infty}^{n=+\infty} f\,(k_n,\,x,\,z),\ \text{with}\ k_n = \text{n.}2\pi/\text{L} = \text{n.}\Delta\text{k}$$

We now consider a surface s(x) periodic in x with period L and bounding an homogeneous half-space in which a source is located. We represent the elastic wave field diffracted by the surface by a force distribution applied at N = 2M + 1 points of s(x) regularly spaced at $\Delta x = L/N$ interval. This sampling results in a periodicity in the wavenumber space and restricts the wavenumber range to [-MΔk,+MΔk]. The representation of the wave field produced by this force distribution can be made as precise as desired by increasing the value of N. The displacement and stress field S(x, z) produced by the surface force distribution and by the source excitation is then

$$S\,(x,\,z) = S_o\,(x,\,z) + S_d\,(x,\,z)$$

where S_o denotes the source field excitation and S_d is the term due to the contribution of horizontal and vertical line forces $Q_m{}^h.\ exp\,(i\,\omega t)$ and $Q_m{}^v.\ exp\,(i\,\omega t)$ applied at each point $(x_m,\,z_m)$ of the surface. The amplitudes of the forces $Q_m{}^h$ and $Q_m{}^v$ are determined so that they cancel the incident normal and tangential stresses on the surface and thus realize the free stress boundary condition at each point $(x_m,\,z_m)$ of the surface. S_d derives from the potentials:

$$\phi_h\,(x,\,z) = \frac{1}{2L\,\omega^2\rho}\sum_{m=-M}^{m=+M} Q_m{}^h \sum_{n=-M}^{n=+M}\frac{k_n}{\nu_n}\,exp\,(-i\,\nu_n\,|\,z - z_m\,|)\,exp\,(-ik_n\,(x - x_m))$$

$$\phi_v\,(x,\,z) = \frac{1}{2L\,\omega^2\rho}\sum_{m=-M}^{m=+M} Q_m{}^v\ sgn\,(z - z_m)\sum_{n=-M}^{n=+M} exp\,(-i\,\nu_n\,|\,z - z_m\,|)\,exp\,(-ik_n\,(x - x_m))$$

$$\psi_h\,(x,\,z) = \frac{-1}{2L\,\omega^2\rho}\sum_{m=-M}^{m=+M} Q_m{}^h\ sgn\,(z - z_m)\sum_{n=-M}^{n=+M} exp\,(-i\,\gamma_n\,|\,z - z_m\,|)\,exp\,(-ik_n\,(x - x_m))$$

$$\psi_v\,(x,\,z) = \frac{1}{2L\,\omega^2\rho}\sum_{m=-M}^{m=+M} Q_m{}^v \sum_{n=-M}^{n=+M}\frac{k_n}{\gamma_n}\,exp\,(-i\,\gamma_n\,|\,z - z_m\,|)\,exp\,(-ik_n\,(x - x_m))$$

The displacement at any point of the surface or of the half space is given by

$$u\ (x, z) = \partial(\phi_h + \phi_v) / \partial x - \partial(\psi_h + \psi_v) / \partial z$$

$$w\ (x, z) = \partial(\phi_h + \phi_v) / \partial z + \partial(\psi_h + \psi_v) / \partial x$$

The stresses and tractions are then obtained using Hookes law.

Defining the terms

$$E_{nm}\ (z) = exp\,[-i\,\nu_n\,|\,z - z_m\,|\,]$$
$$G_{nm}\ (z) = exp\,[-i\,\gamma_n\,|\,z - z_m\,|\,]$$

$$C_{nm}\ (x) = 2.\ cos\,[k_n(x - x_m)]$$
$$S_{nm}\ (x) = -2i.\ sgn(x - x_m).\ sin\,[k_n(x - x_m)]$$

$$F_L\ (\omega) = 1/(2L\,\omega^2\rho)$$

and the components of the stress tensor

$$a_n{}^{xx} = -(\lambda + 2\mu)\ k_n{}^2 - \lambda\nu_n{}^2$$
$$a_n{}^{xz} = -2\mu\ k_n\nu_n$$
$$a_n{}^{zz} = -(\lambda + 2\mu)\ \nu_n{}^2 - \lambda k_n{}^2$$

$$b_n{}^{xx} = 2\mu\ k_n{}^2$$
$$b_n{}^{xz} = -\mu\ k_n(k_n{}^2 - \gamma_n{}^2)/\gamma_n$$
$$b_n{}^{zz} = -2\mu\ k_n{}^2$$

$$c_n{}^{xx} = -(\lambda + 2\mu)\ k_n{}^3/\nu_n - \lambda k_n\nu_n$$
$$c_n{}^{xz} = -2\mu\ k_n{}^2$$
$$c_n{}^{zz} = -(\lambda + 2\mu)\ k_n\nu_n - \lambda k_n{}^3/\nu_n$$

$$d_n{}^{xx} = -2\mu\ k_n\gamma_n$$
$$d_n{}^{xz} = \mu\ (k_n{}^2 - \gamma_n{}^2)$$
$$d_n{}^{zz} = 2\mu\ k_n\gamma_n$$

where λ and μ denote the Lamé's coefficients.

(i) The displacement at a point (x, z) due to the force distribution applied on the surface is:

$$u\ (x, z) = F_L \sum_{m=-M}^{m=+M} {Q_m}^{v} . sgn(z - z_m) . \sum_{n=1}^{n=+M} S_{nm} . [-ik_n E_{nm} + ik_n G_{nm}] +$$

$$ {Q_m}^{h} . (-i\gamma_o G_{om} + \sum_{n=1}^{n=+M} C_{nm} . [-i\frac{{k_n}^2}{\nu_n} E_{nm} - i\gamma_n G_{nm}])$$

$$w\ (x, z) = F_L \sum_{m=-M}^{m=+M} {Q_m}^{v} . (-i\nu_o E_{om} + \sum_{n=1}^{n=+M} C_{nm} . [-i\nu_n E_{nm} - i\frac{{k_n}^2}{\gamma_n} G_{nm}]) +$$

$$ {Q_m}^{h} . sgn(z - z_m) . \sum_{n=1}^{n=+M} S_{nm} . [-ik_n E_{nm} + ik_n G_{nm}]$$

(ii) The components of the stress vector at a point (x, z) of a surface having a normal (n_x, n_z) are:

$$T_x\ (x, z) = F_L \sum_{m=-M}^{m=+M} {Q_m}^{v} . [n_x . (sgn(z - z_m) . [{a_o}^{xx} E_{om} + \sum_{n=1}^{n=+M} C_{nm} . ({a_n}^{xx} E_{nm} + {b_n}^{xx} G_{nm})])$$

$$+ n_z . (\sum_{n=1}^{n=+M} S_{nm} . ({a_n}^{xz} E_{nm} + {b_n}^{xz} G_{nm}))]$$

$$+ {Q_m}^{h} . [n_x . (\sum_{n=1}^{n=+M} S_{nm} . ({c_n}^{xx} E_{nm} + {d_n}^{xx} G_{nm}))$$

$$+ n_z . (sgn(z - z_m) . [{d_o}^{xz} G_{om} + \sum_{n=1}^{n=+M} C_{nm} . ({c_n}^{xz} E_{nm} + {d_n}^{xz} G_{nm})])]$$

$$T_z\ (x, z) = F_L \sum_{m=-M}^{m=+M} {Q_m}^{v} . [n_x . (\sum_{n=1}^{n=+M} S_{nm} . ({a_n}^{xz} E_{nm} + {b_n}^{xz} G_{nm}))$$

$$+ n_z . (sgn(z - z_m) . [{a_o}^{zz} E_{om} + \sum_{n=1}^{n=+M} C_{nm} . ({a_n}^{zz} E_{nm} + {b_n}^{zz} G_{nm})])]$$

$$+ {Q_m}^{h} . [n_x . (sgn(z - z_m) . [{d_o}^{xz} G_{om} + \sum_{n=1}^{n=+M} C_{nm} . ({c_n}^{xz} E_{nm} + {d_n}^{xz} G_{nm})])$$

$$+ n_z . (\sum_{n=1}^{n=+M} S_{nm} . ({c_n}^{zz} E_{nm} + {d_n}^{zz} G_{nm}))]$$

The calculation of the force amplitudes required to cancel the incident surface stress is simply done by inverting the linear square system

$$\sum_{m=-M}^{m=+M} Q_m \sum_{n=1}^{n=+M} S_m\ (x_p, z_p, k_n) = -T_o\ (x_p, z_p)$$

where p ∈ [-M, .. ,0, .. ,+M] and the point (x_p, z_p) is a sampling point of the surface. $Q_m = (Q_m{}^h, Q_m{}^v)$ and S_m is a 2-by-2 matrix deduced from the expressions of T_x and T_z.

II.3 - Applications

In all the examples considered we use the surface shape given by Sills (1978):

$$s(x) = h\ (1.0 - a)\ exp(-3a), \text{ with } a = (x/l)^2,$$

where h and l denote the height and the half width of the hill. The aim feature of this topography is its shape ratio h/l (see figure II.1). The source excitation is a vertically incident plane *P*- or *SV*-wave or an explosion with a Ricker wavelet time dependence in displacement

$$f(t) = (b - 0.5)\ exp(-b), \text{ with } b = [\pi\ (t - t_s) / t_p]^2,$$

where t_s and t_p are respectively the time of maximum amplitude and the period of the pulse. We define two characteristic dimensionless periods, $\eta_l = 2l / (ct_p)$ and $\eta_h = h / (ct_p)$ representing the ratios of the width and the height of the ridge to the incident wavelength (c is the incident wave velocity).

II.3.1 - *Tests of the method*

In order to test the accuracy of the method the results obtained in the case of a ridge topography have been compared with the calculations done by Bard (1982) for the same configuration using the Aki-Larner (1970) method. In the Aki-Larner (1970) approach, the scattered wave field is represented by a discrete superposition of downgoing plane waves. Such a description is incomplete in the depth range of surface variation but the method yields an accurate solution when the seismic wavelengths are

longer than the dimension of the irregularity. The comparison between the two methods is made for vertically incident plane *P*- and *SV*-waves and is presented in figure II.2. The parameter values used are h/l=*0.375* and η_l = *1.83*. The two sets of results obtained are in very good agreement, showing the accuracy of the two methods.

II.3.2 - *Ridge height effects*

We investigate the effect of the ridge steepness on the diffracted wave field. Three surfaces of shape ratios h/l=*0.375*, h/l=*0.5* and h/l=*0.75* are considered. The seismograms obtained are presented in figure II.3 for a vertically incident plane *P*-wave and in figure II.4 for a vertically incident plane *SV*-wave. The receivers location is shown in figure II.1. Two forms of results are presented for each shape ratio: (i) the classical seismogram representation in which the horizontal (U) and the vertical (W) ground displacement are drawn, (ii) a polarization diagram which displays the particle motion developed in the time domain (horizontal axis). The wavelengths of the incident fields have been chosen so that η_h = *0.5* in the case of an incident plane *P*-wave and η_h = *1.0* in the case of an incident plane *SV*-wave.

A sharp amplification can be observed between stations situated at the top of the ridge and those distant from the ridge. This amplification effect is more important in the case of an incident *SV*-wave as reported by Bouchon (1973) and Bard (1982). The amplitude ratio between stations "a" and "q" is then equal to *2.7* for a shape ratio h/l=*0.375* (figure II.4a), *3.1* for h/l=*0.5* (figure II.4b), and *2.4* for h/l=*0.75* (figure II.4c). For an incident *P*-wave the amplitude ratio between stations "a" and "q" increases with the steepness and is equal to *1.1* for h/l=*0.375* (figure II.3a), *1.4* for h/l=*0.5* (figure II.3b), and *2.0* for h/l=*0.75* (figure II.3c).

The diffracted field is essentially composed of the Rayleigh wave and of the surface *P*-wave. This phase whose propagation was described by Lapwood (1949) and Bouchon (1978) is more efficiently excited for small shape ratio in the case of an incident *SV*-wave (figure II.4a) and its amplitude decreases as the shape ratio increases. The amplitude of this phase is approximately the same as the Rayleigh wave amplitude for h/l=*0.375* and fits an x^{-1} decay. An incident *P*-wave also generates a surface *P*-

wave. The amplitude of this phase increases with the surface shape ratio and becomes the same as the Rayleigh wave amplitude for h/l=*0.75* (figure II.3c). The diffracted Rayleigh wave presents different features connected with the topographic shape and with the type of incident field. Its amplitude is larger in the case of an incident *P*-wave than in the case of an incident *SV*-wave. Its maximum strength is obtained for a shape ratio h/l=*0.5* when the excitation is a *P*-wave and for a ratio h/l=*0.75* when the source is a *SV*-wave.

The receivers located above the ridge display particularly complex particle motion in the case of an incident *SV*-wave on a steep ridge (see receivers "b", "c", and "d", figure II.4c). A triangular counterclockwise particle motion appears at station "b". Station "c" shows an elliptically clockwise motion which reverses to counterclockwise to initiate the Rayleigh wave. Station "d" shows a turnabout point which appears at the time of the beginning of the Rayleigh wave elliptic motion. Finally, stations "e", "f", and "g" show a wave, horizontally polarized which propagates with the *SV*-wave velocity. This phase has approximately the amplitude of the following Rayleigh wave and disappears when the distance increases. It may be interpreted as the surface *S*-wave and seems to merge rapidly with the Rayleigh wave.

II.3.3 - *Surface wave generation by an explosion*

Considering that surface waves are not generated by an explosion placed below a flat surface (figure II.6), we now study how these waves are generated by an explosion located in the vicinity of a non planar topography. We consider a surface of shape ratio h/l=*0.375* and an explosive line source placed below, at the base, and inside the ridge as depicted in figure II.5. The results are displayed in figure II.7 using the same representation as in figures II.3 and II.4. The principal effect is a strong increase in Rayleigh wave amplitude when the source is located within the ridge. This increase is accompanied by a broadening of the Rayleigh pulse, suggesting that the Rayleigh wave generation takes place over a wider area of the surface than in the case of a deeper source.

Conclusion

The discrete wavenumber-boundary integral equation method has been formulated for the case of *P*- and *SV*-waves incident on an irregular topography. For vertical incidence, the surface *P*-wave, the surface *S*-wave, and the Rayleigh wave diffracted by an elevated topography have been described in detail in correlation to the topographic shape, to the type of the incident field and to the position of the receivers. The amplification effect at the top of the ridge has been shown. For an incident *SV*-wave it appears to be important regardless of the shape ratio while in the case of an incident *P*-wave the amplification effect is negligible for a small shape ratio and increases with the shape ratio. The amplitude of the diffracted Rayleigh wave is larger in the case of an incident *P*-wave than in the case of an incident *SV*-wave. This amplitude seems to be closely dependent on the shape of the topography. Finally we have simulated the generation of surface waves by an explosive source located in the vicinity of a non planar topography.

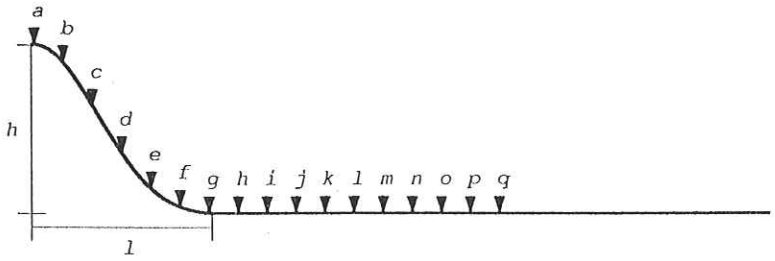

Fig. II.1 - Geometry of the topography.

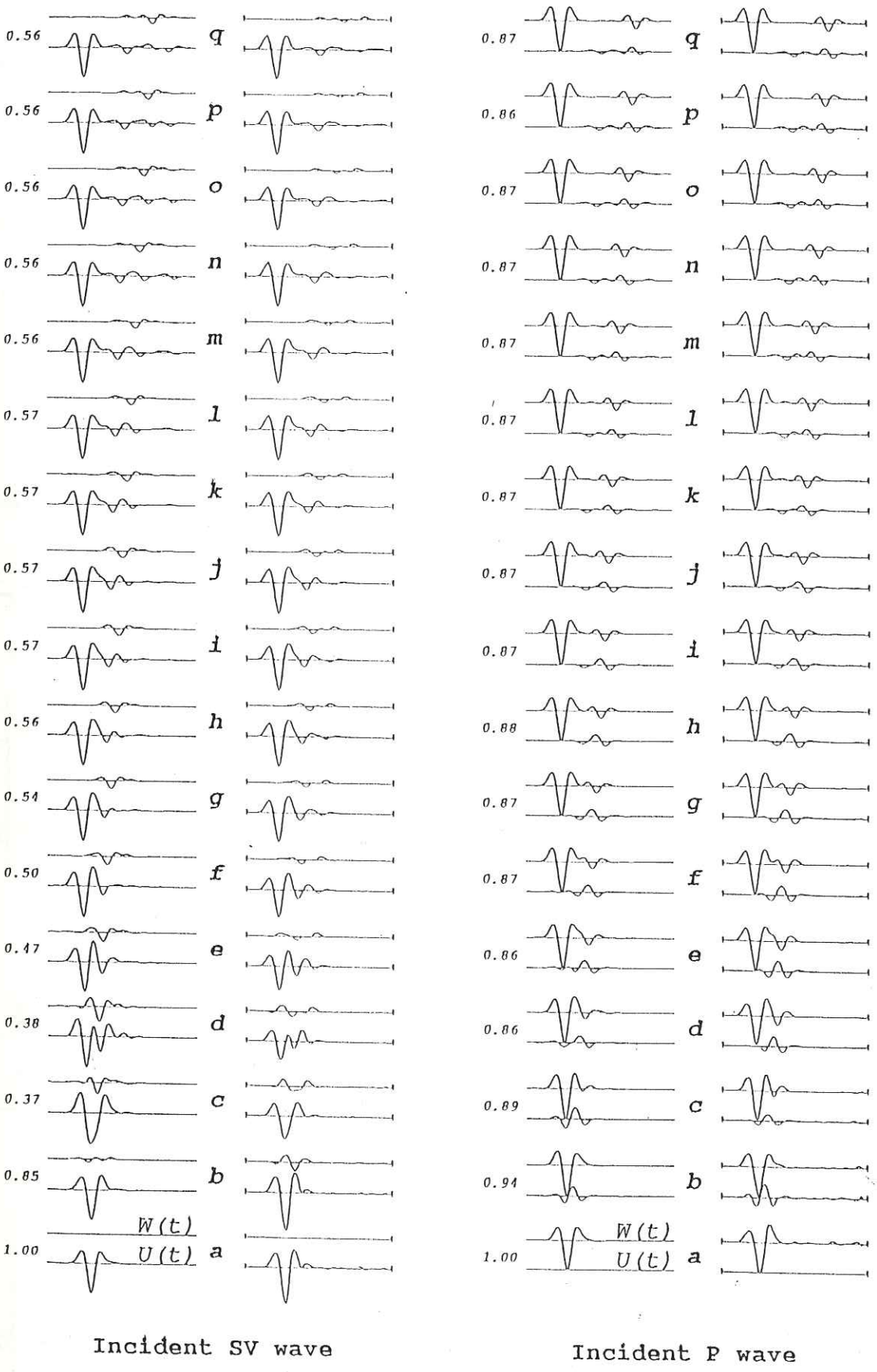

Fig. II.2 - Comparison of the results obtained by the discrete wavenumber-boundary integral equation method (left) with those obtained by Bard (1982) using the Aki-Larner (1970) method (right). The different traces represent the vertical *W(t)* and the horizontal *U(t)* displacement at the surface receivers spaced from *0* to *2.5* times the half width *l* of the ridge. The topography used is presented on the figure II.1.

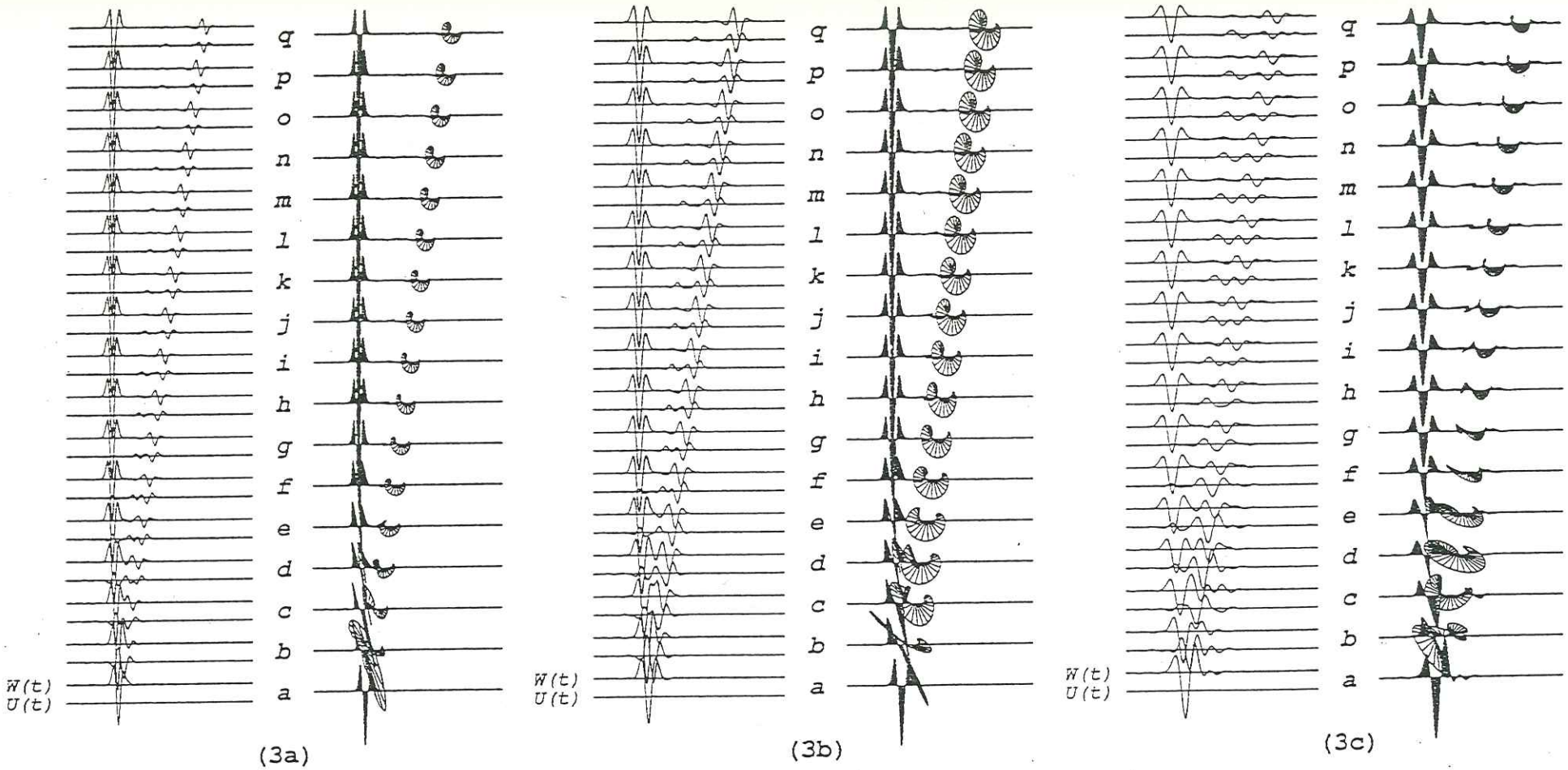

Fig. II.3 - Display of the surface motion obtained for three shape ratios h/l=*0.375* (a), h/l=*0.5* (b), and h/l=*0.75* (c). The receivers location is shown in figure II.1. The source is a vertically incident plane *P*-wave with a wavelength of λ=2h (h being the height of the ridge). The left hand side of the figures 3a, 3b, and 3c represents the horizontal (*U*) and the vertical (*W*) displacements. The time window is *3.33* s. The right hand side of these figures is a polarization plot which corresponds to a time extension of the particule motions (Explanations in text).

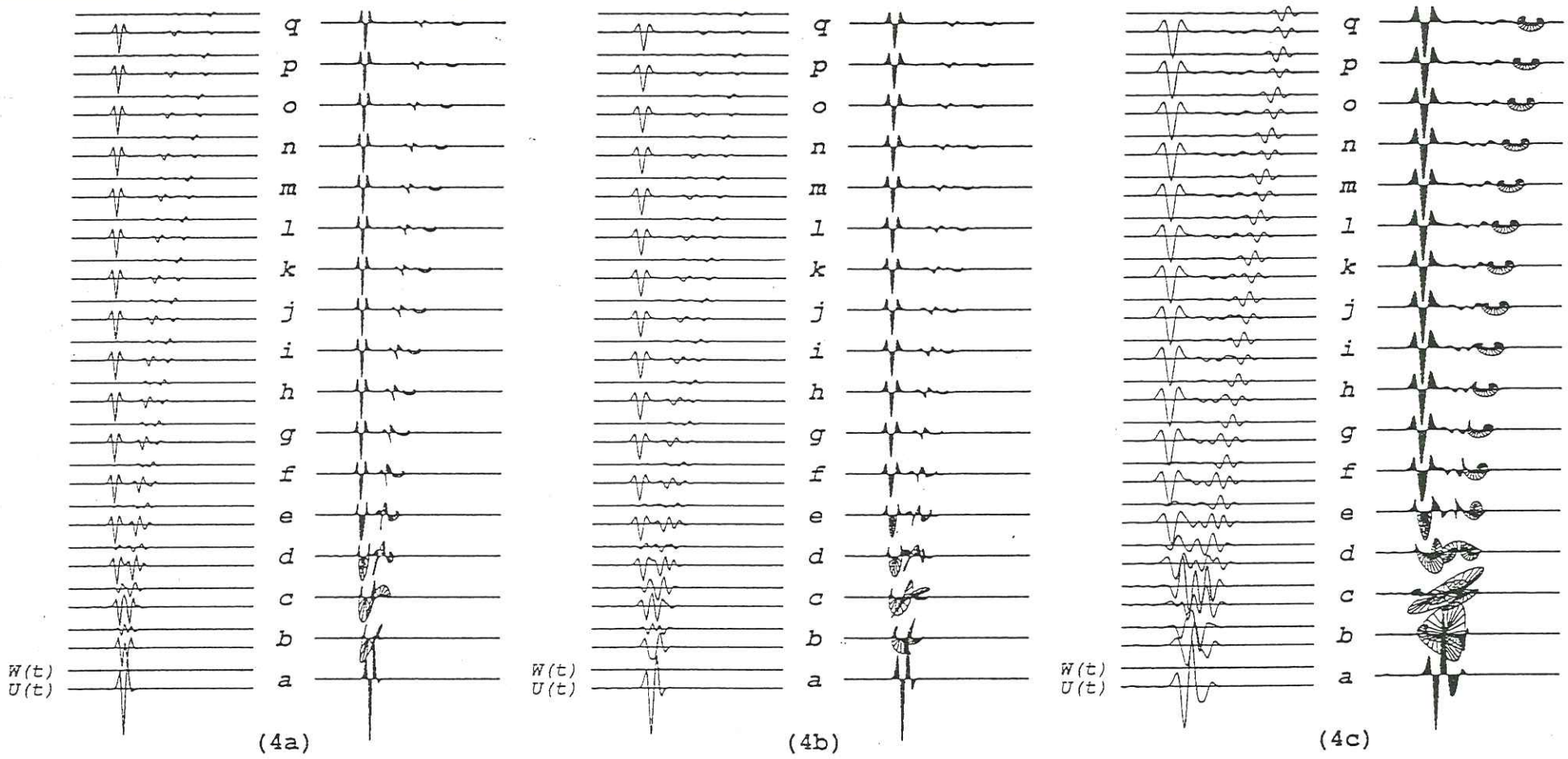

Fig. II.4 - Same as figures II.3a, II.3b, and II.3c for a vertically incident plane *SV*-wave with a wavelength of λ=h (Explanations in text).

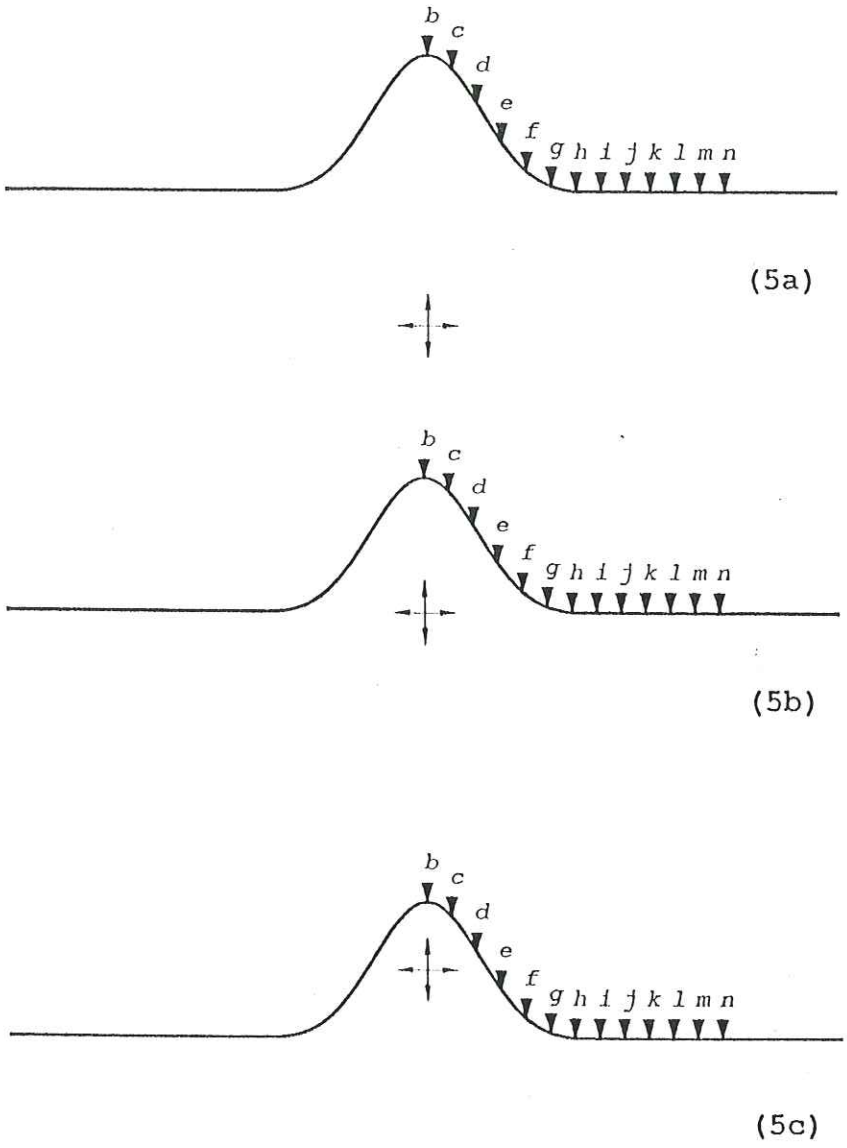

Fig. II.5 - Geometry of the topography profile and location of the receivers. The shape ratio is h/l=*0.375*. The three positions of the explosions studied are indicated by the crossed arrows: below (a), at the base (b), and inside (c) the ridge.

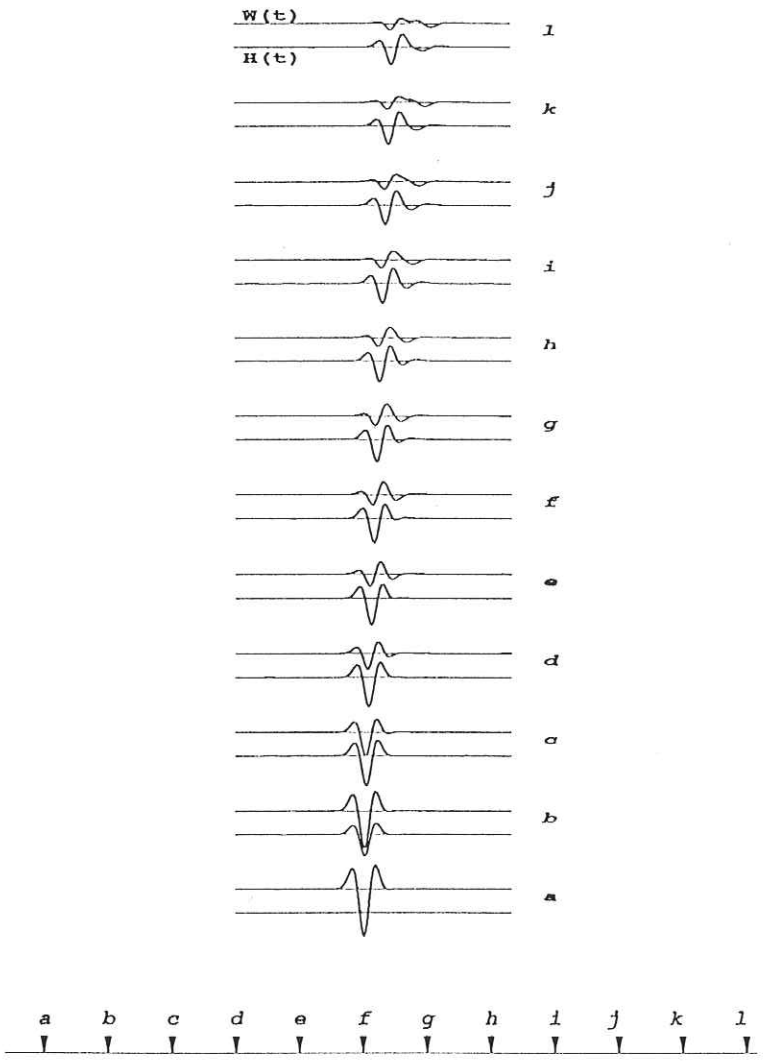

Fig. II.6 - Surface displacement produced by an explosion located under a flat surface. The geometry of the problem is displayed in the lower part of the figure.

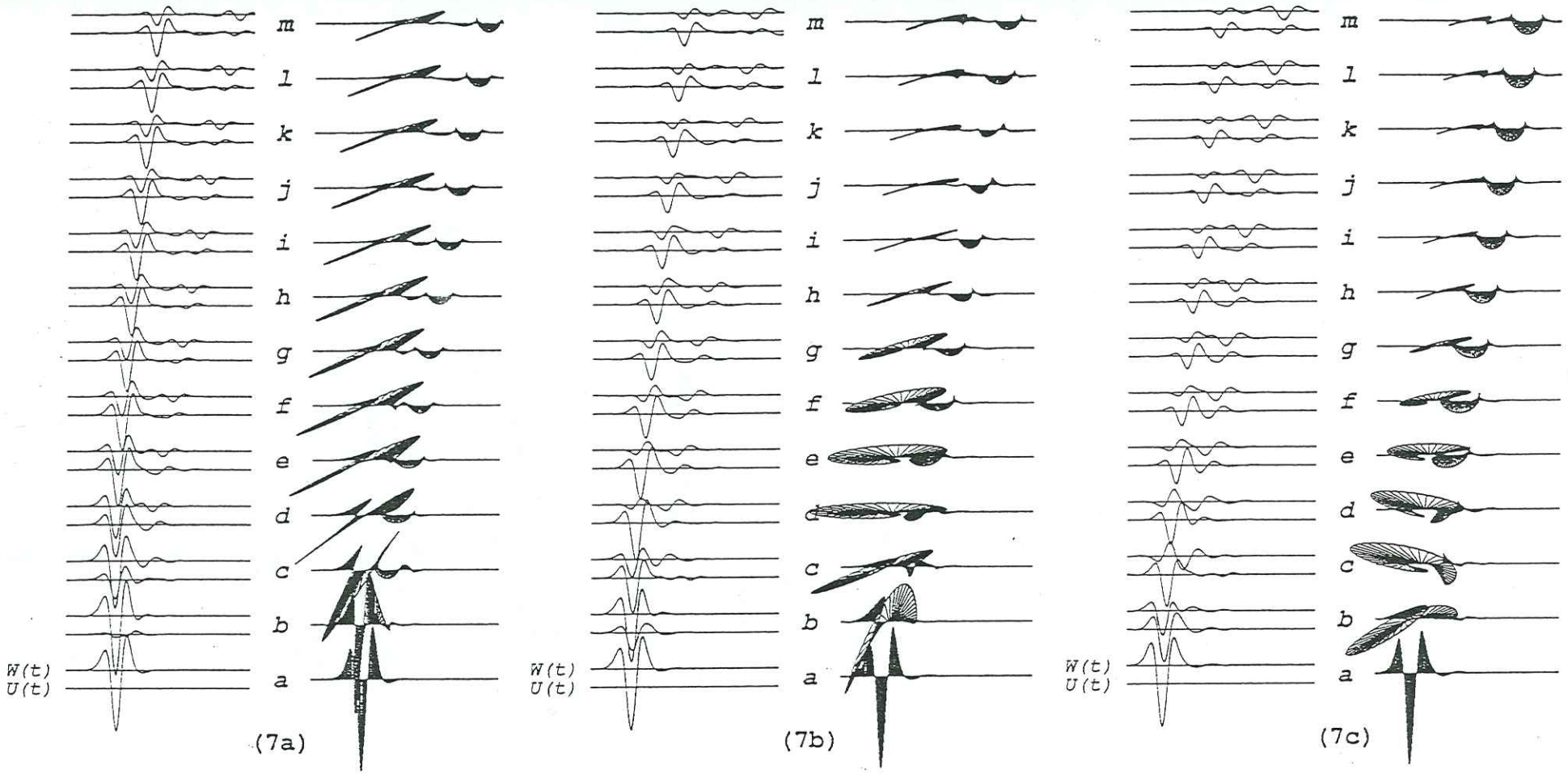

Fig. II.7 - Display of the surface displacement produced for the three configurations of figure II.5. The time window is 2 s. The source time function is a Ricker wavelet. Its central frequency corresponds to a compressional wavelength $\lambda_\alpha = 2.5h$.

- III -

A boundary integral equation-discrete wavenumber representation method to study wave propagation in multilayered media having irregular interfaces

Michel Bouchon, Michel Campillo, and Stéphane Gaffet

Geophysics **54**, 1134-1140

A boundary integral equation-discrete wavenumber representation method to study wave propagation in multilayered media having irregular interfaces

Michel Bouchon*, Michel Campillo*, and Stephane Gaffet‡

ABSTRACT

We present a method which combines boundary-integral equation techniques with the discrete wavenumber Green's function representation to study wave propagation in multilayered media having irregular interfaces. The approach is based on the representation of the interfaces by distributions of body forces, the radiation from which is equivalent to the scattered wave field produced by the diffracting boundaries. The Green's functions are evaluated by the discrete wavenumber method. Propagator matrices are introduced to relate force distributions on neighboring interfaces. The solution then requires the inversion of a matrix at each interface. The dimensions of the linear system are independent of the number of layers considered, and the computation time varies linearly with the number of interfaces. We apply the method to calculate surface and vertical seismic profiles in the presence of synclinal or anticlinal structures.

INTRODUCTION

Many problems of wave propagation involving inhomogeneous media can be formulated in terms of boundary-integral equations. The use of this approach, however, lags far behind the use of finite-difference or finite-element techniques. Indeed, the finite-difference and finite-element schemes are often thought of as exclusive tools for calculating the complete solution to problems of wave propagation in laterally varying media. The aim of this paper is to show that the boundary-integral equation formulation may provide an alternate method of calculation.

In the present work, we extend the boundary-integral equation-discrete wavenumber method (Bouchon, 1985; Campillo and Bouchon, 1985; Campillo, 1987) to multiple irregular interfaces and apply the method to seismic exploration problems. The presentation is restricted to antiplane motion (*SH* waves), which is similar to the acoustic case. The generalization of the scheme to the elastic case, however, is straightforward.

Although the boundary-integral equation formulation for acoustic waves was introduced more than a century ago by Helmholtz and Kirchhoff, use of the method to solve problems of wave propagation in multilayered media has been limited. Previous examples include the works of Larner (1970), Jiracek (1972), and Bard and Tucker (1985), who use the Aki-Larner method, and Dravinski (1983).

DESCRIPTION OF THE METHOD

The problem configuration is depicted in Figure 1. The medium consists of a series of homogeneous layers separated by irregular interfaces. x and z denote the horizontal and vertical directions, respectively. The medium is assumed to be invariant in the direction normal to the (x, z) plane; the free surface is flat; and the seismic source is located at the surface.

The displacement field radiated by a surface force Q_0 with time dependence $e^{i\omega t}$ may be written (Lamb, 1904)

$$u_0(x, z) = \frac{Q_0 e^{i\omega t}}{2\pi i \rho_1 \alpha_1^2} \int_{-\infty}^{\infty} \frac{e^{-i\nu z}}{\nu} e^{-ik(x - x_0)}\, dk, \qquad (1)$$

with

$$\nu = [(\omega/\alpha_1)^2 - k^2]^{1/2},$$

where k and ν denote the horizontal and vertical wavenumbers, x_0 is the point of application of the force, and ρ_1 and α_1 are the density and wave velocity in the surface layer.

In order to evaluate the radiated wave field, we introduce a periodicity L in the source-medium configuration. Equation (1) is then replaced by (Bouchon and Aki, 1977)

Manuscript received by the Editor November 2, 1987; revised manuscript received March 10, 1989.
*IRIGM, Universite Joseph Fourier, BP 53X, 38041 Grenoble Cedex, France.
‡LDG/CEA, Centre et Etudes de Bruyeres le Chatel, BP 12, 91680 Bruyeres le Chatel, France.

$$u_0(x, z) = \frac{Q_0 e^{i\omega t}}{iL\rho_1\alpha_1^2} \sum_{n=-M}^{M} \frac{e^{-i\nu_{1,n}z}}{\nu_{1,n}} e^{-ik_n(x-x_0)}, \qquad (2)$$

with

$$k_n = \frac{2\pi}{L} n \quad \text{and} \quad \nu_{1,n} = \left(\frac{\omega^2}{\alpha_1^2} - k_n^2\right)^{1/2}, \qquad \text{Im}\,(\nu_{1,n}) < 0,$$

and M is an integer large enough to ensure the convergence of the series. The substitution of equation (2) for equation (1) replaces the single-source radiation problem, which is difficult to solve, by the numerically simpler problem of evaluating the radiation of a periodic array of sources. As shown by Bouchon and Aki (1977), the single-source, time-domain solution may be later retrieved from the multiple-source result provided that the frequency is chosen to be complex. This choice also removes numerical singularities from equation (2).

We next discretize each interface ℓ into an odd number of points N_ℓ equally spaced along the x direction. At each point i of the interface ℓ, we apply two body forces: $Q_{i\ell 1}e^{i\omega t}$ located on the upper side of the interface radiating into the upper layer and $Q_{i\ell 2}e^{i\omega t}$ situated on the lower side of the interface and radiating into the lower layer. The displacement fields associated with these forces, because of the periodicity introduced, are

$$u_{i,\ell}(x, z) = \frac{Q_{i\ell 1}e^{i\omega t}}{2iL\rho_\ell\alpha_\ell^2} \sum_{n=-\infty}^{\infty} \frac{e^{-i\nu_{\ell,n}|z-z_{i,\ell}|}}{\nu_{\ell,n}} e^{-ik_n(x-x_{i,\ell})} \qquad (3)$$

in the upper layer and in the lower layer

$$u_{i,\ell+1}(x, z) = \frac{Q_{i\ell 2}e^{i\omega t}}{2iL\rho_{\ell+1}\alpha_{\ell+1}^2} \times \sum_{n=-\infty}^{\infty} \frac{e^{-i\nu_{\ell+1,n}|z-z_{i,\ell}|}}{\nu_{\ell+1,n}} e^{-ik_n(x-x_{i,\ell})} \qquad (4)$$

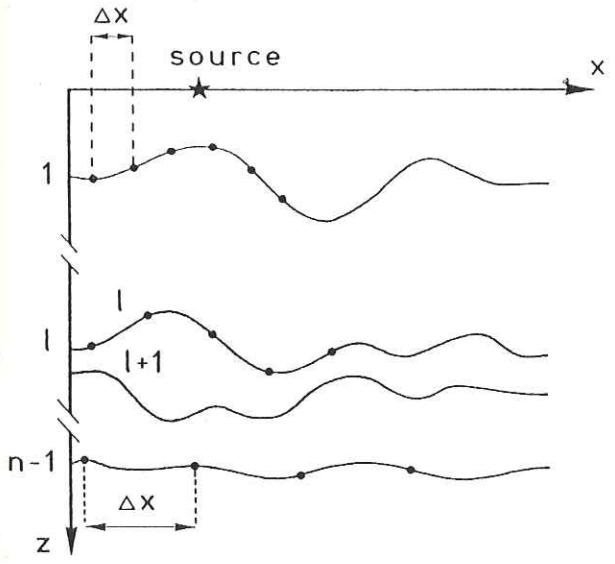

FIG. 1. Problem configuration.

with

$$\nu_{\ell,n} = \left(\frac{\omega^2}{\alpha_\ell^2} - k_n^2\right)^{1/2}, \qquad \text{Im}\,(\nu_{\ell,n}) < 0,$$

and where $(x_{i,\ell}, z_{i,\ell})$ denotes the x and z coordinates of the discretized interface.

Thus, the total displacement field associated with the force distribution along the interface ℓ in the upper layer is

$$u_\ell(x, z) = \frac{e^{i\omega t}}{2iL\rho_\ell\alpha_\ell^2} \sum_{i=1}^{N_\ell} Q_{i\ell 1} \times \sum_{n=-\infty}^{\infty} \frac{e^{-i\nu_{\ell,n}|z-z_{i,\ell}|}}{\nu_{\ell,n}} e^{-ik_n(x-x_{i,\ell})} \qquad (5)$$

and has a similar form in the lower layer. However, because of the existence of both periodicity and discretization in x, equation (5) reduces to (Bouchon, 1985)

$$u_\ell(x, z) = \frac{e^{i\omega t}}{2iL\rho_\ell\alpha_\ell^2} \times \sum_{i=1}^{N_\ell} Q_{i\ell 1} \sum_{n=-M_\ell}^{M_\ell} \frac{e^{-i\nu_{\ell,n}|z-z_{i,\ell}|}}{\nu_{\ell,n}} e^{-ik_n(x-x_{i,\ell})}, \qquad (6)$$

with M_ℓ such that $N_\ell = 2M_\ell + 1$.

The discretization in x at equal Δx intervals implies a periodicity in the horizontal wavenumber space, so that the wavenumber summation in equation (6) is restricted to the interval

$$\left[-\frac{\pi}{\Delta x}, \frac{\pi}{\Delta x}\right] \quad \text{or} \quad \left[-\frac{\pi}{L} N_\ell, \frac{\pi}{L} N_\ell\right].$$

The choices of both the periodicity length L and the discretization interval Δx thus uniquely define the sampling of the wavenumber space. The number of terms of the two series in equation (6) is simply $L/\Delta x$. Similarly, in the $\ell + 1$th layer

$$u_{\ell+1}(x, z) = \frac{e^{i\omega t}}{2iL\rho_{\ell+1}\alpha_{\ell+1}^2} \times \sum_{i=1}^{N_\ell} Q_{i\ell 2} \sum_{n=-M_\ell}^{M_\ell} \frac{e^{-i\nu_{\ell+1,n}|z-z_{i,\ell}|}}{\nu_{\ell+1,n}} e^{-ik_n(x-x_{i,\ell})}. \qquad (7)$$

We now define the displacement-stress vector at interface ℓ as

$$\mathbf{S}_\ell = [u_\ell(x_{j,\ell}, z_{j,\ell}), j = 1, \ldots N_\ell; \sigma_\ell(x_{j,\ell}, z_{j,\ell}), j = 1, \ldots N_\ell]^T, \qquad (8)$$

with

$$\sigma_\ell = \rho_\ell\alpha_\ell^2\left(n_x \frac{\partial u_\ell}{\partial x} + n_z \frac{\partial u_\ell}{\partial z}\right), \qquad (9)$$

where n_x and n_z denote the x and z components of the normal to the interface.

Using equations (6) and (7), we express the displacement-stress field at the ℓth interface as the sum of the contributions from the top side of the ℓth interface (self-interaction

term) and from the underside of the ℓ-1th interface (extrapolated term) in the form (for $\ell \neq 1$)

$$S_\ell = \underline{A}_{\ell,1}\mathbf{Q}_{\ell-1,2} + \underline{A}_{\ell,2}Q_{\ell,1}, \tag{10}$$

where the elements of $\underline{A}_{\ell,1}$ are

$$a_{j,i}^{\ell,1} = \frac{1}{2iL\rho_\ell\alpha_\ell^2} \sum_{n=-M_{\ell-1}}^{M_{\ell-1}} \frac{e^{-i\nu_{\ell,n}|z_{j,\ell}-z_{i,\ell-1}|}}{\nu_{\ell,n}} e^{-ik_n(x_{j,\ell}-x_{i,\ell-1})}$$

and

$$a_{j+N_\ell,i}^{\ell,1} = \frac{-1}{2L} \times \sum_{n=-M_{\ell-1}}^{M_{\ell-1}} \left(n_{z_{j,\ell}} \operatorname{sgn}(z_{j,\ell}-z_{i,\ell-1}) + n_{x_{j,\ell}} \frac{k_n}{\nu_{\ell,n}} \right) \times e^{-i\nu_{\ell,n}|z_{j,\ell}-z_{i,\ell-1}|} e^{-ik_n(x_{j,\ell}-x_{i,\ell-1})},$$

with $\operatorname{sgn}(z_{j,\ell}-z_{i,\ell-1}) = 1$ if $z_{j,\ell} \geq z_{i,\ell-1}$, and $= -1$ otherwise for $j = 1, \ldots N_\ell$ and $i = 1, \ldots N_{\ell-1}$; and the elements of $\underline{A}_{\ell,2}$ are

$$a_{j,i}^{\ell,2} = \frac{1}{2iL\rho_\ell\alpha_\ell^2} \sum_{n=-M_\ell}^{M_\ell} \frac{e^{-i\nu_{\ell,n}|z_{j,\ell}-z_{i,\ell}|}}{\nu_{\ell,n}} e^{-ik_n(x_{j,\ell}-x_{i,\ell})}$$

and

$$a_{j+N_\ell,i}^{\ell,2} = \frac{-1}{2L} \sum_{n=-M_\ell}^{M_\ell} \left(n_{z_{j,\ell}} \operatorname{sgn}(z_{j,\ell}-z_{i,\ell}) + n_{x_{j,\ell}} \frac{k_n}{\nu_{\ell,n}} \right) \times e^{-i\nu_{\ell,n}|z_{j,\ell}-z_{i,\ell}|} e^{-ik_n(x_{j,\ell}-x_{i,\ell})},$$

with $\operatorname{sgn}(z_{j,\ell}-z_{i,\ell}) = 1$ if $z_{j,\ell} > z_{i,\ell}$, and $= -1$ otherwise, for $j = 1, \ldots, N_\ell$ and $i = 1, \ldots, N_\ell$.

Because of the continuity of displacement and stress across the interface, we also have

$$\mathbf{S}_\ell = \underline{B}_{\ell+1,1}\mathbf{Q}_{\ell,2} + \underline{B}_{\ell+1,2}\mathbf{Q}_{\ell+1,1}, \tag{11}$$

where the elements of $\underline{B}_{\ell+1,1}$ are

$$b_{j,i}^{\ell+1,1} = \frac{1}{2iL\rho_{\ell+1}\alpha_{\ell+1}^2} \times \sum_{n=-M_\ell}^{M_\ell} \frac{e^{-i\nu_{\ell+1,n}|z_{j,\ell}-z_{i,\ell}|}}{\nu_{\ell+1,n}} e^{-ik_n(x_{j,\ell}-x_{i,\ell})} \quad \text{and}$$

$$b_{j+N_\ell,i}^{\ell+1,1} = \frac{-1}{2L} \times \sum_{n=-M_\ell}^{M_\ell} \left[n_{z_{j,\ell}} \operatorname{sgn}(z_{j,\ell}-z_{i,\ell}) + n_{x_{j,\ell}} \frac{k_n}{\nu_{\ell+1,n}} \right] \times e^{-i\nu_{\ell+1,n}|z_{j,\ell}-z_{i,\ell}|} e^{-ik_n(x_{j,\ell}-x_{i,\ell})},$$

with $\operatorname{sgn}(z_{j,\ell}-z_{i,\ell}) = 1$ if $z_{j,\ell} \geq z_{i,\ell}$, and $= -1$ otherwise, for $j = 1, \ldots N_\ell$ and $i = 1, \ldots N_\ell$ and where the elements of $\underline{B}_{\ell+1,2}$ are

$$b_{j,i}^{\ell+1,2} = \frac{1}{2iL\rho_{\ell+1}\alpha_{\ell+1}^2} \times \sum_{n=-M_{\ell+1}}^{M_{\ell+1}} \frac{e^{-i\nu_{\ell+1,n}|z_{j,\ell}-z_{i,\ell+1}|}}{\nu_{\ell+1,n}} e^{-ik_n(x_{j,\ell}-x_{i,\ell+1})} \quad \text{and}$$

$$b_{j+N_\ell,i}^{\ell+1,2} = \frac{-1}{2L} \times \sum_{n=-M_{\ell+1}}^{M_{\ell+1}} \left[n_{z_{j,\ell}} \operatorname{sgn}(z_{j,\ell}-z_{i,\ell+1}) + n_{x_{j,\ell}} \frac{k_n}{\nu_{\ell+1,n}} \right] \times e^{-i\nu_{\ell+1,n}|z_{j,\ell}-z_{i,\ell+1}|} e^{-ik_n(x_{j,\ell}-x_{i,\ell+1})},$$

with $\operatorname{sgn}(z_{j,\ell}-z_{i,\ell+1}) = 1$ if $z_{j,\ell} > z_{i,\ell+1}$, and $= -1$ otherwise for $j = 1, \ldots, N_\ell$ and $i = 1, \ldots, N_{\ell+1}$.

The continuity of the displacement-stress vector at the deepest interface may be written as

$$\mathbf{S}_{n-1} = \underline{A}_{n-1,1}\mathbf{Q}_{n-2,2} + \underline{A}_{n-1,2}\mathbf{Q}_{n-1,1} = \underline{B}_{n,1}\mathbf{Q}_{n-1,2}, \tag{12}$$

which implies

$$\mathbf{Q}_{n-1} = \underline{D}_{n-1}^{-1}\underline{A}_{n-1,1}\mathbf{Q}_{n-2,2}, \tag{13}$$

where we have defined

$$\underline{D}_{n-1} = [-\underline{A}_{n-1,2}; \underline{B}_{n,1}] \tag{14}$$

and

$$\mathbf{Q}_{n-1} = [\mathbf{Q}_{n-1,1}; \mathbf{Q}_{n-1,2}].$$

Similarly, the force distribution at interface ℓ, $2 \leq \ell \leq n-2$, may be written in the form

$$\mathbf{Q}_\ell = \underline{D}_\ell^{-1}\underline{A}_{\ell,1}\mathbf{Q}_{\ell-1,2} \tag{15}$$

with

$$\underline{D}_\ell = [-\underline{A}_{\ell,2}; \underline{B}_{\ell+1,1} + \underline{B}_{\ell+1,2}(\underline{D}_{\ell+1}^{-1})_1\underline{A}_{\ell+1,1}] \tag{16}$$

and where $(\underline{D}_{\ell+1}^{-1})_1$ denotes the upper half of the inverse matrix. Equation (15) propagates the force distribution from one interface to the next one.

At the shallowest interface, we have

$$\mathbf{S}_1 = \underline{A}_{1,2}\mathbf{Q}_{1,1} + \mathbf{S}_{s0} = \underline{B}_{2,1}\mathbf{Q}_{1,2} + \underline{B}_{2,2}\mathbf{Q}_{2,1}, \tag{17}$$

where $\mathbf{S}_{s0}$ is the incident displacement-stress vector produced by the source and the elements of $\underline{A}_{1,2}$ are

$$a_{j,i}^{1,2} = \frac{1}{2iL\rho_1\alpha_1^2} \sum_{n=-M_1}^{M_1} \frac{1}{\nu_{1,n}} \times \left[e^{-i\nu_{1,n}|z_{j,1}-z_{i,1}|} + e^{i\nu_{1,n}(z_{j,1}+z_{i,1})} \right] e^{-ik_n(x_{j,1}-x_{i,1})} \quad \text{and}$$

$$a_{j+N_1,i}^{1,2} = \frac{-1}{2L} \sum_{n=-M_1}^{M_1} \left\{ n_{z_{j,1}} \left[\operatorname{sgn}(z_{j,1}-z_{i,1}) e^{-i\nu_{1,n}|z_{j,1}-z_{i,1}|} + e^{-i\nu_{1,n}(z_{j,1}+z_{i,1})} \right] + n_{x_{j,1}} \frac{k_n}{\nu_{1,n}} \times \left[e^{-i\nu_{1,n}|z_{j,1}-z_{i,1}|} + e^{-i\nu_{1,n}(z_{j,1}+z_{i,1})} \right] \right\} e^{-ik_n(x_{j,1}-x_{i,1})},$$

with sgn $(z_{j,1} - z_{i,1}) = 1$ if $z_{j,1} > z_{i,1}$, and $= -1$ otherwise. From equation (17) we finally get the solution

$$\mathbf{Q}_1 = \underline{\mathbf{D}}_1^{-1}\mathbf{S}_{s0}, \tag{18}$$

where $\underline{\mathbf{D}}_1$ is given by equation (16).

CHOICE OF THE INTERFACE PERIODICITY AND SAMPLING

The interface sampling is mostly a function of the wavelengths present. The shorter the wavelengths, the smaller the required sampling interval. Campillo (1987) found that a discretization rate of three points per wavelength is sufficient to make the numerical noise level negligible. In Figure 2, we present a comparison between the surface displacement profile obtained by the present method for a flat-layered medium and the one calculated by using plane-wave reflection and transmission coefficients. In both cases, a line force is applied at the surface, oriented perpendicular to the line of receivers. The source wave field is expressed by equation (2). The diffracted wave field is calculated by the present method, i.e., by representing each interface by a double distribution of sources. This result is compared to the displacement field obtained by evaluating each plane-wave component of the source radiation [equation (2)] using the reflection and transmission matrices for the different layers. The model consists of four layers overlying a half-space. The frequency of the source is 20 Hz, and the comparison is made over one period of the source-medium configuration.

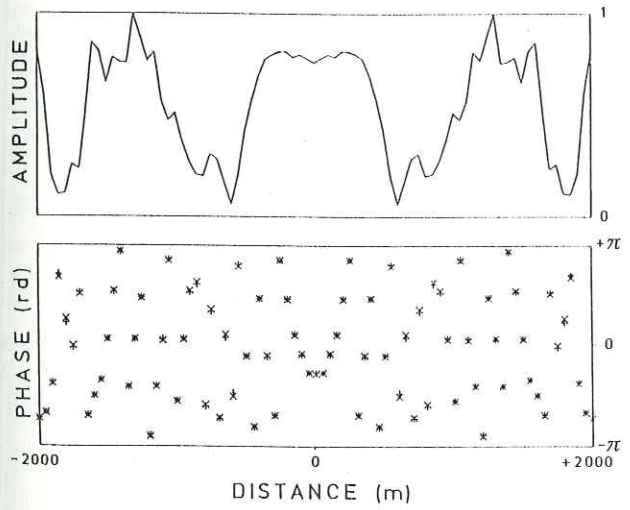

FIG. 2. Comparison of the surface displacement calculated by the boundary-integral equation-discrete wavenumber formulation (x) with the solution obtained by using the flat-layer reflection and transmission coefficients (+). The interfaces are discretized at a rate of two points per shortest wavelength. The model consists of four horizontal layers overlying a half-space. The layer thicknesses are 500, 200, 100, and 200 m. The corresponding wave velocities are 2000, 3000, 2600, 3500 and 4000 m/s with associated densities of 2.0, 2.3, 2.2, 2.4, and 2.5 g/cm^3. The source is located at the middle of the distance range considered which is equal to the periodicity interval (4000 m). The frequency considered is 20 Hz plus a small imaginary part equal to one-tenth of the real part.

The discretization interval is different for each interface and is half of the smallest wavelength present on either side of the boundary.

A similar comparison is made in Figure 3 for a sampling rate of three points per wavelength. The remarkable agreement between the two solutions shows the numerical validity of the interface representation and of the propagator matrix scheme. It also confirms that sampling at three points per wavelength is sufficient to ensure the accuracy of the results. At low frequencies (including the static case which is present in the solution before the convolution with the source is performed), we impose, however, a minimum number of points to represent the shape of the interface. In all the applications presented, this minimum value of N_c was arbitrarily choosen to be 41.

The periodicity length L of the source-medium configuration must be chosen according to the simple criterion that no disturbance from a neighboring source or diffracting boundary arrives at the receivers within the time window T considered. The choice of the imaginary part of the frequency has been discussed in previous papers (e.g., Bouchon and Aki, 1977). In all of the applications presented here, the imaginary angular frequency is $-2\pi/T$.

The use of a different sample rate at each interface minimizes computation time by preventing unnecessary sampling of interfaces separating high-velocity formations.

APPLICATIONS

To illustrate the usefulness of our method, we apply it to several exploration configurations. The first application is illustrated in Figure 4. The model is a sine-shaped anticline. The layer and lower half-space velocities are 2500 m/s and 4000 m/s, with corresponding densities of 2.2 g/cm^3 and 2.6 g/cm^3. The anelastic attenuation of the rocks is introduced in the calculation through the use of slightly dispersive complex wave velocities (e.g., Aki and Richards, 1980). The quality factors used are $Q = 40$ in the surface layer and $Q = 400$ in the half-space. The source is a Ricker wavelet with

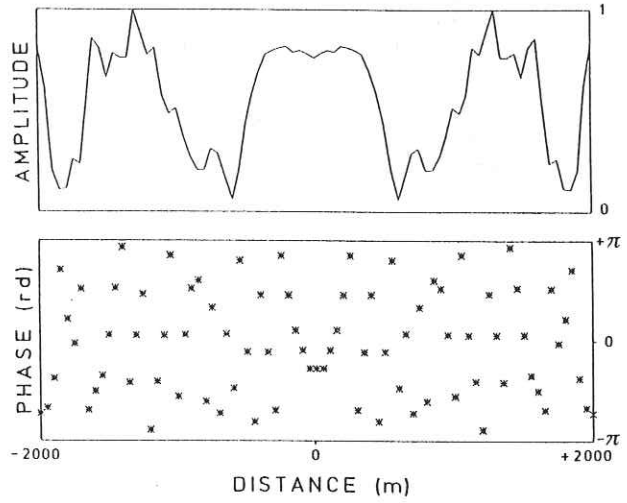

FIG. 3. Same as Figure 2 for an interface sampling rate equal to one-third of the smallest wavelength.

center frequency equal to 25 Hz. The seismograms show the diffracted surface displacement. They display two major arrivals: the first reflection and the first multiple reflection from the top of the anticline.

The second model is a sine-shaped syncline (Figure 5). The surface and half-space velocities are now 2500 m/s and 3000 m/s with corresponding densities of 2.2 g/cm^3 and 2.4 g/cm^3 and quality factors of 40 and 100. The seismograms illustrate the diffracted surface displacement and are characterized by a caustic.

The next example considered (Figure 6) involves a folded anticline. The layer wave velocities are 2500, 3000, 4000, and 5000 m/s with corresponding densities of 2.2, 2.4, 2.6, and 2.7 g/cm^3 and quality factors of 40, 100, 400, and 600. As above, the source emits a Ricker pulse with a 25 Hz center frequency. The diffracted surface displacement seismograms display the primary reflection pulses from the three interfaces. The amplitude of the multiples is very small for this configuration.

The fourth application, displayed in Figure 7, corresponds to a filled sedimentary basin overlying a folded syncline. The layer wave velocities are 2500, 2800, 3000, and 3500 m/s with associated densities of 2.2, 2.3, 2.4, and 2.5 g/cm^3 and quality factors of 40, 80, 100, and 250. The source is the same as the one previously described. The reflections from the folded layer display the characteristic caustics previously seen in Figure 5.

The final application is the calculation of a vertical seismic profile (VSP) in the model displayed in Figure 7. The recording well is located along the axis of the syncline. The source location is the one indicated in Figure 7. The resulting profile is shown in full scale in Figure 8 and with an amplitude cutoff and independent trace normalization in Figure 9. One interesting feature of the VSP is the apparent splitting of the upgoing and downgoing branches due to the multiplicity of paths for waves reflected by the syncline structure.

CONCLUSION

We have presented a formulation which combines boundary-integral equation techniques with the discrete-wavenumber Green's function representation to calculate the propagation of seismic waves in multilayered media having irregular interfaces. The method is based on a double discretization—in space and in the wavenumber domain—of the integral equations representing the diffracted wave field. The resulting linear system may be decomposed into a combination of layer matrices. The solution then requires the inversion of a matrix at each interface. The method provides a tool for computing surface reflection or refraction profiles and VSPs.

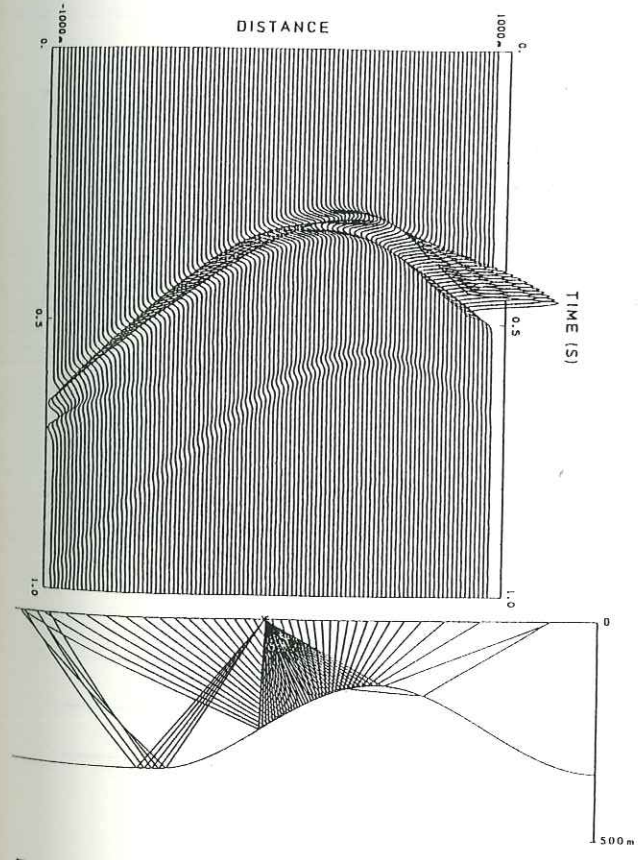

FIG. 4. Diffracted surface displacement and corresponding source-medium configuration. The periodicity length is L = 4000 m.

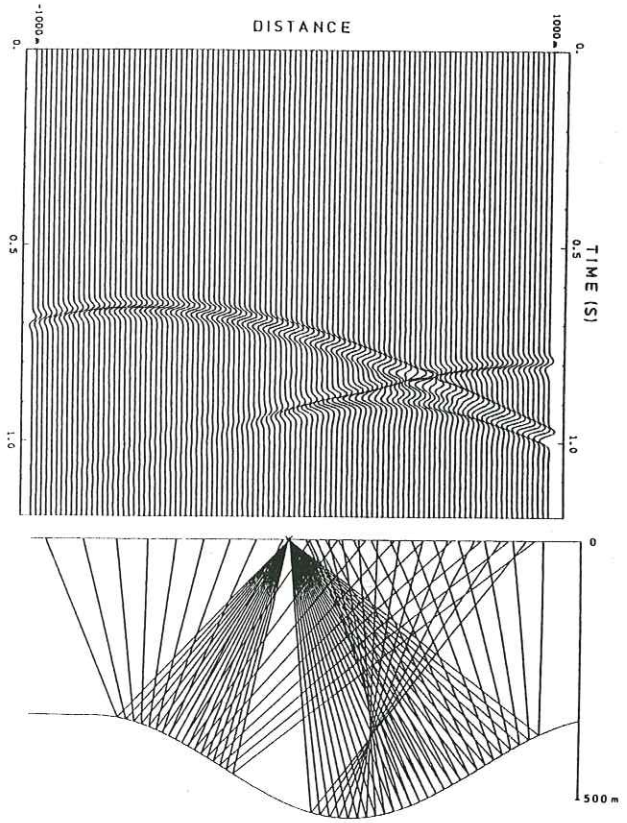

FIG. 5. Diffracted surface displacement and corresponding source-medium configuration.

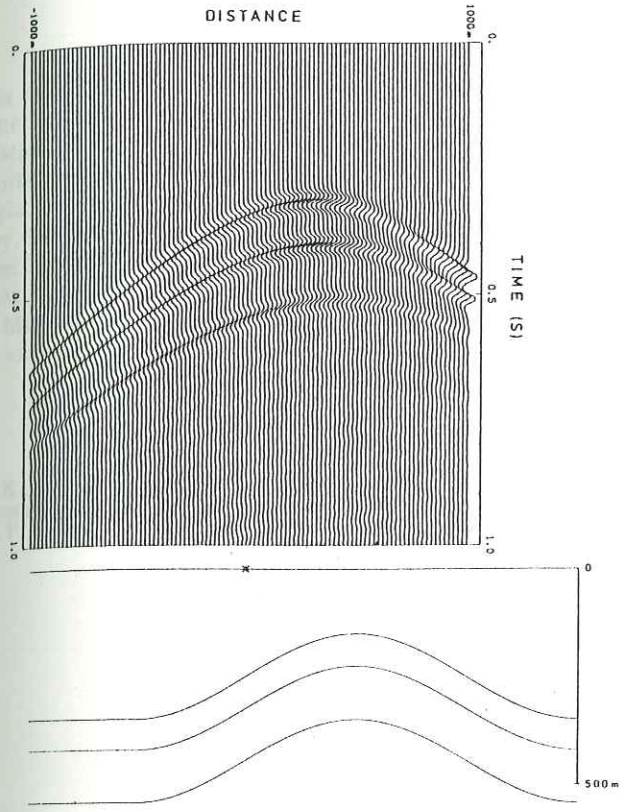

FIG. 6. Diffracted surface displacement and corresponding source-medium configuration.

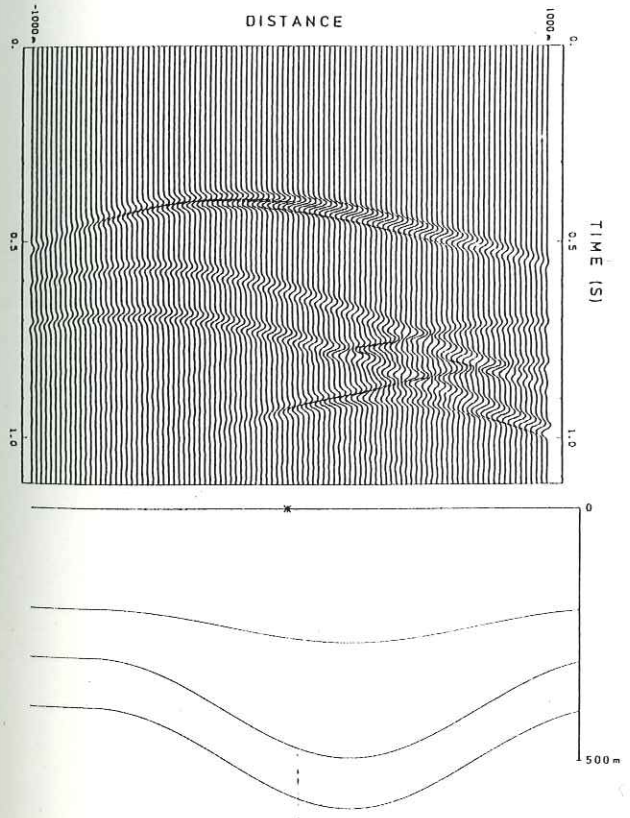

FIG. 7. Diffracted seismogram and corresponding source-medium configuration.

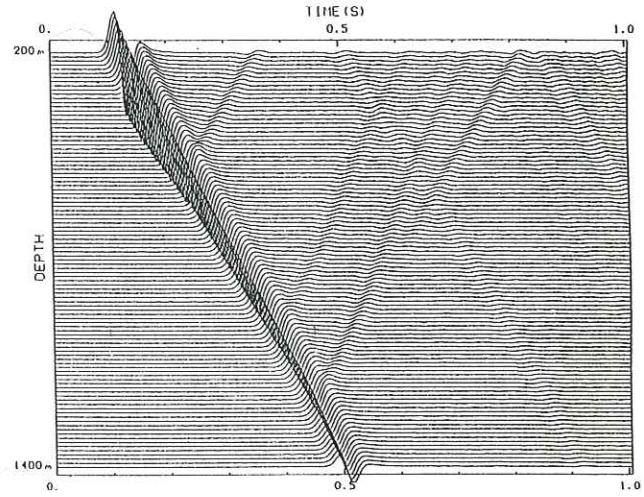

FIG. 8. Vertical seismic profile calculated for the source-medium configuration shown in Figure 7. The recording borehole lies along the axis of the syncline. The source offset is 250 m, and its time dependence is a Ricker pulse of 25 Hz center frequency.

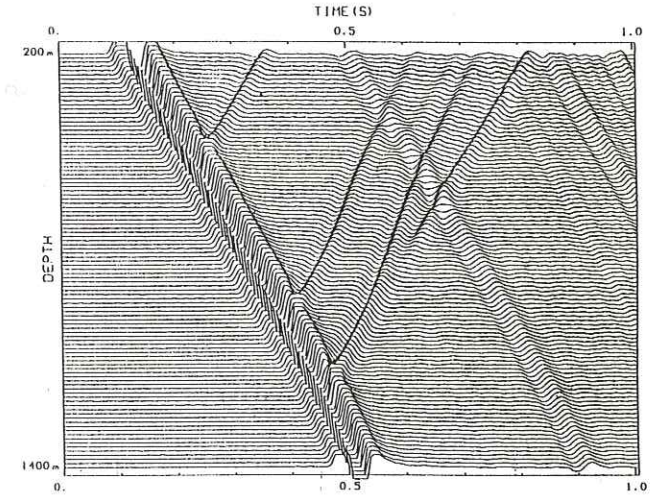

FIG. 9. Same as Figure 8 except for the plotting scale. The traces are normalized independently and an amplitude cutoff equal to one-tenth the maximum amplitude of each signal is applied.

ACKNOWLEDGMENTS

This work was made possible through the support of the Société Nationale Elf Aquitaine (Production), the Compagnie Générale de Géophysique, and the Centre de Calcul Vectoriel pour la Recherche. We thank Philippe Staron, Patricia Arditty, Georges Arens, Benoit Paternoster, Michel Revoy, Wafik Beydoun, Michel Waeselynck, and Francois Chapel from SNEA(P), Fernand Baixas from CGG, and Nafi Toksöz, Denis Schmitt, Ted Madden, and Roger Turpening from MIT for stimulating discussions and encouragement in the course of this work.

REFERENCES

Aki, K., and Richards, P. G., 1980, Quantitative seismology: Theory and methods: W. H. Freeman and Co.

Bard, P. Y., and Tucker, B. E., 1985, Underground and ridge site effects: a comparison of observation and theory: Bull. Seis. Soc. Am., **75**, 905–922.

Bouchon, M., 1985, A simple, complete numerical solution to the problem of diffraction of *SH* waves by an irregular interface: J. Acoust. Soc. Am., **77**, 1–5.

Bouchon, M., and Aki, K., 1977, Discrete wavenumber representation of seismic source wave fields: Bull. Seis. Soc. Am., **67**, 259–277.

Campillo, M., 1987, Modeling of *SH*-wave propagation in an irregularly layered medium—Application to seismic profiles near a dome: Geophys. Prosp., **35**, 236–249.

Campillo, M., and Bouchon, M., 1985, Synthetic *SH*-seismograms in a laterally varying medium by the discrete wavenumber method: Geophys. J. Roy. Astr. Soc., **83**, 307–317.

Dravinksi, M., 1983, Scattering of plane harmonic *SH* waves by dipping layers of arbitrary shape: Bull. Seis. Soc. Am., **73**, 1309–1319.

Jiracek, G. R., 1972, Geophysical studies of electromagnetic scattering from rough surfaces and from irregularly layered structures: Ph.D. thesis, Univ. of Cal., Berkeley.

Lamb, H., 1904, On the propagation of tremors at the surface of an elastic solid: Phil. Trans. Roy. Soc. London, **A203**, 1–42.

Larner, K. L., 1970, Near-receiver scattering of teleseismic body waves in layered crust-mantle models having irregular interfaces: Ph.D. thesis, Mass. Inst. of Tech.

- IV -

Source location and valley shape effects on the P-SV near displacement field using a boundary integral equation-discrete wavenumber representation method.

Stéphane Gaffet and Michel Bouchon

Prepared to be submitted to the *Geophys. J. Int.*

Résumé

Les effets induits sur les champs de déplacements par la présence de vallées sédimentaires de formes irrégulières sont analysés pour des capteurs placés en surface à des distances inférieures à *20* km de la source. Nous montrons l'importance des amplifications et de la défocalisation du champ d'ondes suivant la position de la source dans de tels bassins. La position de la source mais également le milieu dans lequel elle se trouve interviennent sur le contenu de la coda comme nous le montrons dans le cas de vallées sédimentaires bi-couches. La méthode de discrétisation des nombres d'onde est détaillée dans le cas *P-SV* pour la configuration de vallées alluviales à stratifications multiples et irrégulières faisant intervenir le problème des équations intégrales aux frontières.

IV.1 - Introduction

The underground geological structure has a great influence on the observed seismic waveforms and can greatly affect the displacement amplitude as illustrated for instance by the work of Tucker and King (1984), or by the ground motion observed around Mexico City during the great 1985 Michoacan earthquake. In parallel with these observations, theoretical investigations have shown the importance of the geometry of sedimentary basins and valleys on seismic motion (Aki and Larner, 1970; Sánchez-Sesma and Esquivel, 1979; Bard and Bouchon, 1980a, 1980b, 1985; Bard and Gariel, 1986; Campillo, 1987; Sánchez-Sesma *et al.*, 1988; Kawase and Aki, 1989). The aim of the present study is to extend these theoretical investigations to the case where the seismic excitation is a *P-SV* source, such as an explosion, and where the geological structure includes several irregular layers. We use the discrete wavenumber - boundary integral equation method previously described in a *SH* formulation (Bouchon *et al.* 1989). Following the study made on the topographic effects at short distances (Gaffet and Bouchon, 1989) we investigate the effects of the source location and of the basin interface shape on the displacement field recorded by surface receivers at short distance from the source.

IV.2 - Description of the method

The method is described in the case of a semi-infinite space underlying a valley made up of a stack of laterally varying layers and bounded by a flat free surface (figure IV.1). The displacement field is computed frequency by frequency from the displacement potentials given by Lamb (1904) for horizontal and vertical forces acting at a point (x_p , z_p) of an infinite homogeneous elastic space. These compressional and shear potentials are written in a half space formulation to directly cancel the tractions at the free surface. Following the approach developed by Bouchon and Aki (1977), we introduce a horizontal spatial periodicity X_L of the application point of force. This spatial periodicity induces a wavenumber space sampling with a step $\Delta k = 2\pi / X_L$. Two distributions of couples of horizontal and vertical forces located on the upper (*i.e.* $[Q_{p_l}^{h\,upper} \; exp(i\omega t) \; ; \; Q_{p_l}^{v\,upper} \; exp(i\omega t)]$) and lower (*i.e.* $[Q_{p_l}^{h\,lower} \; exp(i\omega t) \; ; \; Q_{p_l}^{v\,lower} \; exp(i\omega t)]$) sides of each interface l are used to represent the upward and downward elastic diffracted fields. These couples are regularly spaced at Δx sampling interval along the interfaces l (l= *1, ... , L*). This sampling leads to a periodic wavenumber space restricting the wavenumber range to $[\ -\pi/\Delta x \ ; \ +\pi/\Delta x\ ]$. The representation of the diffracted field can be made as precise as desired when reducing Δx. The amplitudes $Q_{p_l}^{h\,upper}$, $Q_{p_l}^{v\,upper}$, $Q_{p_l}^{h\,lower}$, and $Q_{p_l}^{v\,lower}$ are determined to insure the continuity of the displacement-traction field across the interfaces.

The compressional and shear displacement potentials for a distribution of P_l horizontal forces regularly spaced along an interface l in a periodic elastic homogeneous half space are given by:

$$\phi_{h,l}^{½\ space} = F \sum_{p_l=1}^{p_l=P_l} Q_{p_l}^{h} \sum_{n=-M}^{n=+M} \left[\frac{k_n}{\nu_n} E_{np_l} + \frac{k_n}{\nu_n} R_{PP} \; T_{np_l} + R_{SP} \; V_{np_l} \right] H_{np_l} \qquad (1)$$

$$\psi_{h,l}^{½\ space} = F \sum_{p_l=1}^{p_l=P_l} Q_{p_l}^{h} \sum_{n=-M}^{n=+M} \left[-sign(z - z_{p_l}) \, G_{np_l} + R_{SS} \; U_{np_l} + \frac{k_n}{\nu_n} R_{PS} \; W_{np_l} \right] H_{np_l} \qquad (2)$$

Similarly we obtain for a distribution of P_l vertical forces:

$$\phi^{\text{½ space}}_{\nu,l} = F \sum_{p_l=1}^{p_l=P_l} Q^{\nu}_{p_l} \sum_{n=-M}^{n=+M} [\, sign(z - z_{p_l})\, E_{np_l} - R_{PP}\, T_{np_l} + \frac{k_n}{\gamma_n} R_{SP}\, V_{np_l} \,]\, H_{np_l} \qquad (3)$$

$$\psi^{\text{½ space}}_{\nu,l} = F \sum_{p_l=1}^{p_l=P_l} Q^{\nu}_{p_l} \sum_{n=-M}^{n=+M} [\, \frac{k_n}{\gamma_n} G_{np_l} + \frac{k_n}{\gamma_n} R_{SS}\, U_{np_l} - R_{PS}\, W_{np_l} \,]\, H_{np_l} \qquad (4)$$

with,

$$F = 1 / 2X_L \omega^2 \rho \qquad E_{np_l} = \exp[-i\nu_n |z - z_{p_l}|] \quad G_{np_l} = \exp[-i\gamma_n |z - z_{p_l}|] \qquad (5)$$

$$H_{np_l} = \exp[-ik_n(x - x_{p_l})] \quad T_{np_l} = \exp[-i\nu_n(z - z_{p_l})] \quad U_{np_l} = \exp[-i\gamma_n(z - z_{p_l})]$$

$$V_{np_l} = \exp[-i\nu_n z - i\gamma_n z_{p_l}] \quad W_{np_l} = \exp[-i\gamma_n z - \nu_n z_{p_l}]$$

where $M = \pi / (\Delta k \Delta x)$, $k_n = 2\, n\, \pi / X_L$, $\nu_n^2 = \omega^2 / \alpha^2 - k_n^2$, $\gamma_n^2 = \omega^2 / \beta^2 - k_n^2$, $Im(\nu_n) \leq 0$ and $Im(\gamma_n) \leq 0$. ω denotes the angular frequency, α and β are the compressional and the shear wave velocities, and ρ is the density. R_{PP}, R_{PS}, R_{SP}, and R_{SS} are the reflection coefficients of the potentials at the free surface and are dependent upon k_n, ν_n, and γ_n. The horizontal and vertical displacements in a two dimensional Cartesian space are obtained using Helmholtz' formulas.

$$u(x, z) = \frac{\partial(\phi_h + \phi_v)}{\partial x} - \frac{\partial(\psi_h + \psi_v)}{\partial z} \qquad (6)$$

$$w(x, z) = \frac{\partial(\phi_h + \phi_v)}{\partial z} + \frac{\partial(\psi_h + \psi_v)}{\partial x}$$

The stress tensor components are obtained using Hooke's law. Defining the terms

$$a_n^{xx} = (\lambda + 2\mu)\, k_n^2 + \lambda\, \nu_n^2 \qquad b_n^{xx} = 2\mu\, k_n\, \gamma_n \qquad (7)$$

$$a_n^{xz} = 2\mu\, k_n\, \nu_n \qquad b_n^{xz} = \mu\, [\, k_n^2 - \gamma_n^2 \,]$$

$$C_{np_l} = 2\, cos[k_n\, (x - x_{p_l})] \qquad S_{np_l} = -2i\, sin[k_n\, (x - x_{p_l})]$$

we obtain the displacements and tractions for each point *(x, z)* of the space for *(i)* a distribution of P_l horizontal forces regularly spaced along an interface l

$$u^h(x,z) = -iF \sum_{p_l=1}^{p_l=P_l} Q_{p_l}^h \left(-\gamma_o \, \xi_{op_l}^h + \sum_{n=1}^{n=M} C_{np_l} \left[k_n \, \kappa_{np_l}^h - \gamma_n \, \xi_{np_l}^h \right] \right) \tag{8}$$

$$w^h(x,z) = -iF \sum_{p_l=1}^{p_l=P_l} Q_{p_l}^h \left(\sum_{n=1}^{n=M} S_{np_l} \left[\nu_n \, \zeta_{np_l}^h + k_n \, \kappa_{np_l}^h \right] \right) \tag{9}$$

$$\sigma_{xx}^h(x,z) = -F \sum_{p_l=1}^{p_l=P_l} Q_{p_l}^h \left(\sum_{n=1}^{n=M} S_{np_l} \left[a_n^{xx} \, \kappa_{np_l}^h - b_n^{xx} \, \xi_{np_l}^h \right] \right) \tag{10}$$

$$\sigma_{xz}^h(x,z) = -F \sum_{p_l=1}^{p_l=P_l} Q_{p_l}^h \left(b_o^{xz} \, \chi_{op_l}^h + \sum_{n=1}^{n=M} C_{np_l} \left[a_n^{xz} \, \zeta_{np_l}^h + b_n^{xz} \, \chi_{np_l}^h \right] \right) \tag{11}$$

$$\sigma_{zz}^h(x,z) = -F \sum_{p_l=1}^{p_l=P_l} Q_{p_l}^h \left(\sum_{n=1}^{n=M} S_{np_l} \left[-b_n^{xz} \, \kappa_{np_l}^h + b_n^{xx} \, \xi_{np_l}^h \right] \right) \tag{12}$$

where

$$\kappa_{np_l}^h = \frac{k_n}{\nu_n} E_{np_l} + \frac{k_n}{\nu_n} R_{PP} \, T_{np_l} + R_{SP} \, V_{np_l} \tag{13}$$

$$\chi_{np_l}^h = -sign(z - z_{p_l}) \, G_{np_l} + R_{SS} \, U_{np_l} + \frac{k_n}{\nu_n} R_{PS} \, W_{np_l}$$

$$\zeta_{np_l}^h = sign(z - z_{p_l}) \frac{k_n}{\nu_n} E_{np_l} + \frac{k_n}{\nu_n} R_{PP} \, T_{np_l} + R_{SP} \, V_{np_l}$$

$$\xi_{np_l}^h = -G_{np_l} + R_{SS} \, U_{np_l} + \frac{k_n}{\nu_n} R_{PS} \, W_{np_l}$$

and *(ii)* for a distribution of P_l vertical forces

$$u^v(x,z) = -iF \sum_{p_l=1}^{p_l=P_l} Q_{p_l}^v \left(\sum_{n=1}^{n=M} S_{np_l} \left[k_n \, \kappa_{np_l}^v - \gamma_n \, \xi_{np_l}^v \right] \right) \tag{14}$$

$$w^v(x,z) = -iF \sum_{p_l=1}^{p_l=P_l} Q_{p_l}^v \left(\nu_o \, \zeta_{om} + \sum_{n=1}^{n=M} C_{np_l} \left[\nu_n \, \zeta_{np_l}^v + k_n \, \kappa_{np_l}^v \right] \right) \tag{15}$$

$$\sigma_{xx}^v(x,z) = -F \sum_{p_l=1}^{p_l=P_l} Q_{p_l}^v \left(a_o^{xx} \, \kappa_{om} + \sum_{n=1}^{n=M} C_{np_l} \left[a_n^{xx} \, \kappa_{np_l}^v - b_n^{xx} \, \xi_{np_l}^v \right] \right) \tag{16}$$

$$\sigma_{xz}^v(x,z) = -F \sum_{p_l=1}^{p_l=P_l} Q_{p_l}^v \left(\sum_{n=1}^{n=M} S_{np_l} \left[a_n^{xz} \, \zeta_{np_l}^v + b_n^{xz} \, \chi_{np_l}^v \right] \right) \tag{17}$$

$$\sigma_{zz}^v(x,z) = -F \sum_{p_l=1}^{p_l=P_l} Q_m^v \left(-b_o^{xz} \, \kappa_{om} + \sum_{n=1}^{n=M} C_{np_l} \left[-b_n^{xz} \, \kappa_{np_l}^v + b_n^{xx} \, \xi_{np_l}^v \right] \right) \tag{18}$$

where
$$\kappa^{v}_{np_l} = sign\,(z - z_{p_l})\, E_{np_l} - R_{PP}\; T_{np_l} + \frac{k_n}{\gamma_n}\, R_{SP}\; V_{np_l} \qquad (19)$$

$$\chi^{v}_{np_l} = \frac{k_n}{\gamma_n}\, G_{np_l} + \frac{k_n}{\gamma_n}\, R_{SS}\; U_{np_l} - R_{PS}\; W_{np_l}$$

$$\zeta^{v}_{np_l} = E_{np_l} - R_{PP}\; T_{np_l} + \frac{k_n}{\gamma_n}\, R_{SP}\; V_{np_l}$$

$$\xi^{v}_{np_l} = sign\;(z - z_{p_l})\, \frac{k_n}{\gamma_n}\, G_{np_l} + \frac{k_n}{\gamma_n}\, R_{SS}\; U_{np_l} - R_{PS}\; W_{np_l}$$

The forces applied on the upper and lower sides of an interface must insure the continuity of the displacement-traction field accross this interface. We define a displacement-traction vector $\mathbf{S}^{(m)}_{s,l} = [\; \mathbf{U}^{(m)}_{s,l}\; ;\; \mathbf{T}^{(m)}_{s,l}\; (\mathbf{n}^{(m)}_{l})\;]^{T}$, where

$\mathbf{U}^{(m)}_{s,l} = [\; u_x^{(m)}\; (x_{1_l}\; ,\; z_{1_l})\; ,\; ..\; ,\; u_x^{(m)}\; (x_{P_l}\; ,\; z_{P_l})\; ,\; u_z^{(m)}\; (x_{1_l}\; ,\; z_{1_l})\; ,\; ..\; ,\; u_z^{(m)}\; (x_{P_l}\; ,\; z_{P_l})\;]$ is the displacement vector and where $u_x^{(m)}\; (x_{p_l}\; ,\; z_{p_l})$ and $u_z^{(m)}\; (x_{p_l}\; ,\; z_{p_l})$ are the horizontal and vertical components of the displacement in medium m at each sampling point $(\; x_{p_l}\; ,\; z_{p_l}\;)$ of the interface l and produced by a source s located in medium m.

$\mathbf{T}^{(m)}_{s,l} = [\; T_x^{(m)}\; (x_{1_l}\; ,\; z_{1_l})\; ,\; ..\; ,\; T_x^{(m)}\; (x_{P_l}\; ,\; z_{P_l})\; ,\; T_z^{(m)}\; (x_{1_l}\; ,\; z_{1_l})\; ,\; ..\; ,\; T_z^{(m)}\; (x_{P_l}\; ,\; z_{P_l})\;]$ is the traction vector for which each component is defined as the product of the stress tensor $\underline{\sigma}$ induced by a source s acting in medium m by the unit vector $\mathbf{n}_l^{(m)}$ normal to the interface l and pointing outward relatively to medium m at the point $(\; x_{p_l}\; ,\; z_{p_l}\;)$.

i.e.
$$T_x^{(m)}\; (x_{p_l}\; ,\; z_{p_l}) = \sigma^{s}_{xx}\; (x_{p_l}\; ,\; z_{p_l})\; n^{(m)}_{x,l}\; (x_{p_l}\; ,\; z_{p_l}) + \sigma^{s}_{xz}\; (x_{p_l}\; ,\; z_{p_l})\; n^{(m)}_{z,l}\; (x_{p_l}\; ,\; z_{p_l}) \qquad (20)$$

$$T_z^{(m)}\; (x_{p_l}\; ,\; z_{p_l}) = \sigma^{s}_{xz}\; (x_{p_l}\; ,\; z_{p_l})\; n^{(m)}_{x,l}\; (x_{p_l}\; ,\; z_{p_l}) + \sigma^{s}_{zz}\; (x_{p_l}\; ,\; z_{p_l})\; n^{(m)}_{z,l}\; (x_{p_l}\; ,\; z_{p_l})$$

Assuming the existence of one or more source(s) in each medium, we have to solve the following linear matrix system.

$$\mathbf{S}^{(1)}_{1,1} + \underline{\mathbf{A}}^{(1)}_{1,1}\,\mathbf{Q}^{upper}_{1} = \mathbf{S}^{(2)}_{2,1} + \underline{\mathbf{A}}^{(2)}_{1,1}\,\mathbf{Q}^{lower}_{1} + \underline{\mathbf{A}}^{(2)}_{2,1}\,\mathbf{Q}^{upper}_{2} \qquad (21)$$

$$\mathbf{S}^{(2)}_{2,2} + \underline{\mathbf{A}}^{(2)}_{2,2}\,\mathbf{Q}^{upper}_{2} + \underline{\mathbf{A}}^{(2)}_{1,2}\,\mathbf{Q}^{lower}_{1} = \mathbf{S}^{(3)}_{3,2} + \underline{\mathbf{A}}^{(3)}_{2,2}\,\mathbf{Q}^{lower}_{2} + \underline{\mathbf{A}}^{(3)}_{3,2}\,\mathbf{Q}^{upper}_{3}$$

...

$$\mathbf{S}^{(l)}_{l,l} + \underline{\mathbf{A}}^{(l)}_{l,l}\,\mathbf{Q}^{upper}_{l} + \underline{\mathbf{A}}^{(l)}_{l-1,l}\,\mathbf{Q}^{lower}_{l-1} = \mathbf{S}^{(l+1)}_{l+1,l} + \underline{\mathbf{A}}^{(l+1)}_{l,l}\,\mathbf{Q}^{lower}_{l} + \underline{\mathbf{A}}^{(l+1)}_{l+1,l}\,\mathbf{Q}^{upper}_{l+1}$$

...

$$\mathbf{S}^{(L)}_{L,L} + \underline{\mathbf{A}}^{(L)}_{L,L}\,\mathbf{Q}^{upper}_{L} + \underline{\mathbf{A}}^{(L)}_{L-1,L}\,\mathbf{Q}^{lower}_{L-1} = \mathbf{S}^{(L+1)}_{L+1,L} + \underline{\mathbf{A}}^{(L+1)}_{L,L}\,\mathbf{Q}^{lower}_{L}$$

where

$\mathbf{S}^{(m)}_{m,l}$ is the displacement-traction vector acting on the sampling points of the interface l in medium m and due to the source located in medium m.

$\underline{\mathbf{A}}^{(m)}_{l1,l2}\,\mathbf{Q}^{upper}_{l1}$ is the displacement-traction vector acting on the sampling points of the interface $l2$ in medium m and due to the force distribution $\mathbf{Q}^{upper}$ applied on the upper side of interface $l1$.

$\underline{\mathbf{A}}^{(m)}_{l1,l2}\,\mathbf{Q}^{lower}_{l1}$ is the displacement-traction vector acting on the sampling points of interface $l2$ in the medium m and due to the force distribution $\mathbf{Q}^{lower}$ applied on the lower side of interface $l1$.

The coefficients of the matrix $\underline{\mathbf{A}}^{(m)}_{l1,l2}$ are deduced from equations (8) to (12), and (14) to (19). To solve this system leads us to determine the vectors $\mathbf{Q}_l = [\,\mathbf{Q}^{upper}_{l}\,;\,\mathbf{Q}^{lower}_{l}\,]$ which contain the unknown forces applied on the upper or lower sides of the interfaces $l = 1, \cdots, L$.

The general solution is given by the following recurrent procedure:

$$\mathbf{Q}_1 = \underline{\mathbf{a}}_1 \left(-\mathbf{S}^{(1)}_{1,1} + \mathbf{S}^{(2)}_{2,1} \right) + \underline{\mathbf{b}}_1 \mathbf{Q}_2^{upper} \qquad (22)$$

$$\text{with } \underline{\mathbf{a}}_1 = \left[\underline{\mathbf{A}}^{(1)}_{1,1} ; -\underline{\mathbf{A}}^{(1)}_{1,1} \right]^{-1} \text{ and } \underline{\mathbf{b}}_1 = \underline{\mathbf{a}}_1 \underline{\mathbf{A}}^{(2)}_{2,1}$$

$$\mathbf{Q}_2 = \underline{\mathbf{a}}_2 \left(-\mathbf{S}^{(2)}_{2,2} + \mathbf{S}^{(3)}_{3,2} - \underline{\mathbf{A}}^{(2)}_{1,2} \mathbf{Q}_1^{lower} \right) + \underline{\mathbf{b}}_2 \mathbf{Q}_3^{upper}$$

$$\underline{\mathbf{a}}_2 = \left[\underline{\mathbf{A}}^{(2)}_{1,2} \underline{\mathbf{b}}_1^{lower} + \underline{\mathbf{A}}^{(2)}_{2,2} ; -\underline{\mathbf{A}}^{(3)}_{2,2} \right]^{-1} \text{ and } \underline{\mathbf{b}}_2 = \underline{\mathbf{a}}_2 \underline{\mathbf{A}}^{(3)}_{3,2}$$

...

$$\mathbf{Q}_l = \underline{\mathbf{a}}_l \left(-\mathbf{S}^{(l)}_{l,l} + \mathbf{S}^{(l+1)}_{l+1,l} - \underline{\mathbf{A}}^{(l)}_{l-1,l} \mathbf{Q}_{l-1}^{lower} \right) + \underline{\mathbf{b}}_l \mathbf{Q}_{l+1}^{upper}$$

$$\underline{\mathbf{a}}_l = \left[\underline{\mathbf{A}}^{(l)}_{l-1,l} \underline{\mathbf{b}}_{l-1}^{lower} + \underline{\mathbf{A}}^{(l)}_{l,l} ; -\underline{\mathbf{A}}^{(l+1)}_{l,l} \right]^{-1} \text{ and } \underline{\mathbf{b}}_l = \underline{\mathbf{a}}_l \underline{\mathbf{A}}^{(l+1)}_{l+1,l}$$

...

$$\mathbf{Q}_L = \underline{\mathbf{a}}_L \left(-\mathbf{S}^{(L)}_{L,L} + \mathbf{S}^{(L+1)}_{L+1,L} - \underline{\mathbf{A}}^{(L)}_{L-1,L} \mathbf{Q}_{L-1}^{lower} \right)$$

$$\underline{\mathbf{a}}_L = \left[\underline{\mathbf{A}}^{(L)}_{L-1,L} \underline{\mathbf{b}}_{L-1}^{lower} + \underline{\mathbf{A}}^{(L)}_{L,L} ; -\underline{\mathbf{A}}^{(L+1)}_{L,L} \right]^{-1}$$

where $\underline{\mathbf{b}}_l$ is a $4P_l \times 2P_{l+1}$ matrix and $\underline{\mathbf{b}}_l^{lower}$ represents the $2P_{l+1} \times 2P_{l+1}$ square matrix extracted from the lower part of $\underline{\mathbf{b}}_l$. P_l is the number of sampling points of the interface l (figure IV.1).

IV.3 - Applications

IV.3.1 - *Tests of the method*

The displacement fields computed in the case of plane *P*- and *SV*-waves vertically incident upon the valley depicted in figure IV.2 are displayed in a contour map form figures IV.3 and IV.4. The medium configuration chosen (figure IV.2) corresponds to the low velocity contrast valley type *II* considered by Bard and Bouchon (1980b). In both figures IV.3 and IV.4 the left and the right hand sides show respectively the horizontal and the vertical components of the ground motion. The time window associated with the vertical axis is *15.0* seconds long and the station offsets are presented on the horizontal axis in kilometer units. The source time function is a Ricker wavelet having a characteristic period of *1.16* s. *(i)* In the case of the vertically incident plane *P*-wave (figure IV.3) we observe besides the direct arrival two surface wavetrains with a *1.2* Hz predominant frequency. These waves that travel across the basin with a phase velocity of *1.15* km/s have been generated at each edge of the valley and correspond to the

fundamental mode of the Rayleigh wave (see the phase velocity *vs.* frequency diagram given figure IV.5). This mode prevails in the diffracted field but the first higher mode of the Rayleigh wave slightly appears in the earlier part of the horizontal component. This phase has been emphasized by the thin broken line drawn on the horizontal map (figure IV.3). *(ii)* The diffracted field obtained in the case of the vertically incident plane *SV*-wave (figure IV.4) is more complex. This can be explained by the greater excitation of the first higher mode of the Rayleigh wave for an incident *SV*-plane wave. This mode well observed on the horizontal displacement component (*i.e.* The phase marked *1*), is reflected at the edges of the basin (*i.e.* see the mark *R1*). The amplitude of this horizontally polarized mode is now comparable to the amplitude of the fundamental mode that continues to prevail on the vertical component.

We now show a configuration that illustrates the completeness of the computed diffracted displacement field. The medium corresponds to the high velocity contrast valley type I (figure IV.6) defined by Bard and Bouchon (1980). The seismograms are computed over a time window of *23.5* seconds at *16* receivers and with a Ricker source time dependence having a *0.7* Hz central frequency. This frequency has been chosen for it corresponds to the valley *P*-wave fundamental resonance frequency $\alpha / 4h$. The elastic parameters of the model are given in figure IV.6. The source is a vertically incident plane *P*-wave. The seismograms are presented in figure IV.7. Besides the direct *P* arrival one can see two different types of propagating waves emphasized by the thin broken line signed *SP* and by the thick bold broken lines denoted *R1* and *R2*. The *SP* marked phase propagates with the basin *P*-wave velocity. It has a prevailing horizontal component and corresponds to the surface *P*-wave described by Lapwood (1949) and Bouchon (1978). This phase generated at the edge of the basin has an amplitude equal to two third the amplitude of the phases *R1*. The phases *R1* travelling across the basin with the *S*-wave velocity have a predominant vertical motion and correspond to two Rayleigh waves symetrically generated at the two edges of the basin. These two surface waves interfere at the center of the basin resulting in a strong increase of the Rayleigh pulse at the receiver *1* (see the mark *I1* figure IV.7). Each Rayleigh phase (*i.e. R1*) is reflected at each edge and backpropagates across the valley (see the mark *R2* figure IV.7), generating a new interference at the receiver *1* (see the mark *I2* figure IV.7).

IV.3.2 - *Effect of source location within the basin*

The medium considered now corresponds to the profile across the central region of the Yucca Flat valley, Nevada, given by Ferguson (1988). The basin interface used is an idealized interpolation of the interface between the Tertiary volcanic rocks and the Paleozoic basement. The basin is assumed to be only filled with Tertiary volcanic saturated materials. Neither the water table nor the alluvium layer are taken into account in the model in order to focus the attention on the influence of the source location within the basin on the displacement field at short distances. The medium geometry and the elastic parameters are those given by Ferguson (1988) and are depicted in figure IV.8. The four maximum slope angles observed from the left-hand side to the right-hand side of the basin interface are *21°*, *9°*, *6°*, and *40°*. Three explosions buried at *600* m depth (*i.e.* *A*, *B*, and *C*) are used for this study. The epicentral distances measured from explosion *B* are *20* km for receivers *1* and *11*, *14* km for receivers *2* and *10*, *8* km for receivers *3* and *9*, *4* km for receivers *4* and *8*, and *2* km for receivers *5* and *7*. The computed seismograms are displayed in figures IV.9a, IV.9b, and IV.9c for explosions *A*, *B*, and *C* respectively. The calculated time window is *15* seconds long and the source time function in displacement is a Ricker pulse having a *0.75* Hz central frequency. The seismogram displays have been normalized for each explosion (*i.e.* *A*, *B*, and *C*). The absolute amplitude scales are given at the left of each receiver for the *3* detonations to allow us to directly compare all the seismogram amplitudes.

The large maximum amplitude variations observed between the different configurations (*i.e.* the factor *2.58* observed at receiver *6* figure IV.9b) is due to the vicinity of the convex basement straight below explosion *B*. For this explosion the absolute amplitudes of the fields diffracted outside as well as inside of the basin are much greater than in the cases of explosions *A* and *C*. However the relative amplitudes (*i.e.* the ratios of the diffracted field over the maximum observed amplitude) are significantly smaller for explosion *B* than for the two other source locations. The extreme ratio values observed at receivers *1* and *11* are respectively *0.45* and *0.43*, *0.21* and *0.31*, and *0.37* and *0.53* for detonations *A*, *B*, and *C* respectively. These two amplitude behaviours mean that the diffracted field magnified by the vicinity of the interface is defocused by the convex region. This region induces a high lost of energy

by transmission in the underlying bedrock.

The field that propagates inside the basin in the case of explosion *C* is mainly composed of a well formed Rayleigh wavetrain (see the receivers *6*, *5*, and *4* figure IV.9c) and is magnified in the ascent region of the left-hand side of the basin (see the receiver *4* figure IV.9c). In the case of explosion *A* the surface wave is not as well generated and a wide-angle reflection merges with the Rayleigh wave at receiver *7* (figure IV.9a). The amplitude of the displacement fields emitted in the left-hand side of the basin by explosions *A* and *C* are comparable (see receivers *1*, *2*, and *3* figures IV.9a and IV.9c). But in the right-hand side of the basin (*i.e.* for the receivers *9*, *10*, and *11*) the displacement field amplitude for explosion *A* (figure IV.9a) is three fourth the one of explosion *C* (figure IV.9c). We can also noticed the longer duration of the explosion *A* diffracted Rayleigh wavetrain on the right hand side of the basin compared to the one generated by explosion *C*. This duration is associated with a slight frequency dispersion well observed on the vertical displacement components at receivers *8*, *9*, and *10* (figure IV.9a) and *2*, *3*, and *4* (figure IV.9c).

IV.3.3 - *Diffracted field by a multi–layered basin*

The source location influence is also related to the burying medium. Figure IV.10 depicts the new case studied. The model is a two layers basin with *34* receivers located on the surface. Three explosions (*A*, *B*, *C*) are detonated in the three media and the displacement fields generated are displayed in figures IV.11a, IV.11b, and IV.11c. The horizontal axes correspond to the station number and the oblique axes to the time window. The source time function is a Ricker wavelet having a *4* Hz central frequency. This value is two times the *P*- and four times the *S*-waves resonance frequencies of the first medium. The different phases observed are enhanced by the α, β, γ, γ^*, χ, and η arrows. The *T* arrow shows the shot point location.

Some of these phases are observed for explosion *A* (figure IV.11a). The surface wave η, well seen on the vertical component, corresponds to the diffraction of the explosion direct field at the left edge of the basin. The α and β phases correspond respectively to the surface *P*-wave and to the Rayleigh wave diffracted out of the left

side of the basin. After a *1*s duration gap of ground motion and following the β phase, a broadened phase, denoted γ, appears with the velocity of the β phase. Since it only appears out of the left hand side of the basin the phase γ (and γ* as will be seen later in figures IV.11b and IV.11c) must result from two successive *P*-head waves. *(i)* A *P*-head wave propagating along the first interface from the shot point region to the right hand side of the basin is transmitted into the second medium. *(ii)* This wave is diffracted by the right basin edge which generates the Rayleigh wave χ (well seen in figures IV.11b and IV.11c) and the second *P*-head wave that backpropagates along the second interface from the right side to the left side of the basin where it rises up as the phase γ. In the cases of explosions *B* (figure IV.11b) and *C* (figure IV.11b), the phase γ is weaker but is followed by a stronger phase denoted γ*. This late phase results from two successive *P*-head waves. These two head waves both propagate along the second interface before reaching the at the left side of the basin as the γ* phase. The phase α is the direct *P*-wave in the case of explosion *C* for which the phase β has a negligible amplitude.

> . . . La suite du texte ne fait pas partie de l'article. Nous voulons ici décrire plus finement le comportement du champ de déplacement suivant la forme du bassin . . .

IV.4 - Influence de la forme du bassin

Nous analysons les modifications du champ de déplacement à des distances inférieures à *10* km qui sont dues à la forme des bassins sédimentaires. Deux vallées *a* et *b* décrites figure IV.12 sont étudiées. Les pentes maximales du modèle *a* sont *27°* à gauche et *38°* à droite. Pour le modèle *b* les pentes maximales de gauche à droite sont *38°*, *15°*, et *38°*. Les variations du champ de déplacement induites par le changement de forme du bassin sont étudiées pour *7* capteurs placés en surface. La source est une explosion effectuée dans la partie gauche des bassins à *350* m de profondeur. Les sismogrammes correspondants sont présentés figure IV.13. La configuration milieu-stations y est donnée pour chaque modèle avec en superposition une fenêtre de *6* s dans laquelle sont représentées les composantes horizontales et verticales des déplacements enregistrés par chaque récepteur. Les amplitudes absolues sont données au dessus des stations. La fonction source utilisée est un Ricker de fréquence centrale *2* Hz supérieure

à la fréquence de résonnance de l'onde *P*. En bas à gauche une légende résume les notations utilisées dans la suite du texte. Pour mieux décrire les mouvements du sol, chaque sismogramme est décomposé en deux parties. La partie I correspond aux premières arrivées (*i.e.* à gauche du trait épais coupant la fenêtre en deux sous-fenêtres). La partie II correspond au reste des sismogrammes.

IV.4.1 - *Description des sismogrammes*

Trois régions sont définies dans le champ de déplacement présenté figure IV.13. La première région à gauche du bassin concerne les capteurs *1* et *2*. Les premières arrivées y montrent un fort déplacement à composante verticale prédominante, précédé par une phase émergente dans le cas du modèle *a* et par une phase horizontale plus forte et impulsive dans le cas du modèle *b*. La partie II dans cette région montre, pour le bassin *a*, un mouvement de plus faible amplitude que la partie I. Pour le bassin *b* la partie II domine globalement les sismogrammes. La deuxième région groupe les récepteurs *6* et *7*. La durée des sismogrammes y est plus longue. L'onde R_g est clairement générée après propagation dans le bassin *a* et visible au début des ondes de surface des capteurs *6* et *7*. Cette phase apparaît moins clairement pour le modèle *b*, du moins apparaît-elle avec une plus faible amplitude. Le déplacement maximum se situe dans la troisième région qui contient les capteurs *3*, *4*, et *5*. Ce maximum apparaît sur la composante verticale du capteur *5* du modèle *a* tandis qu'il est observé sur la composante horizontale du récepteur *3* du modèle *b* (figure IV.13). L'amplitude maximale est observée pour les deux modèles dans les premières arrivées des sismogrammes. En résumé, si globalement la durée des signaux est allongée par la propagation dans le bassin, les phases observées et leurs amplitudes sont fortement influencées par la forme du milieu.

Nous allons donc décrire les mouvements de particules et comparer la nature des champs de déplacements diffractés par les deux vallées sédimentaires. Les mouvements de particules sont présentés figures IV.14 et IV.15 pour respectivement les parties I et II des modèles *a* et *b*. Chaque dessin est composé de deux niveaux relatifs aux deux modèles étudiés. La représentation orthonormale permet de corréler directement les angles de polarisations avec les différentes pentes des bassins. Les angles de polarisation

sont mesurés entre l'axe horizontal et le grand axe des mouvements elliptiques.

IV.4.2 - *Mouvements des particules*

IV.4.2.a - *Partie I des sismogrammes*

Le récepteur *3* modèle *a* (figure IV.14) montre un mouvement de particule elliptique incliné à *45°*. Cette polarisation permet d'identifier la phase correspondante comme une onde *P* réfléchie grand angle sur la pente gauche du bassin (Aki et Richards 1980). L'angle de réflexion est de *72,6°* (l'angle critique de réflexion étant de *41°*). La réflexion s'est produite à *235* m de profondeur sur une pente de *27,6°*. Dans le modèle *b* le récepteur *3* (figure IV.14b) montre un mouvement elliptique incliné à *28°* correspondant à une onde *P* inhomogène rayonnée par l'interface à proximité du récepteur *3* (Lapwood, 1949). Les contenus fréquentiels des déplacements enregistrés au capteur *3* pour le modèle *a* et pour le modèle *b* sont décrits figure IV.16. Cette figure résume les mouvements horizontaux et verticaux, les mouvements de particules et les spectres de déplacements normalisés pour les deux fenêtres étudiées. Dans le modèle *a* la fréquence centrale de la partie I est voisine de 2 Hz, fréquence de la source, alors que pour le modèle *b* la fréquence centrale est *2,6* Hz. Ceci confirme la nature différente des ondes observées.

Pour les deux modèles (figure IV.14) les récepteurs *5* ont des mouvements de particules similaires présentant une ellipse inclinée à *70°* précédée par un mouvement elliptique de plus faible amplitude incliné à *49°* qui peut correspondre à l'onde *P* cônique rayonnée dans la partie plate des deux bassins. Le mouvement elliptique majeur est associé au rayonnement en onde *S* de l'onde *P* d'interface. Une ellipse de grande amplitude inclinée à *52°* décrit l'émergence simultanée de l'onde réfléchie et de l'onde *P* cônique qui suivent l'arrivée du champ direct au capteur *4* modèle *a*. Pour le modèle *b*, cette station a un comportement différent avec un mouvement triangulaire horaire qui suit immédiatement l'arrivée directe. Ce mouvement de particule est induit par la partie creuse du bassin et entraine une augmentation importante de l'accélération aux instants des points de rebroussement du mouvement de particule (capteur *4* figure IV.14b). Les récepteurs *1*, *2*, *6*, et *7* enregistrent la propagation d'une onde de Rayleigh caractérisée

par son mouvement elliptique. L'amplitude de cette onde de surface est importante comparée à celle de l'onde directe pour le modèle *a* (Voir les récepteurs *1* et *2* par exemple). Par contre son amplitude est réduite pour devenir égale à l'amplitude du champ direct pour le modèle *b*.

IV.4.2.b - *Partie II des sismogrammes*

Les mouvements de particules de la deuxième partie des sismogrammes sont présentés figure IV.15 pour les modèles *a* et *b*. Les mouvements décrits par le sol sont préférentiellement des ellipses verticales pour les deux modèles. Les formes de polarisation sont similaires sauf pour le capteur *4*. Les ellipses anti-horaires de grandes amplitudes des capteurs *6* et *7* correspondent à l'onde R_g observée figure IV.13a. Ces ellipses se finissent par un mouvement quasi circulaire que l'on peut observer avec une amplitude comparable pour les deux modèles. Le déplacement maximum apparaît au récepteur *3* du modèle *b* et vaut *1,5* fois celui du capteur *3* du modèle *a*. Pour ce capteur les fréquences prépondérantes sont *3,25* Hz et *2,4* Hz pour le bassin *a* et pour le bassin *b* respectivement (figure IV.16).

Conclusion

Nous avons développé la méthode de discrétisation des nombres d'ondes, utilisée ici pour la résolution des équations intégrales aux frontières, pour le calcul de sismogrammes en présence de vallées alluviales à stratifications multiples et irrégulières. La méthode matricielle de détermination du champ de forces est détaillée dans le cas général d'un ensemble de sources ponctuelles de distribution quelconque. Dans les applications traitées, l'influence du site environnant la source a été analysée jusqu'à des distances d'une dizaine de kilomètres. Suivant la configuration source *vs.* milieu de propagation, différents effets de défocalisation, d'amplification et de dispersion des ondes ont été mis en évidence. Nous avons montré comment des ondes rétropropagées sous un bassin peuvent allonger la durée des mouvements du sol, nous avons également détaillé les variations de ces mouvements avec les variations de la forme des bassins.

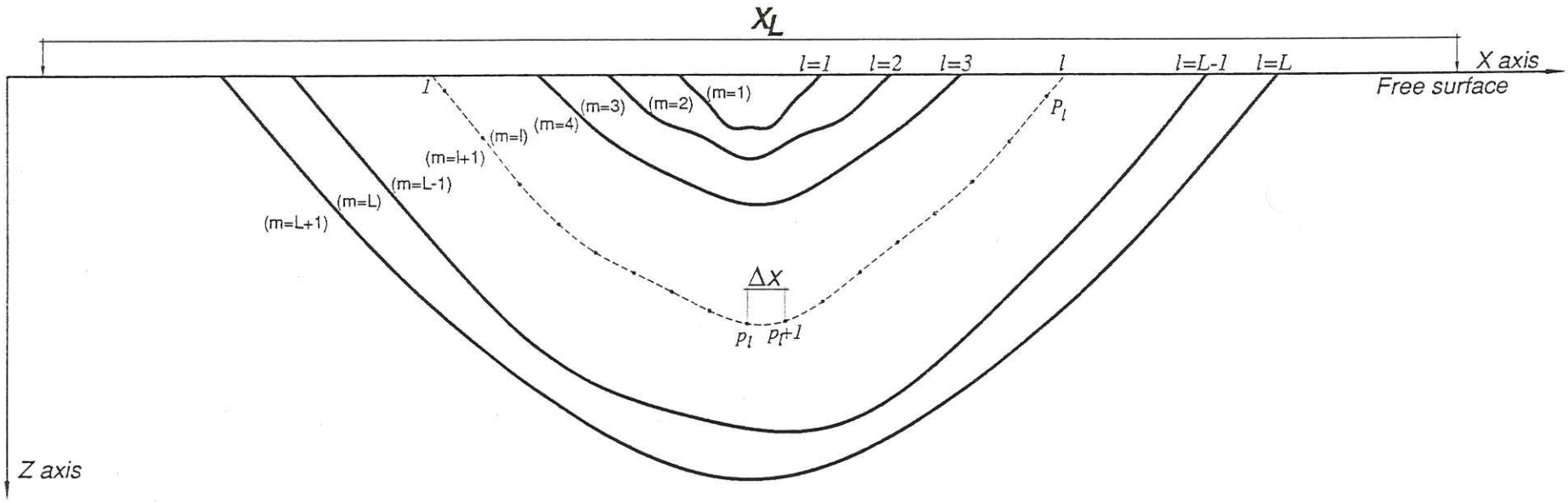

Fig. IV.1 - Geometry of the medium and description of the different notations. The medium is described by $l = 1 \ldots L$ interfaces defining $m = 1 \ldots L + 1$ layers. The interface sampling step is Δx along the x axis. The periodicity of the medium is X_L (Explanations in text).

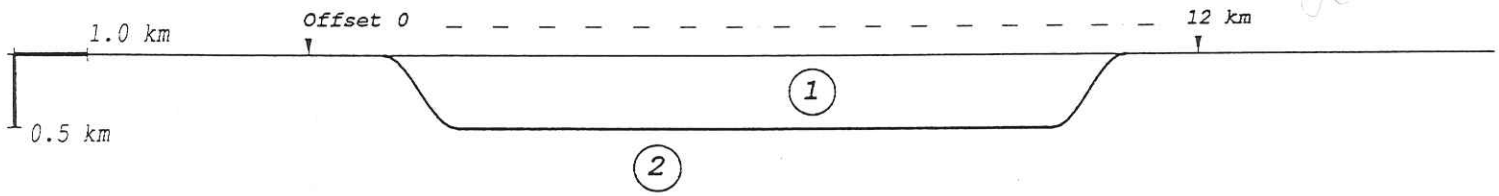

Medium	α (km/s)	β (km/s)	ρ (g/cm^3)	ν
1	2.000	1.100	2.200	0.28
2	5.000	2.800	2.800	0.27

Source: Incident plane wave

Fig. IV.2 - Medium geometry for the first computation and location of the receiver area from the offset *0* to the offset *12* km. The medium is made up of a thin and flat sedimentary valley whose elastic parameters are summarized in the table. The medium *1* corresponds to the valley, and the medium *2* to the underlying bedrock.

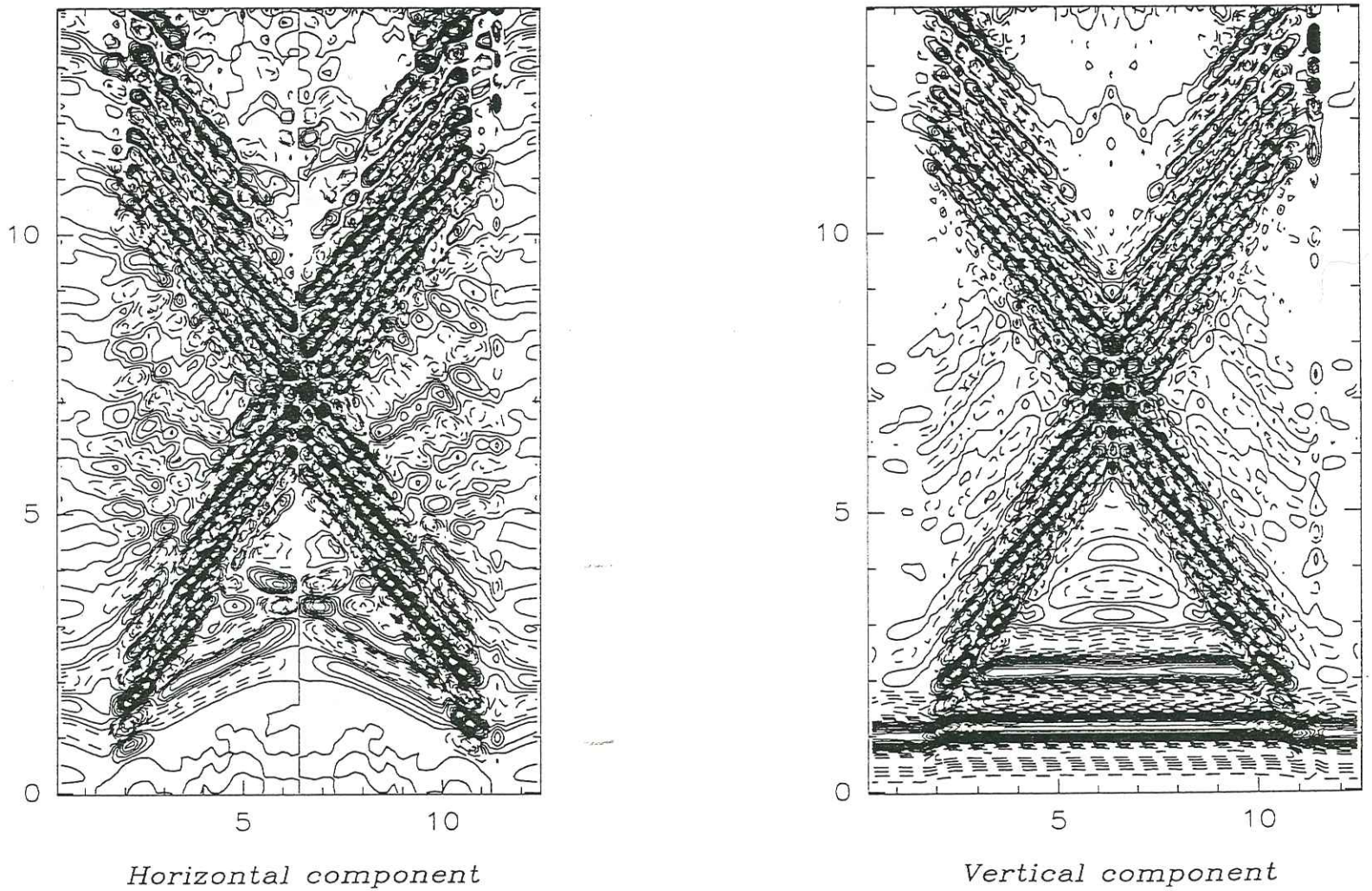

Fig. IV.3 - Contour map displays for the horizontal (Left) and the vertical (Right) motions recorded by the receivers depicted figure IV.2. The source is a vertically incident plane *P*-wave. The Ricker has a period of *1.16* s.

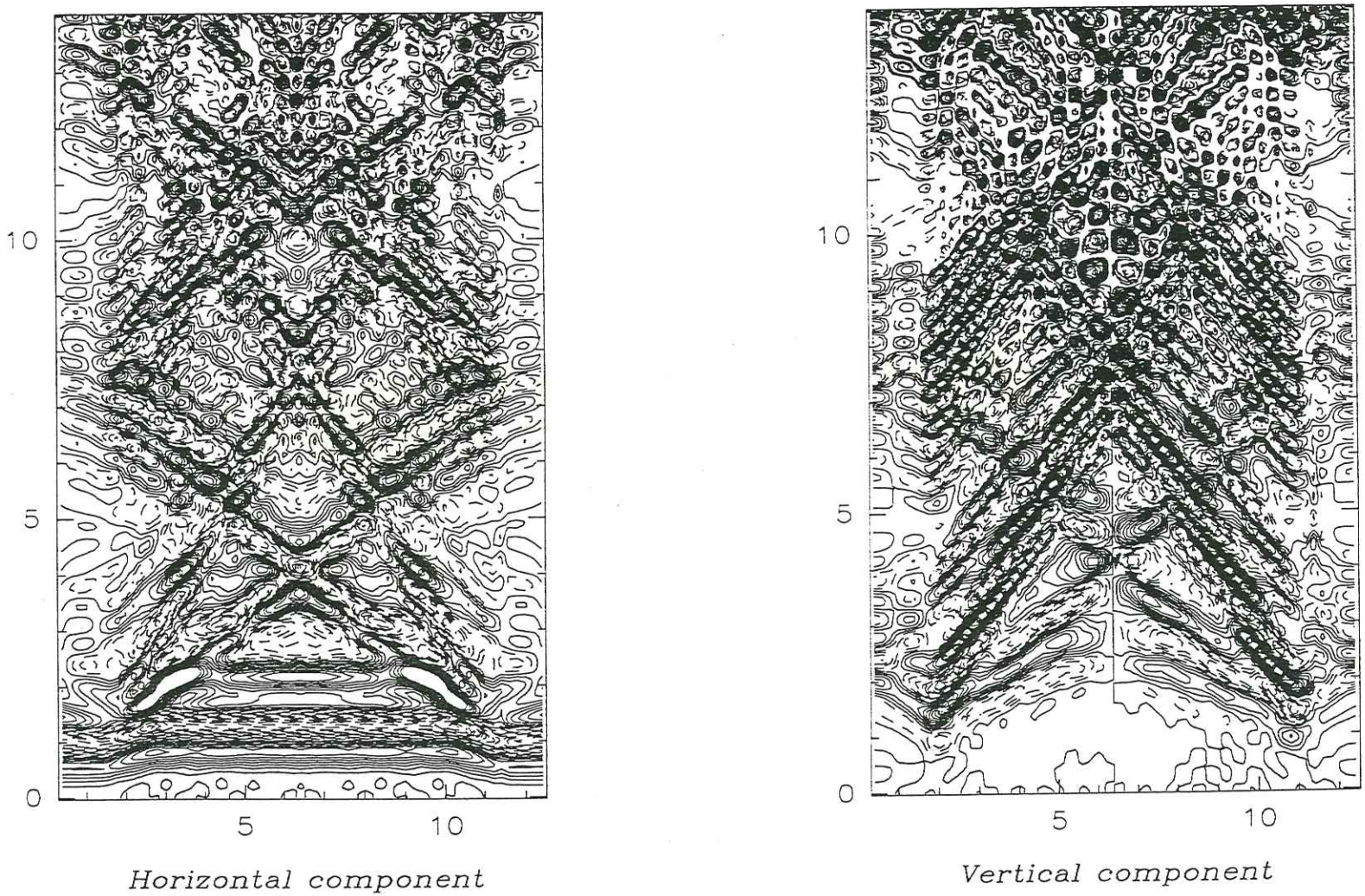

Fig. IV.4 - Same as figure IV.3 for a vertically incident plane *SV*-wave.

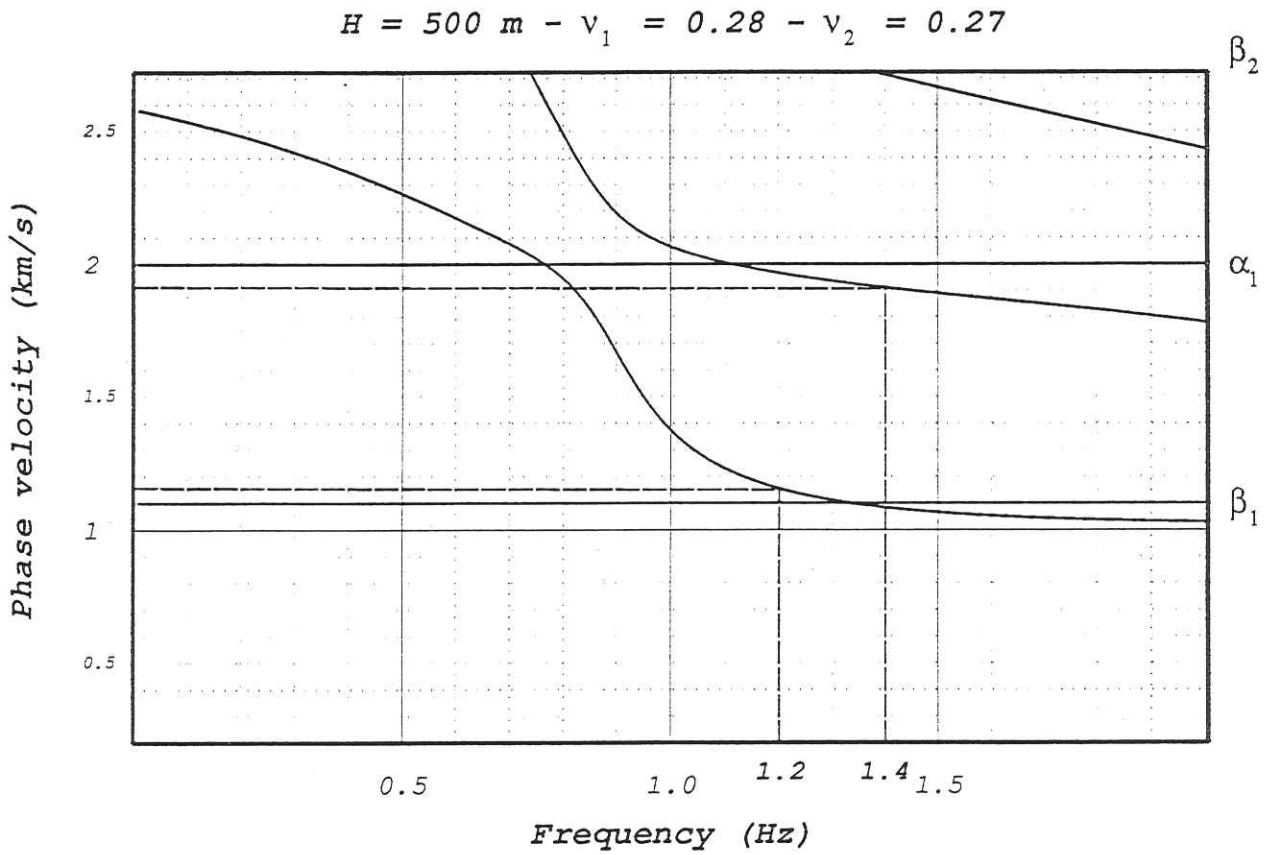

Fig. IV.5 - Phase velocity *vs.* frequency diagram computed for a medium equivalent to the medium given figure IV.2 and made up of a layer having a thickness of *0.5* km overlying a half space. The elastic characteristics of the layer and of the half space are the same as the one described figure IV.2. We have plotted the *1.15* km/s and the *1.9* km/s phase velocity positions at *1.2* Hz and *1.4* Hz that correspond respectively to the fundamental and to the first higher modes of the Rayleigh wave observed on both vertical contour maps of the figures IV.3 and IV.4.

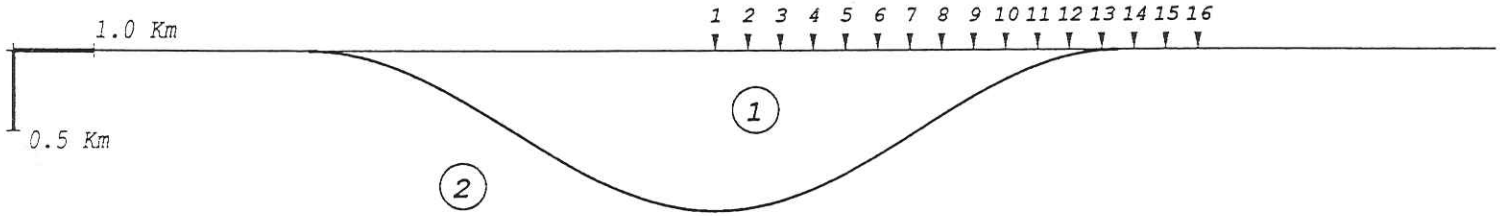

Medium	α (km/s)	β (km/s)	ρ (g/cm^3)	ν
1	1.400	0.700	2.000	0.33
2	6.062	3.500	3.300	0.25

Source: Incident plane wave

Fig. IV.6 - Medium geometry and location of the *16* receivers. The medium is made up of a sediment-filled valley whose elastic parameters are summarized in the table. The notation are the same as in figure IV.2.

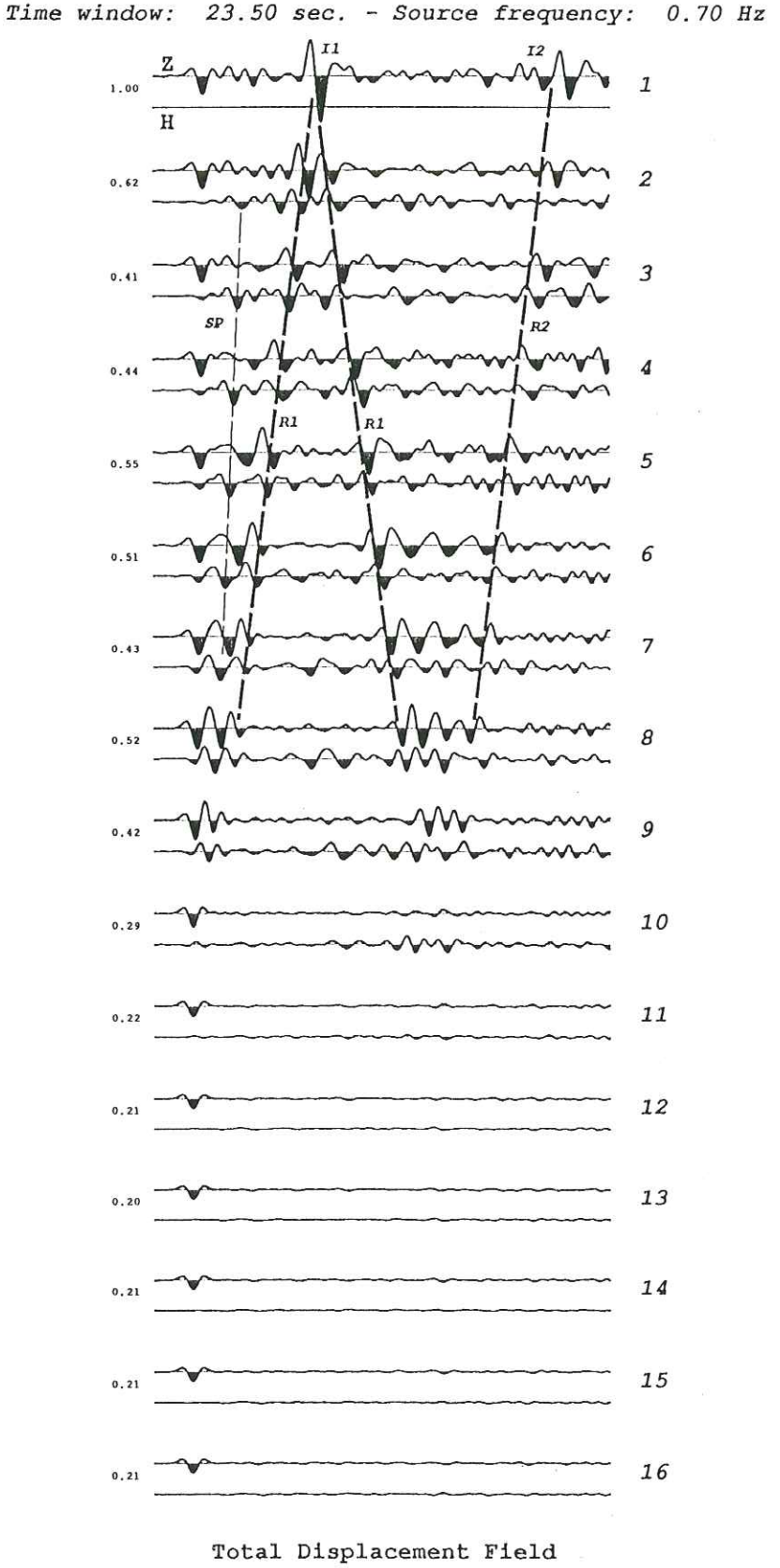

Fig. IV.7 - Blacknening representation of the horizontal *H* and vertical Z displacement components recorded at the *16* receivers displayed figure IV.6. The time duration is *23.5* s long and the Ricker frequency equals *0.7* Hz. See the explanations in the text concerning the notation *I1*, *I2*, *R1*, and *R2*.

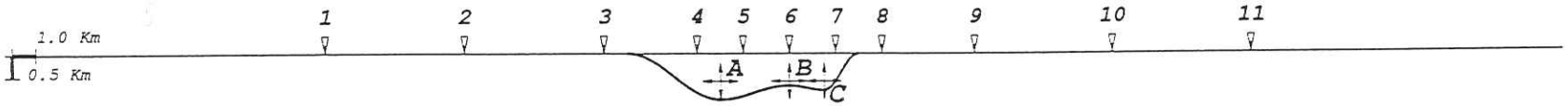

Medium	α (km/s)	β (km/s)	ρ (g/cm^3)	γ
1	3.000	1.600	1.790	0.30
2	4.570	2.640	2.500	0.25

Explosions A, B, and C location

Fig. IV.8 - Medium geometry and location of the *11* receivers considered for the next calculation.

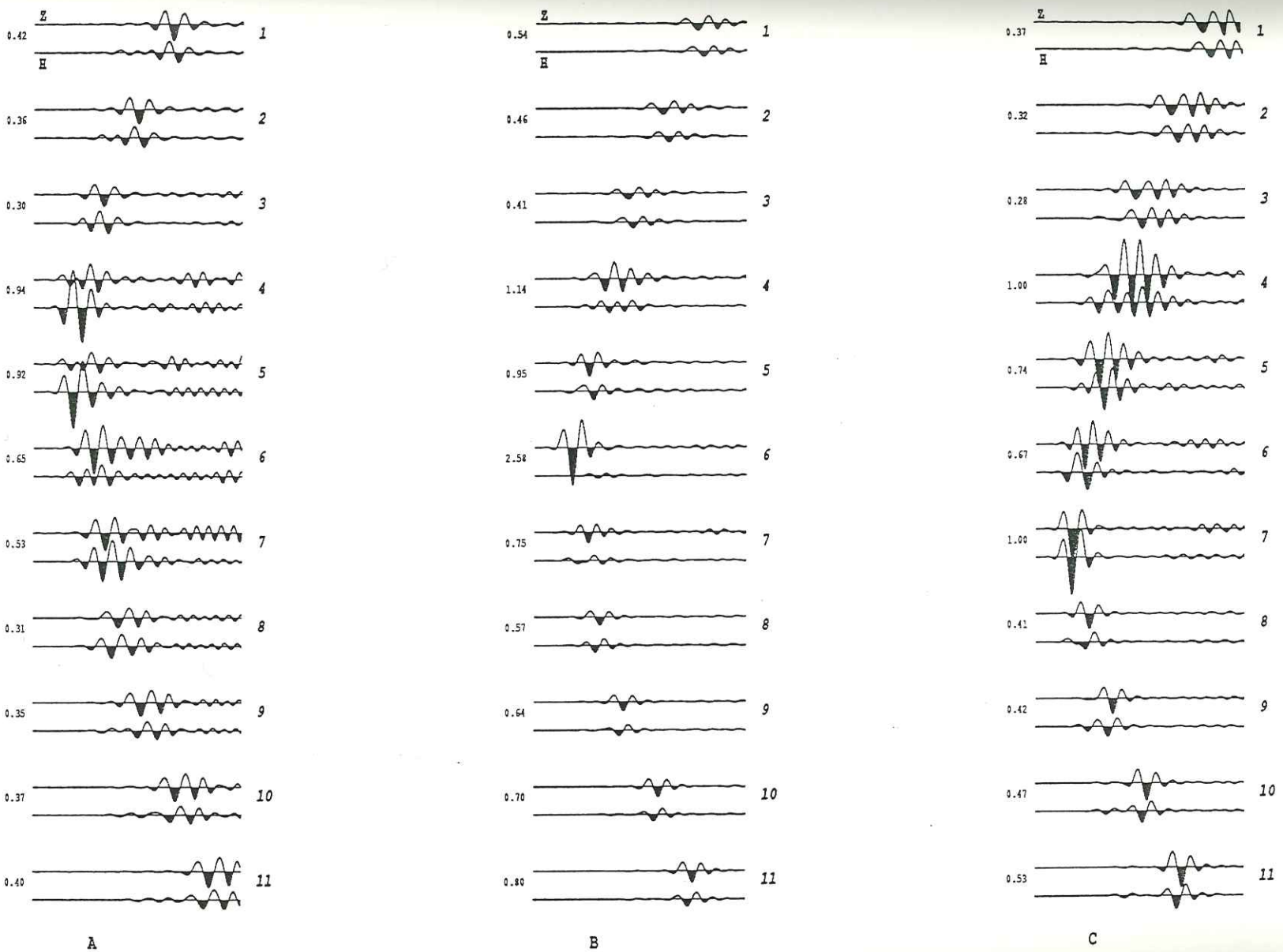

Fig. IV.9 - Blacknening display of the horizontal *H* and vertical *Z* motions computed at the *11* receivers. The time window lasts for *15* s. The Ricker frequency is *0.75* Hz. For each explosion the seismograms are drawn with relative amplitudes. The absolute ones are written for the explosions *A*, *B*, and *C*.

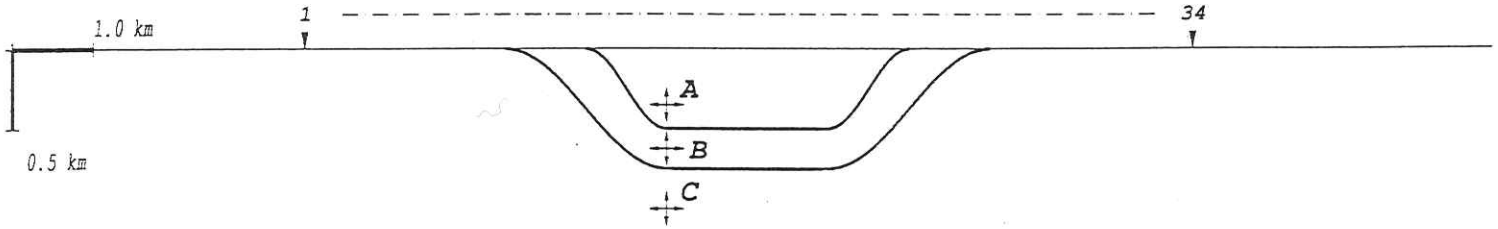

Medium	α (km/s)	β (km/s)	ρ (g/cm^3)	ν
1	3.600	2.000	2.000	0.28
2	4.400	2.500	2.300	0.26
3	5.717	3.300	2.600	0.25

Source: Explosion

Fig. IV.10 - Two layered medium geometry and location of the *34* receivers. The three explosions considered are signed *A*, *B*, and *C* in the first, second and third media.

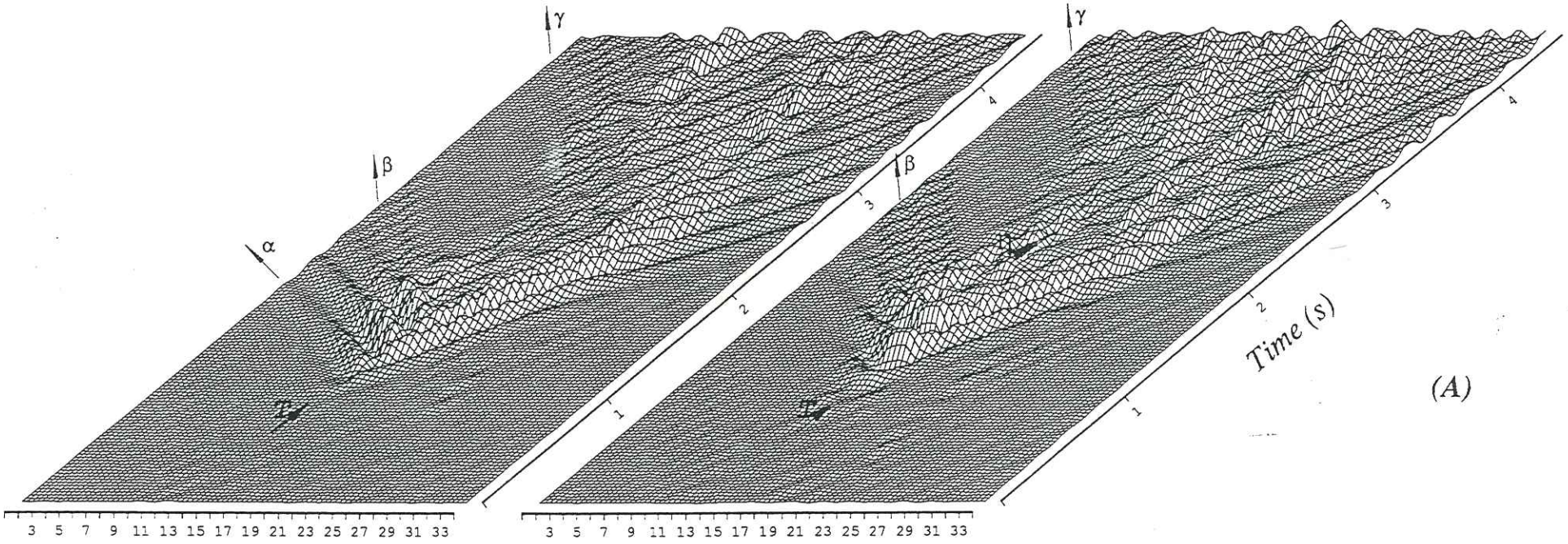

Receivers

Horizontal component

Receivers

Vertical component

Fig. IV.11a - Time *vs.* distance horizontal and vertical displacement nappes for the explosion *A*. The main phases prolonged by the α, β, γ, γ*, χ, and η arrows are described in the text. The shot point is enhanced by the *T* arrow.

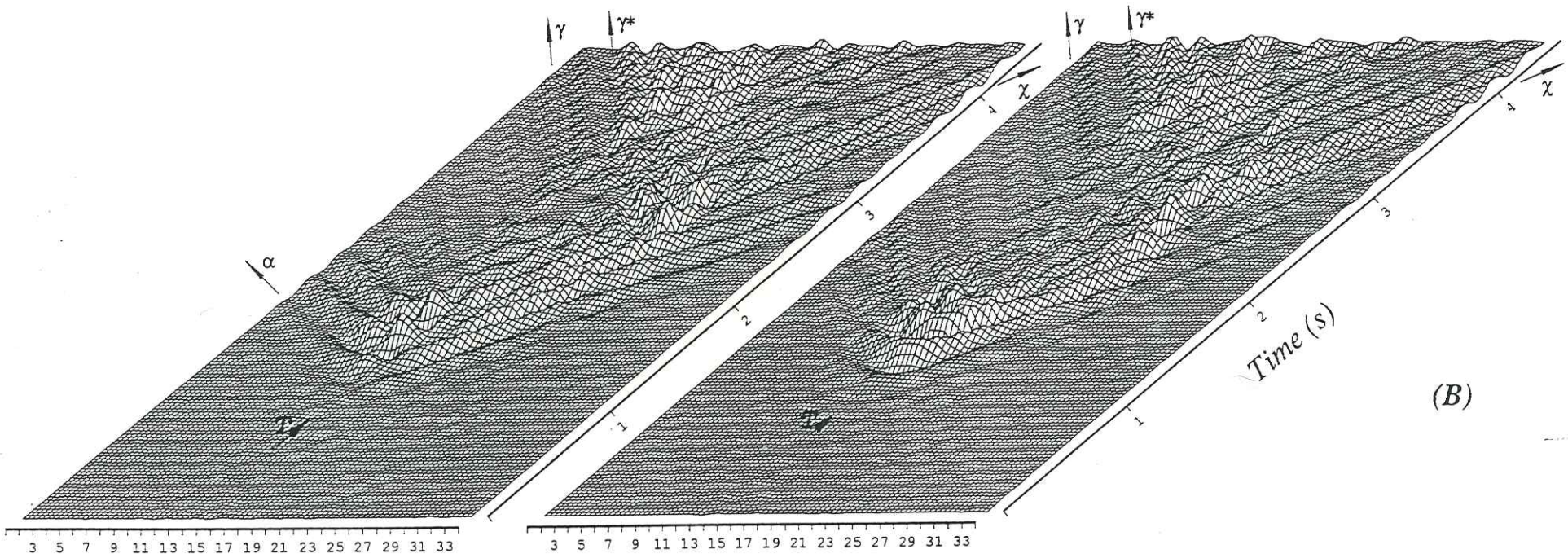

Receivers

Horizontal component

Receivers

Vertical component

Fig. IV.11b - Same as figure. IV.11a for the explosion *B*.

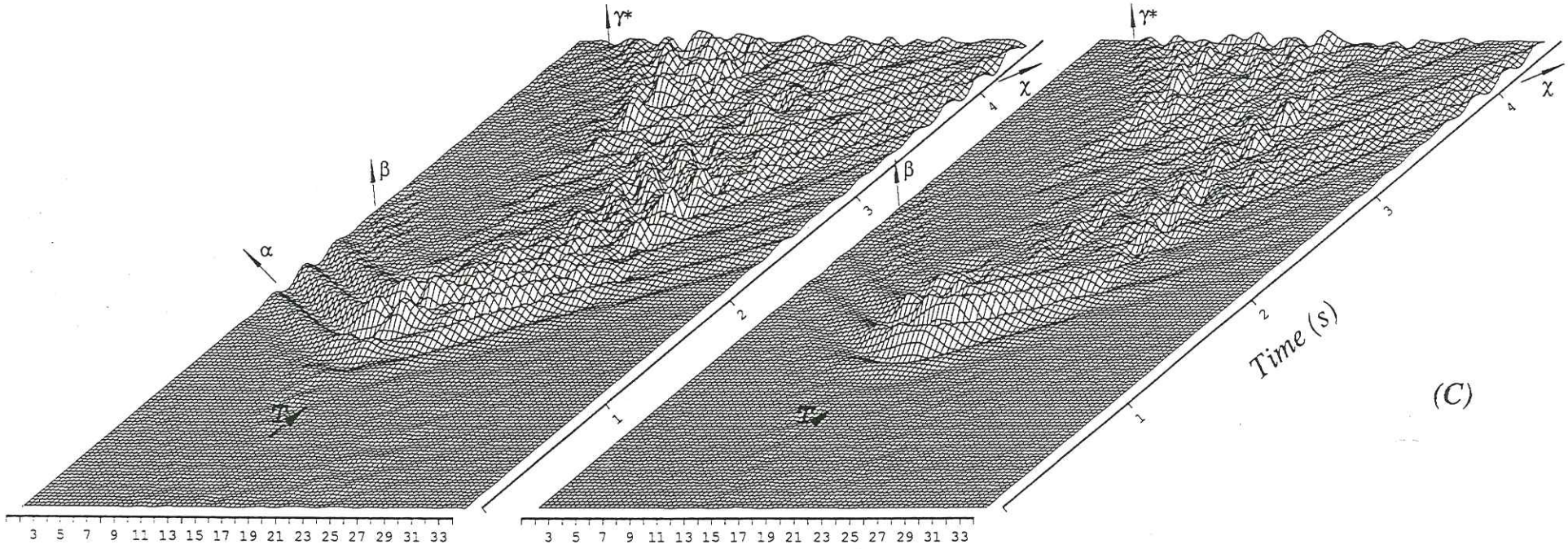

Receivers
Horizontal component

Receivers
Vertical component

Fig. IV.11c - Same as figure IV.11a for the explosion *C*.

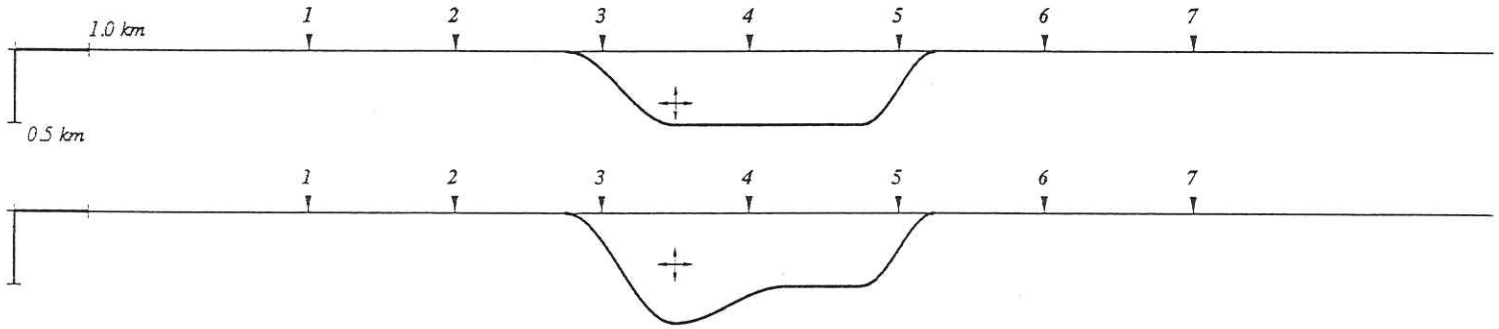

Medium	α (km/s)	β (km/s)	ρ (g/cm^3)	ν
1	3.000	1.600	1.790	0.30
2	4.570	2.640	2.500	0.25

Source: Explosion

Fig. IV.12 - Configuration des milieux *a* et *b* et positions des 7 capteurs.

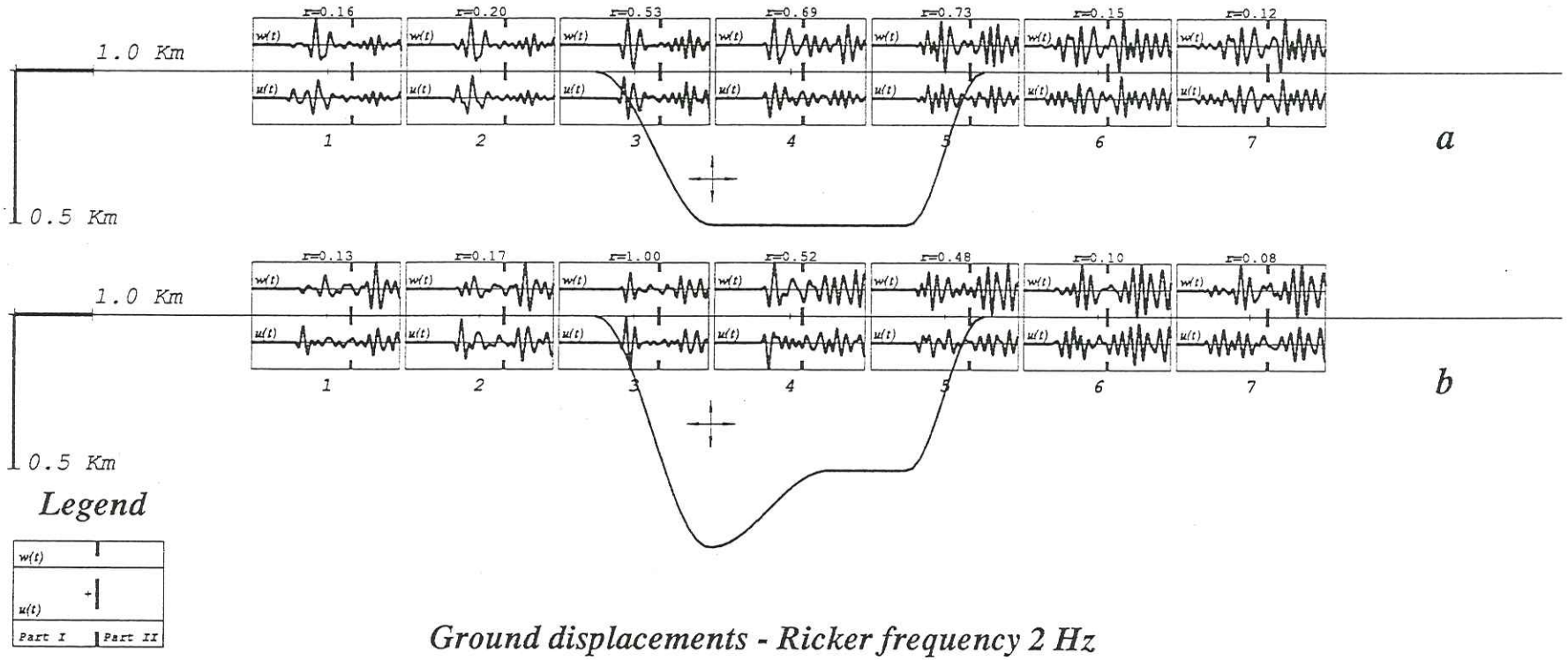

Fig. IV.13 - Représentation composite de la configuration du milieu défini figure IV.12 et des composantes horizontales et verticales des déplacements enregistrés aux 7 capteurs. La fréquence de la source est 2,0 Hz. Le trait vertical épais scinde les sismogrammes en deux parties I et II (voir texte) correspondants aux premières arrivées et aux arrivées plus tardives.

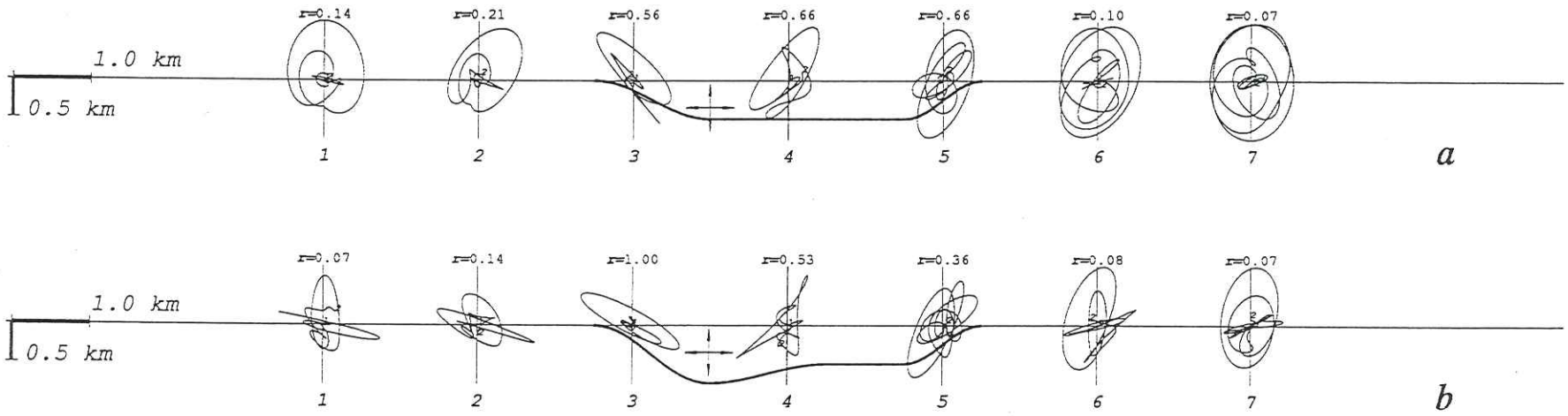

Particle motions of the first arrivals - Ricker frequency 2 Hz

Fig. IV.14 - Représentation des mouvements de particules correspondants aux premières arrivées pour les modèles *a* et *b* définis figure IV.12. La représentation est orthonormale. Les échelles sont données à gauche de chaque représentation. Les amplitudes correspondent au déplacement radial maximum enregistré par chaque capteur.

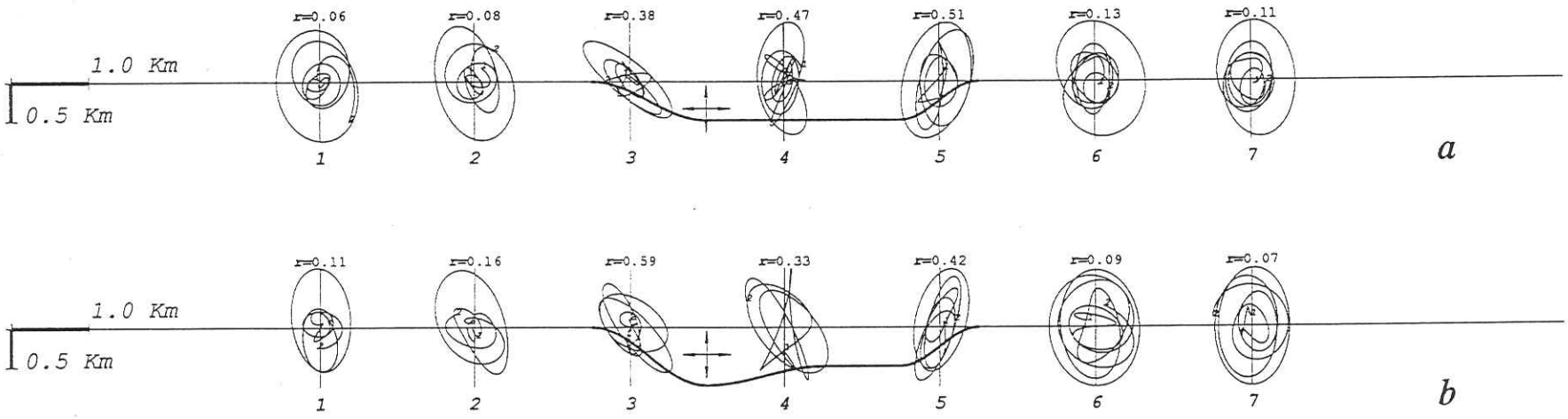

Particle motions of the later arrivals - Ricker frequency 2 Hz

Fig. IV.15 - Représentation des mouvements de particules correspondants aux arrivées tardives pour les modèles *a* et *b* définis figure IV.12. La représentation est orthonormale. Les échelles sont données à gauche de chaque représentation. Les amplitudes correspondent au déplacement radial maximum enregistré par chaque capteur dans cette fenêtre de temps.

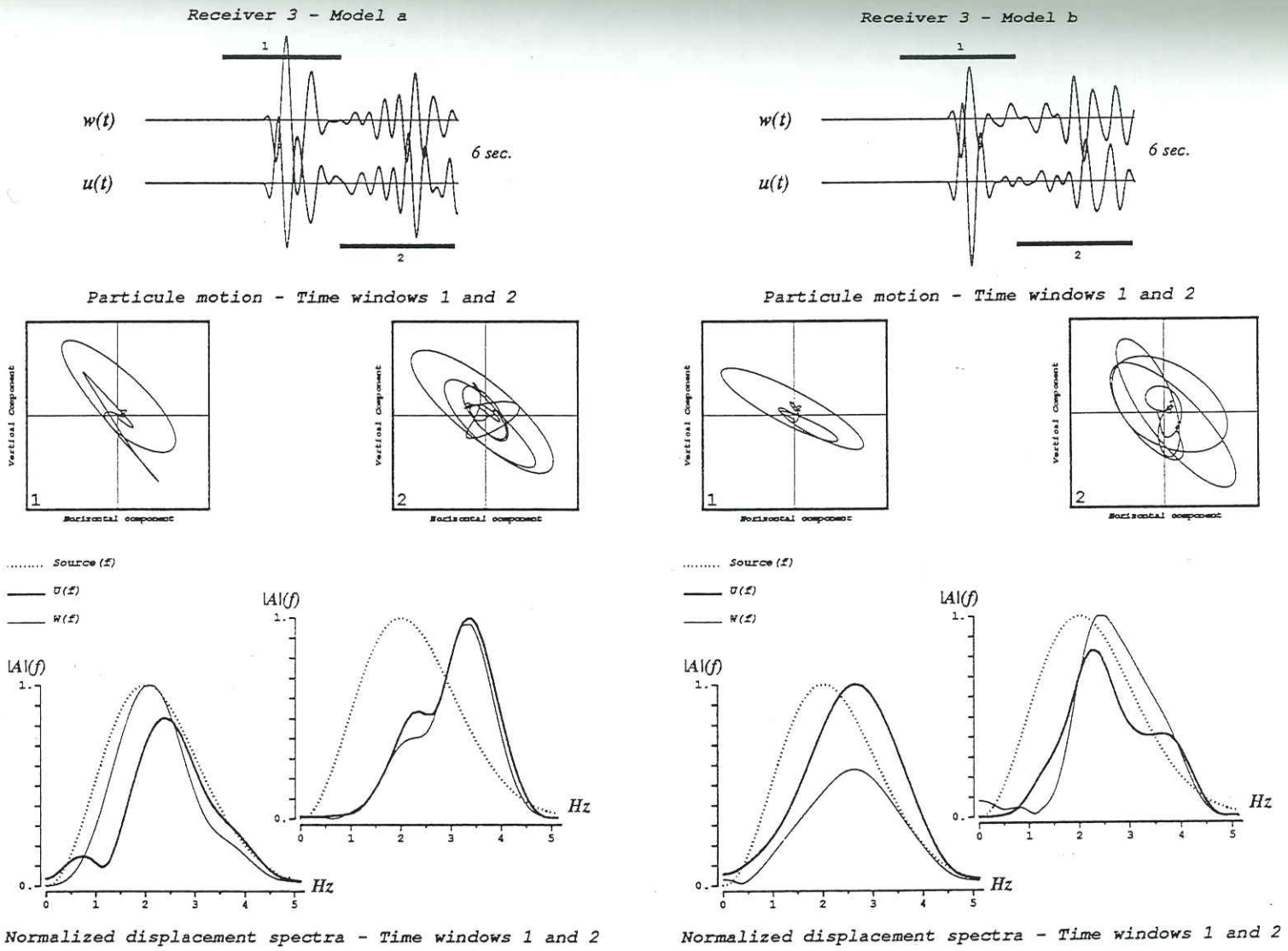

Fig. IV.16 - Déplacements horizontaux et verticaux (en haut), mouvements de particule (milieu), et spectres normalisés (en bas) pour les fenêtres de temps I et II étudiées pour le capteur *3* dans le cas du modèle *a* (à gauche) et du modèle *b* (à droite). Le spectre de la source (pointillé) est normalisé à 1. Les composantes horizontales, *U*, et verticales, *W*, sont normalisées par rapport au maximum des deux composantes pour chaque fenêtre.

- V -

Far-field effects due to geological structures located in the vicinity of buried explosions.

Prepared to be submitted to the *Bull. Seism. Soc. Am.*

Résumé

Nous avons construit les sismogrammes synthétiques en champ lointain et déterminé un ordre de grandeur des variations sur l'estimation de l'énergie des tirs en fonction de leurs positions. Les tirs considérés ont été effectués dans la partie centrale du bassin de Yucca Flat au Nevada et ont été enregistrés par le réseau sismique du L. D. G. Les signaux ont été calculés en utilisant le théorème de réciprocité et la méthode de discrétisation des nombres d'ondes pour résoudre de façon exacte le problème des intégrales aux frontières intervenant pour la construction des signaux dans le bassin irrégulier de Yucca Flat. Nous avons mis en évidence différents effets qui portent sur la forme des signaux calculés et sur l'estimation des magnitudes. Ces effets ont été corrélés d'une part aux hétérogénéités structurales présentes dans le milieu de tir et d'autre part au fonctionnement de la source elle-même. Malheureusement, la comparaison directe entre les signaux calculés et les signaux observés n'a pas été faite car le calcul sur le modèle complet de Yucca Flat n'a pas encore pu être entrepris.

V.1 - Introduction

Many works have started to study the displacement amplitude variations observed at teleseismic distances. These variations have been correlated to scattering by the structure heterogeneities in the vicinity of the source region (Cleary *et al.*, 1975; Bouchon, 1976; McLaughlin *et al.*, 1987; Ferguson, 1988; McLaughlin and Jih, 1988). They also have been attributed to the physical properties (*e.g.* density, porosity, water or oil saturation, etc.) of the source medium taken into account in the source function modelling (Werth and Herbst, 1963; Boardman *et al.*, 1964; Hasegawa, 1971, 1972; Mueller and Murphy, 1971, 1972; Power, 1974). The purpose of this paper is to balance the structure heterogeneity and the source medium property contributions to the farfield displacement using synthetic models. The discrete wavenumber-boundary integral equation method (Bouchon and Aki, 1977; Bouchon *et al.* 1989) is used to study these effects on the radial farfield response of geological structures. We study here the source region effects that we have to take into account when we analyse Yucca Flat nuclear detonations, Nevada Test Site, recorded from the French L.D.G. network.

V.2 - Method of computation

The farfield displacement is assumed to result from the convolution of the source function, *i.e.* $s(\tau)$, by the propagation path response, *i.e.* $p(\tau)$, by the receiver and source site functions, *i.e.* $c(\tau)$, and by the recording system response, *i.e.* $a(\tau)$. Thus

$$r(t) = s(\tau) * p(\tau) * c(\tau) * a(\tau)$$

Different formulations of the source function $s(\tau)$ have been derivated in term of *(i)* the reduced displacement potential

$$\psi(t) = \psi(\infty) \left[1 - e^{-kt} \left\{ 1 + kt + a_1(kt)^2 + a_2(kt)^3 + a_3(kt)^4 \right\} \right],$$

where $a_1 = 1/2$, $a_2 = 1/6$, $a_3 = -B$ in the Haskell model (1967) inducing a ω^{-4} high-frequency dependency. Two modified forms have been proposed by von Seggern and Blandford (1972) with $a_1 = -B$ and $a_2 = a_3 = 0$ and a ω^{-2} high-frequency behaviour, and by Helmberger and Hadley (1981) with $a_1 = 1/2$, $a_2 = -B$, and $a_3 = 0$, corresponding to an intermediate shape between the Haskell and the von Seggern and Blandford models. The B constant is related to the spallation effect (Viecelli, 1973 ; Aki *et al.*, 1974), and k should be related to the yield as $W^{-1/3}$.

(ii) Another source formulation is the one given by Mueller and Murphy (1971). This model takes into account both the yield and the detonation depth. The model scaling factors depending on the medium of burial are empirically determined for different source environments (Murphy, 1977). Power (1974) modified the Mueller and Murphy (1971) scaling theory using a computer code that simulate underground nuclear explosions in tuff with various free porosities and water densities.

The first few seconds of the teleseismic observations at distances of approximately $80°$ essentially consists of the paths (*e.g.* P or pP) that take place in the mantle. The attenuation of these paths are described with the Futterman (1962) inelastic attenuation formulation. Thus in the frequency domain the path is modeled by

$$p(f) = \exp\left[-\pi f t^* \left(1 - \exp\frac{-f}{f_o} \right) \right] \exp\left[-2i\pi f t^* \left(Q - \frac{1}{\pi} Log_e \frac{\varepsilon}{f_o} \right) \right] \exp\left[2if t^* Log_e f \right]$$

where t^* is defined as $t^* = \int_{path} \frac{Q^{-1}}{v} ds$ and represents the ray path-integrated effect of the mantle quality factor Q, f_o is the frequency above which dispersion occurs in the mantle ($f_o > 0$), and ε is the Euler constant. In the *0.2 - 5* Hz frequency band the t^*_α value is estimated in the *0.1 - 0.8* range (Frasier and Filson, 1972; Cormier, 1982; Der and Lees, 1985). In the time domain the mantle transfert function is for each frequency $f \gg f_o$ equal to the convolution of *3* terms, *i.e.*

$$p(t\ ;f) = \frac{2t^*}{\pi\,(t^{*2} + 4t^2)} * \delta\left[t - (Q - \frac{1}{\pi} Log_e \frac{\varepsilon}{f_o})\, t^*\right] * \delta\left[t + \frac{t^*}{\pi} Log_e f\right]$$

Where the first time t function is an amplitude scaling depending on t^*, the second term corresponds to a delay pulse, and the last term represents the frequency dispersion function with a phase advance for $f > 1$ Hz and a delay phase for $f < 1$ Hz.

The French L.D.G. network short period recording system response is mainly a function of the seismometer response for the other different recording filters (*i.e.* the third order Bessel filter frequency modulator and the anti-aliasing Chebychev filter) have flat and linear responses in the studied frequency band 0.2 Hz $\leq f \leq 5$ Hz. Thus the recording system displacement response in the frequency domain is

$$a(f) = \frac{-f^3}{(f^2 - f_c^2) + 2i\beta f_c f}$$

where f_c is the characteristic frequency of the seismometer, and $\beta = 1 / \sqrt{2}$ the damping factor .

Different numerical methods have been investigated to study the influences of the near source site heterogeneities on the teleseismic *P*-wave seismograms. If the lateral heterogeneities in the source region have effects at teleseismic distances on the magnitude m_b estimates that can be averaged or canceled indeed by a network of stations at multiple azimuths, these source site structure are of great importance for thin aperture observations (McLaughlin *et al.*, 1987, McLaughlin and Jih, 1988). Hasegawa (1971 and 1972) using a composite method connects the recorded seismograms shape to the geological complexity of the source environments. Bouchon (1976) links the

Thomson-Haskell method (Thomson, 1950; Haskell, 1953) with the reciprocity theorem and shows the great influence of the source depth and of the burying medium on the m_b estimates for events in layered media. Aki-Larner (1970) calculations for Yucca Flats explosions (Ferguson, 1988), and other empirical or data analysis methods (Taylor, 1983; Lay and Welc, 1987; Lay 1987a and 1987b) have been processed to emphasize the near source structure effect on the farfield displacement records.

The near source structure effects are hereafter computed using the discrete wavenumber-boundary integral equation method associated to the reciprocity theorem. This discrete wavenumber method has been previously described and developped in the *P*, *SV*, and *SH* cases to study the effect of laterally varying media onto the field diffracted at a few tens of kilometers of the source (Bouchon and Aki, 1977; Bouchon *et al.*, 1989; Gaffet and Bouchon, 1989, 1990). We study the farfield source environment influence and therefore ignore the receiver structures for such a problem had been the subject of a great deal of works which give prominence and describe the wave diffraction effects observed on teleseismic recordings that are due to the topography (Key, 1967; Bouchon, 1973; Sánchez-Sesma and Rosenblueth, 1979; Bard, 1982; Kawase and Aki, 1988, 1989, and 1990) or to underground structures (Bard and Bouchon, 1980 and 1985) located near the seismometer.

V.3 - Numerical experiment

A profile turned toward the French L. D. G. network has been infered from the Paleozoic basement depths obtained by Taylor (1983), Ferguson *et al.* (1988) and McLaughlin *et al.* (1987) for the Yucca flat valley. In the aim to determine the influence of the different layers, the basin was firstly made up of a wet tuff rocks filling (model *a*), and then with a wet tuff volcanic rocks underlying a dry alluvium filling (model *b*). A third model should take into account the dry tuff level (*i.e.* the water table) but hasn't been yet processed for computation long duration. The model *b* and the elastic parameters are depicted figure V.1. The crosses indicate the true depths of the two interfaces considered. The horizontal scale gives the distance in kilometer from an arbitrary origin. *11* detonations are studied and described in the table V.1. The map figure V.2 displays their repartition nearly *SW-NE* along the profile given figure V.1.

Table V.1

No	Event names	Date	Time	° N	° W	Depth	m_b
1	**PYRAMID**	16 *Apr* 1980	20 00 00.1	37 06 04	116 01 50	**579** *m*	**5.3**
2	**JORNADA**	28 *Jan* 1982	16 00 00.1	37 05 29	116 03 04	**640** *m*	**5.9**
3	**TURQUOISE**	14 *Apr* 1983	19 05 00.1	37 04 22	116 02 45	**533** *m*	**5.7**
4	**MUNDO**	01 *May* 1984	19 05 00.1	37 06 22	116 01 21	**567** *m*	**5.3**
5	**CAPROCK**	31 *May* 1984	13 04 00.1	37 06 11	116 02 53	**600** *m*	**5.8**
6	**BRETON**	13 *Sep* 1984	14 00 00.0	37 05 12	116 04 16	**483** *m*	**5.0**
7	**HERMOSA**	02 *Apr* 1985	20 00 00.1	37 05 41	116 01 56	**640** *m*	**5.7**
8	**GLENCOE**	22 *Mar* 1986	16 15 00.1	37 04 59	116 03 58	**600** *m*	**5.1**
9	**TAJO**	05 *Jun* 1986	15 04 00.1	37 05 54	116 00 56	**500** *m*	**5.3**
10	**GASCON**	14 *Nov* 1986	16 00 00.1	37 06 02	116 02 53	**600** *m*	**5.8**
11	**BULLFROG**	30 *Aug* 1988	18 00 00.1	37 05 09	116 04 07	**500** *m*	**5.0**

V.3.1 - *Medium shape effect*

The explosions have been projected onto the profile and the layout shows *4* events at the same location and different depths (*i.e. Breton* (*483* m), *Bullfrog* (*500* m), *Turquoise* (*533* m), and *Glencoe* (*600* m)) and a set of *7* events from west to east (*resp. Jornada*, *Gascon*, *Caprock*, *Hermosa*, *Pyramid*, *Tajo*, and *Mundo*). The signals averaged on the L. D. G. network are presented figure V.3 in the *0.5 - 2.5* Hz frequency band. The averaging allows us to minimize the noise and to obtain the signals for a receiver having a flat frequency response (but an unknown magnification constant). The flatness has been verified by comparing the average events with the signals recorded at stations having known flat responses in the considered frequency band (*i.e.*, MFF, LFF, LPO; Lemenager, 1982).

The mean observing distance is *80°* from Yucca Flat and corresponds to an angle of incidence from the source region of *16.95°* (Pho and Behe, 1972). Synthetic

seismograms have been computed over a *10* s duration window at such a distance for the simple basin *a* and for the two layered basin *b*. The results are respectively presented on the left and right columns of the figure V.4. The farfield basin impulsive response has been convolved with the non frequency dispersive Ricker function at *1* Hz. The time domain maximum displacement amplitude increases with the depth of burial for the both models (See *Breton*, *Bullfrog*, *Turquoise*, and *Glencoe*). The general feature observed is the amplitude increase from west and from east up to *Pyramid* in connection with the depth of the basin bottom. This shape effect is magnified by the presence of the alluvium layer for which the maximum displacement location always remains at *Pyramid* location. The seismograms are all the more broadened because the alluvium deposit thickens. *Tajo* and *Mundo* don't show significant variations between the two models for the too thin alluvium coverage above them.

V.3.2 - *Influence of the yield*

We now compute the seismograms that should be recorded in France for the *11* assumed fully coupled detonations and for yields of *20* kt and *120* kt. The Mueller-Murphy source (1971) is used with the parameters corresponding to the wet tuff-rhyolite medium of burial (Murphy, 1977). The t^* value is *0.7* (Cormier, 1982). The frequency responses are presented figure V.5 and the resulting signals (*i.e.* $s(\tau) * p(\tau) * a(\tau)$) are displayed in the two bottom boxes for an infinite space having the characteristics of the wet tuff layer. The main frequencies are *1* Hz and *0.7* Hz for respectively the *20* kt and the *120* kt shots at *500* m depth. These two source functions have then been convolved with the Yucca Flat farfield response of the model *b* to obtain the seismograms displayed figure V.6. The solutions for a half space source medium are superimposed in dotted lines. Besides the computed seismograms of *Tajo* and *Mundo* which are scarcely modified in comparison with the half space solution, the common feature is an enlargement of the *pP*-wave. For the both yields, the amplitude increases while the depth of the Paleozoic basement decreases, the maximum amplitude being recorded in the camber region in the eastern part of the valley. If the amplitude seems to be correlative to the external shape of Yucca Flat, it appears that the frequency of the maximum amplitude has to be related to the thickness of the alluvium. The figure V.7

sums up these results. This display depicts the Δm_b predicted by the synthetic data. The Δm_b values correspond to $Log_{10}(A_{event\ k} / T) - \left[Log_{10}(A_{event\ R} / T) \right]_{max}$, difference between the magnitude of each detonation k with a reference event R which predicts the maximum magnitude. The general behaviour of the maximum amplitude is similar for the two yields with a Δm_b variation well correlated to the Paleozoic basement shape and a regular decrease of the period of the maximum amplitude with the thinning of the alluvium. A source effect is clearly shown for the explosions *6* (*Breton*), *11* (*Bullfrog*), *3* (*Turquoise*), and *8* (*Glencoe*) for which the Δm_b behaviour is reversed when the yield increases. Thus for small yields (*e.g.* around *20* kt) the displacement amplitude decreases with the depth of burial while it increases for big yields (*e.g.* around *120* kt).

We can apply these synthetic Δm_b variations to estimate the correlative yield miss-estimation. Different formulas may be used to estimate the yield in the Yucca Flat test region, *i.e.*

$$m_b = 3.79 + 0.85\ Log_{10}\ W \qquad \text{(Murphy, 1977)} \qquad (1)$$

$$m_b = 3.71 + 0.89\ Log_{10}\ W \qquad \text{(Bache, 1982)} \qquad (2)$$

These two relations can be summarized by $m_b = a + b\ Log_{10}\ W$. Thus on the one hand, if the observed magnitude $m_{b,\,obs}$ is smaller than the magnitude $m_{b,\,true}$ corresponding to the true value of the yield W_{true}, the miss-estimated percentage of the yield is

$$|\Delta W| / W_{true} = 1 - 10^{\frac{-|\Delta m_b|}{b}}$$

For instance, if $\Delta m_b = -0.25$ the underestimated yield is half times the true yield. On the other hand, if the observed magnitude $m_{b,\,obs}$ is greater than the magnitude $m_{b,\,true}$, the miss-estimated percentage of the yield is given by

$$|\Delta W| / W_{true} = 10^{\frac{|\Delta m_b|}{b}} - 1$$

Thus for $\Delta m_b = +0.25$, the estimated yield is almost 2 times the true yield. The b values

proposed in the relations 1 and 2 are close together so that the predictive yield estimation effects are similar for both magnitude *vs.* energy relations.

Conclusion

We have implemented the discrete wavenumber-boundary integral equation method to compute the radial farfield response of structure heterogeneities in the source region. The computation have been processed using the reciprocity theorem to simulate *11* underground explosions occured in the central region of the Yucca Flat valley, Nevada, and recorded in France. We have shown the strong influence of the nature and of the shape of the basin filling. On the one hand, the maximum displacement amplitudes are connected together with the shape of the valley while on the other hand the corresponding frequency is correlative to the thickness of the alluvium deposit. The m_b anomalies determined in this work would be used to reduced the uncertainty in the yield estimations made with data obtained from a thin aperture network. The complete model which hasn't yet been implemented (*i.e.* the model *c*) should increase the model *b* amplitude behaviour and should lengthen the first arrivals registered for the events occured in the eastern part of the valley where the dry tuff level is the thickest.

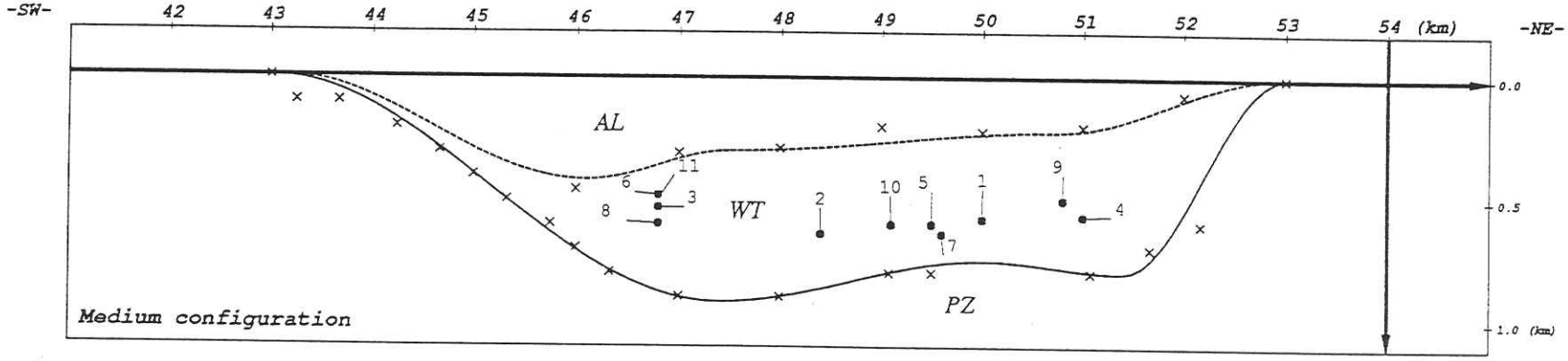

Medium	α (km/s)	β (km/s)	ρ (g/cm³)	ν
AL	1.340	0.640	1.800	0.35
WT	3.000	1.600	1.800	0.30
PZ	4.570	2.640	2.500	0.25

]*a*]*b*

Fig. V.1 - Geometry of the Yucca Flat valley infered from the model given by Ferguson *et al.* (1988). The basin *a* is assumed to be formed with a wet tuff layer (*WT*) overlying a semi infinite space made up of Paleozoic sediments (*PZ*). The elastic parameters are sumed up in table with the bracket *a*. The model *b* takes into account the alluvial deposits (*AL*) and corresponds to the bracket *b*. The explosions numbered from *1* to *11* in the table IV.1 are depicted by the black circles in the tuff level. The horizontal scale is given in kilometers from an arbitrary origin.

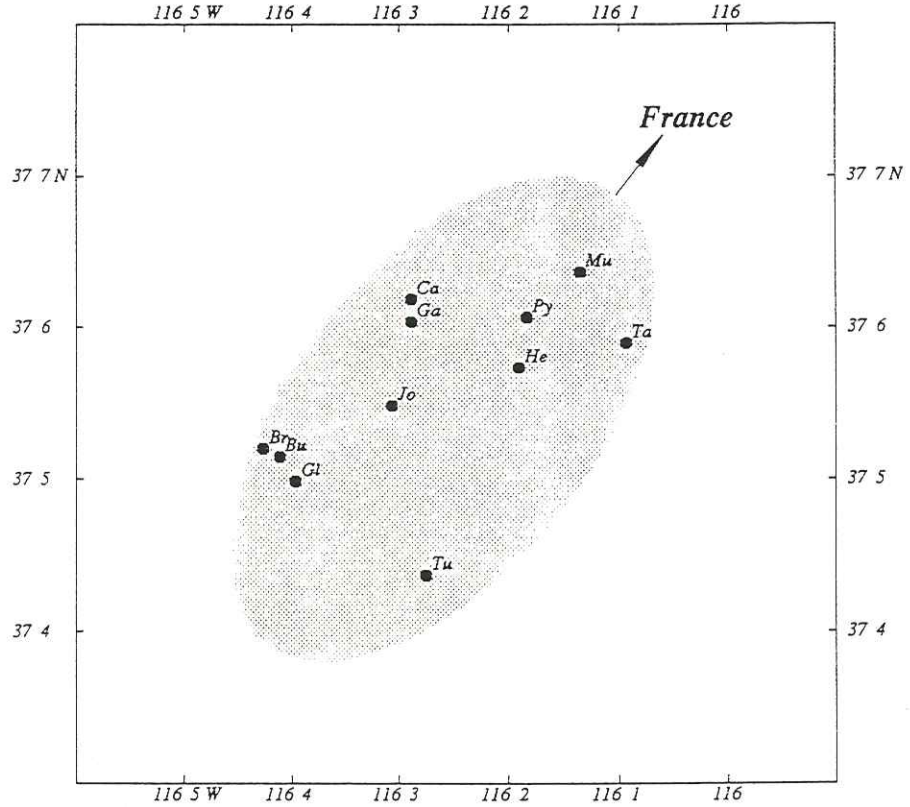

Yucca Flat events map

Fig. V.2 - Simplified map of the studied events. The gray ellipse is plotted to emphasize the global distribution of the events roughly turned toward the France.

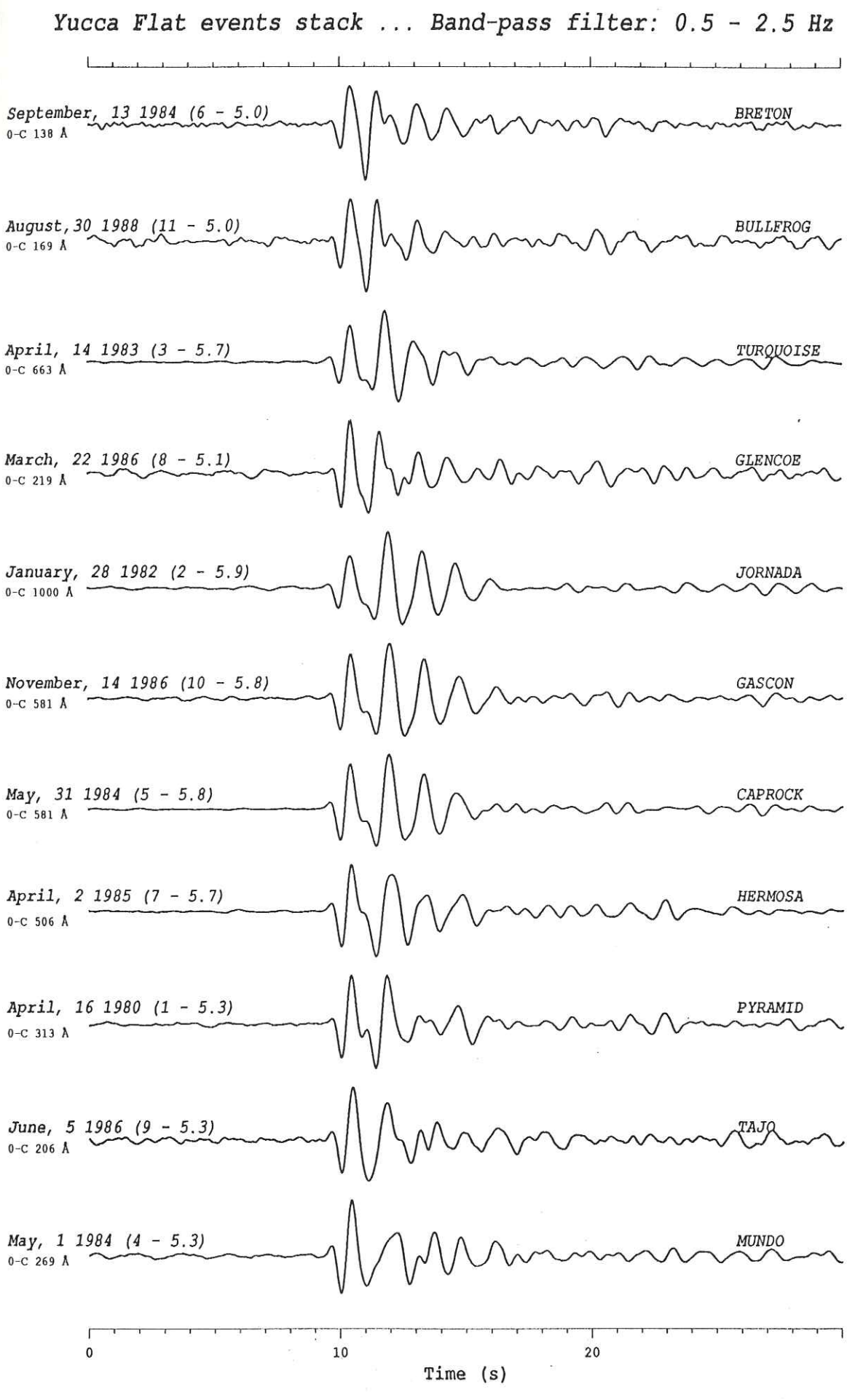
Yucca Flat events stack ... Band-pass filter: 0.5 - 2.5 Hz
September, 13 1984 (6 - 5.0)
0-C 138 A
BRETON
August, 30 1988 (11 - 5.0)
0-C 169 A
BULLFROG
April, 14 1983 (3 - 5.7)
0-C 663 A
TURQUOISE
March, 22 1986 (8 - 5.1)
0-C 219 A
GLENCOE
January, 28 1982 (2 - 5.9)
0-C 1000 A
JORNADA
November, 14 1986 (10 - 5.8)
0-C 581 A
GASCON
May, 31 1984 (5 - 5.8)
0-C 581 A
CAPROCK
April, 2 1985 (7 - 5.7)
0-C 506 A
HERMOSA
April, 16 1980 (1 - 5.3)
0-C 313 A
PYRAMID
June, 5 1986 (9 - 5.3)
0-C 206 A
TAJO
May, 1 1984 (4 - 5.3)
0-C 269 A
MUNDO
0
10
20
Time (s)

Fig.V.3

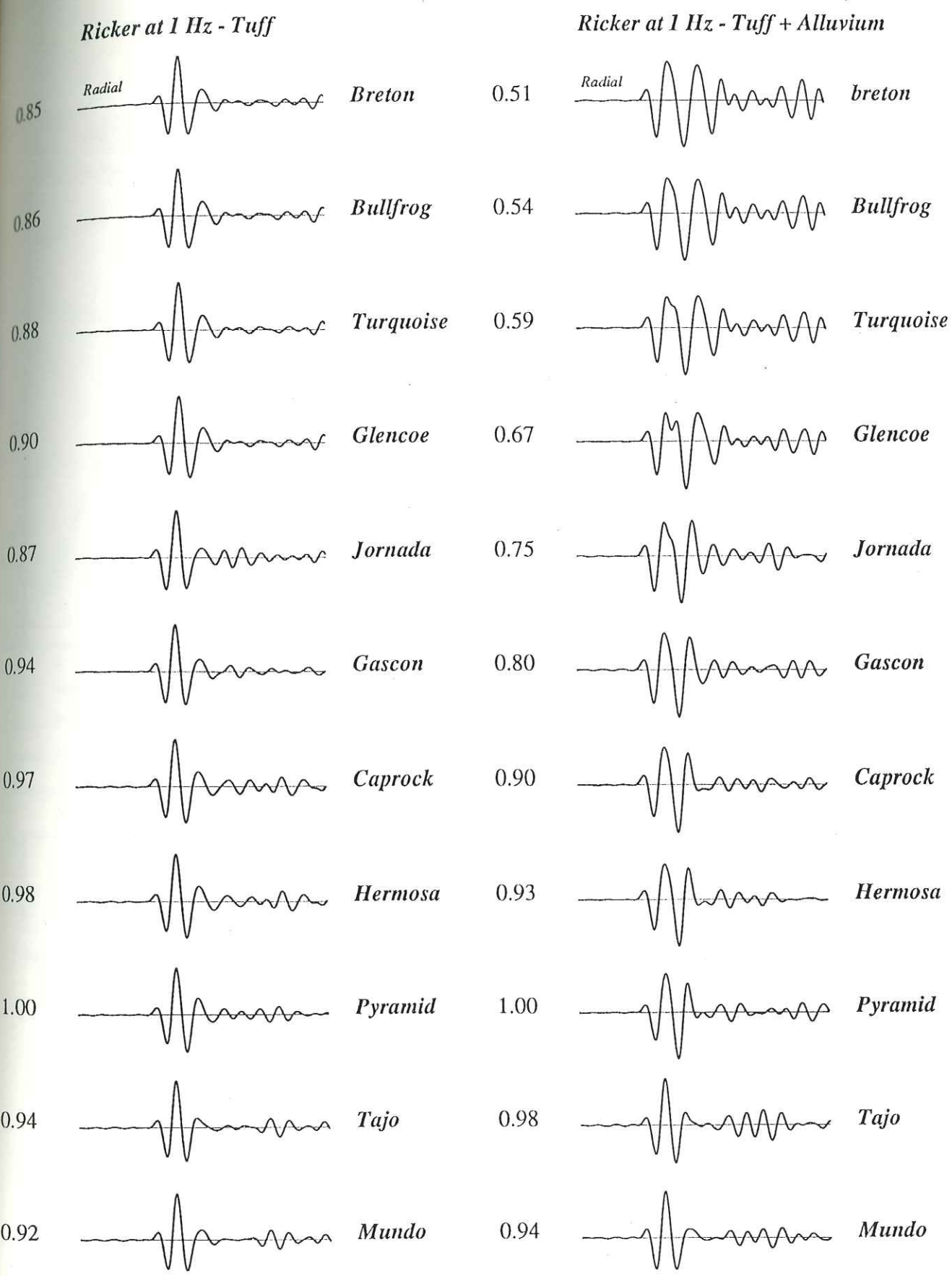

Fig. V.4 - Displays of the synthetic modellings obtained for the model *a* (left) and *b* (right) for the *11* studied detonations. The source is for both cases a Ricker having a *1* Hz central frequency in displacement. The relative amplitudes are written in the left side of each seismogram.

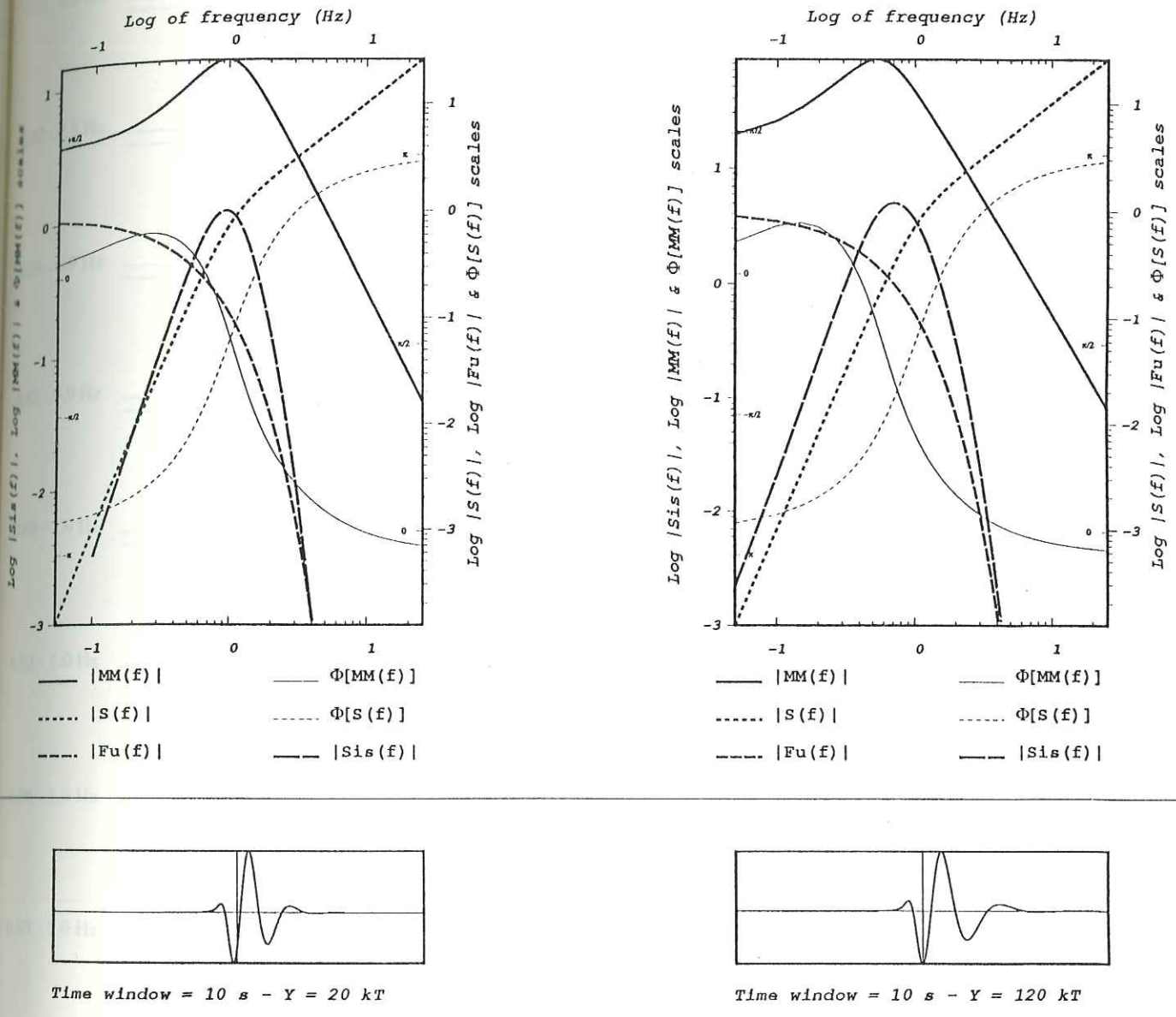

Fig. V.5 - The shapes of the Mueller-Murphy (1971) source that should be recorded at teleseismic distance in an infinite homogeneous space are given for the yields *20* kt and *120* kt in the two bottom boxes. In these boxes, the middle vertical thin line shows the arrival of the *1* Hz frequency. The transfert functions of the Mueller-Murphy (1971) source function (*i.e.* modulus $|MM(f)|$, phase $\Phi[MM(f)]$), of the Futterman (1962) mantle attenuation (*i.e.* modulus $|Fu(f)|$), of the recording system (*i.e.* modulus $|S(f)|$, phase $\Phi[S(f)]$), and of the far field displacement recording (*i.e.* modulus $|Sis(f)|$) are depicted in the top part of the display.

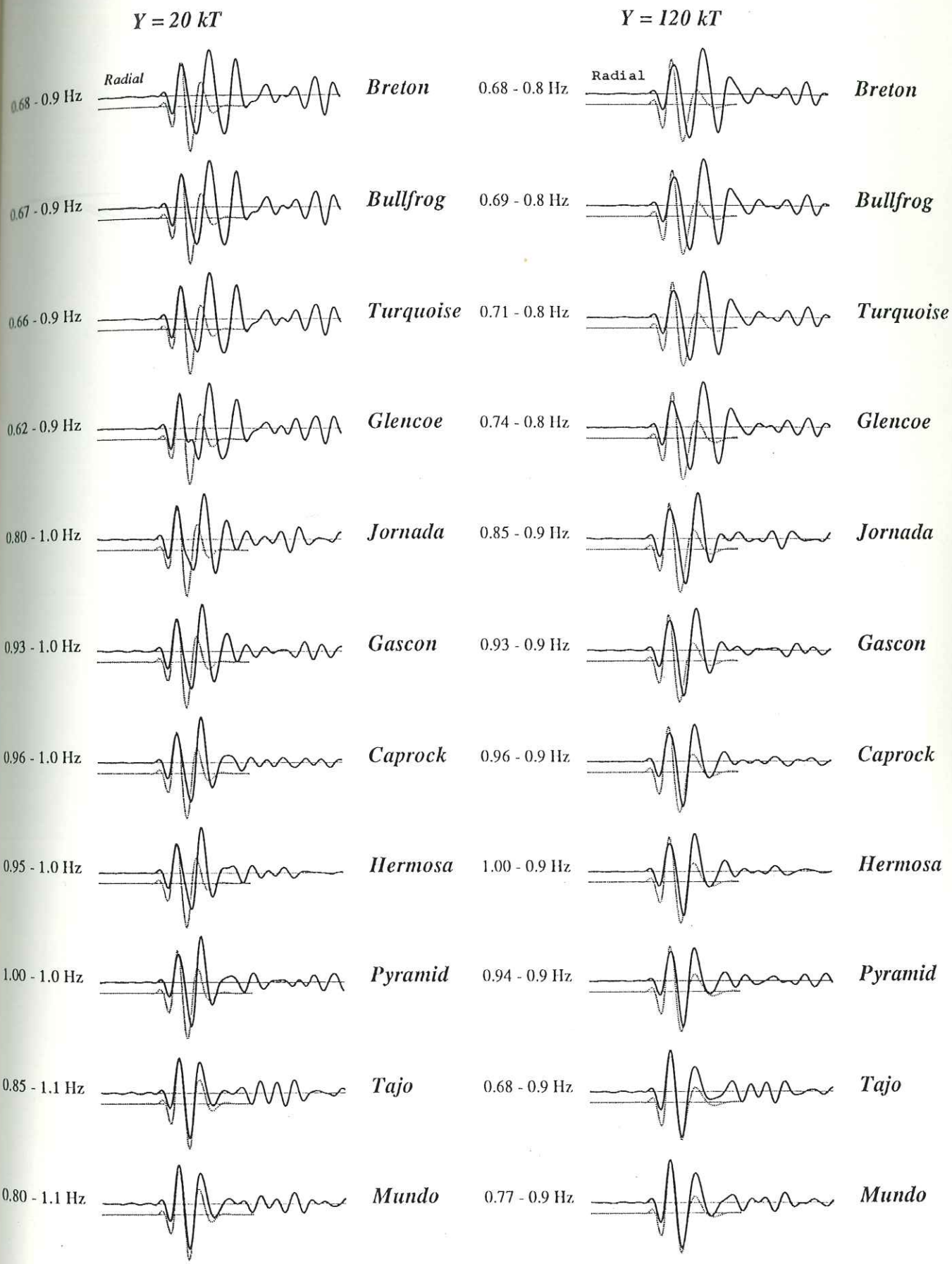

Fig. V.6 - Seismograms obtained for the Mueller-Murphy source (1971) and for the two yields *20* kt (left) and *120* kt (right). The relative amplitudes and their corresponding frequencies are written at the left of each seismogram. The seismograms are the ones calculated for the model *b*. The solutions obtained in a half space are given in slight superimposed dotted lines.

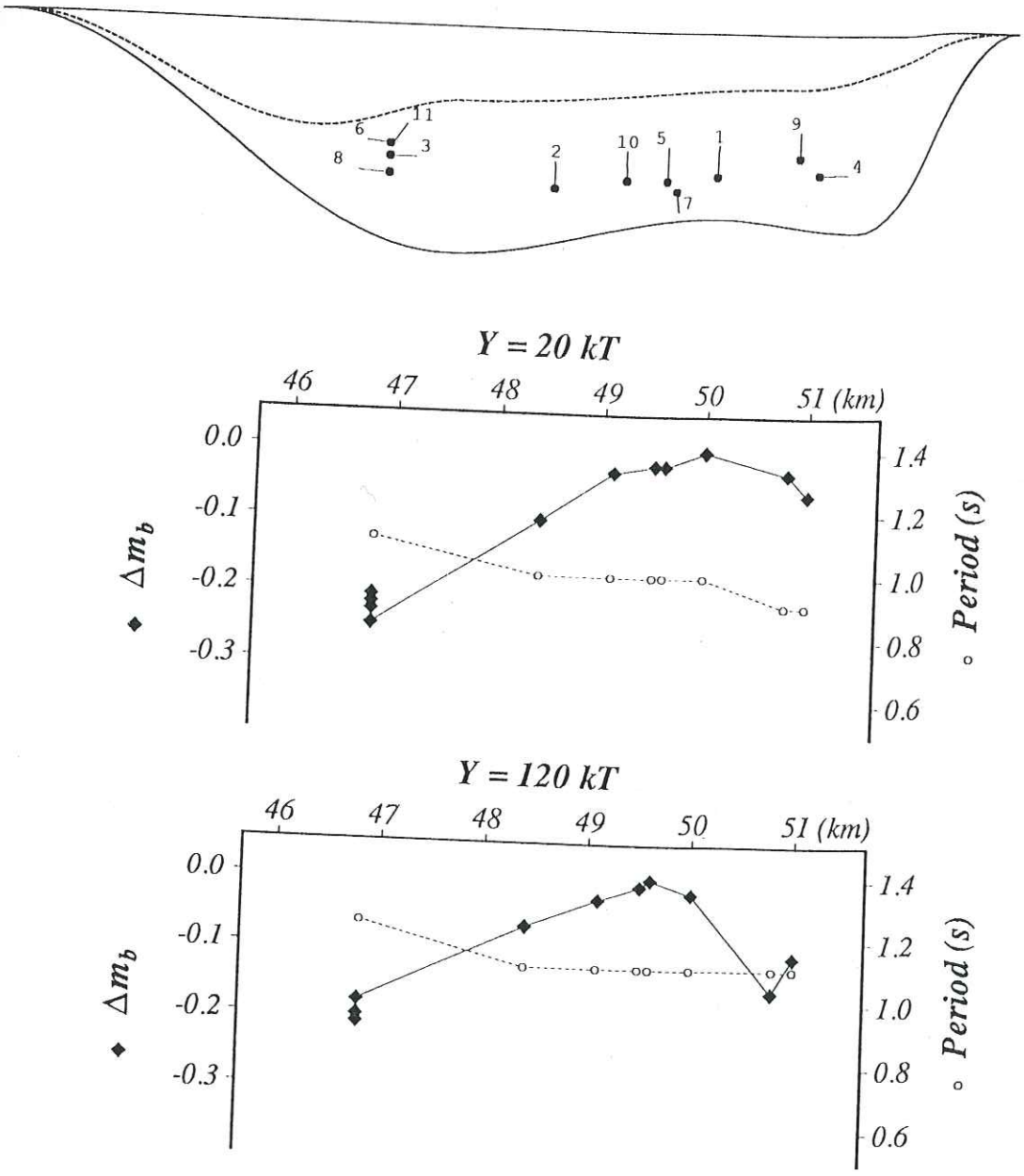

Fig.V.7 - Representation of the synthetic Δm_b predictions deduced from the calculations presented figure V.6. The geometrical configuration is given in the top of the figure. The Δm_b (black squares) and the frequencies (white circles) at which these variations have been computed are plotted for the yields *20* kt and *120* kt.

Perspectives

Au cours de ce travail, nous nous sommes attachés à présenter sur un ensemble de modèles simples, comment différentes altérations peuvent modifier les signaux sismiques en fonction des structures présentes dans les milieux de propagation. Le passage à des milieux plus complexes ne pose aucun problème théorique. Il faut cependant en explorer progressivement les structures si l'on veut continuer à expliquer les modifications des signaux en fonction de celles des modèles. Nous ne rappellerons pas ici de façon systématique les résultats obtenus, préférant définir un plan plus général, composé de deux parties, plan dans le déroulement duquel vient s'insérer cette thèse .

Applications • Nous avons vu combien l'estimation de l'énergie des tirs peut être faussée si l'on ne prend pas en compte l'influence à des distances télésismiques des structures environnant ces sources (*cf.* chapitre V). Il faut, de la même manière, tenir compte des sites de réception qui, eux aussi, peuvent amplifier ou atténuer les ondes reçues (*cf.* chapitre II). Pour corriger ces estimations, on pourra calculer les réponses d'une série de stations à des ondes planes qui viendraient de zones de tirs particulières. Pour chaque tir dont on connaîtra la géologie alentour, on pourra évaluer la réponse du site vue par chacune des stations. On disposera alors de tous les éléments pour analyser les variations de la source explosive réelle par rapport à la source ponctuelle isotrope utilisée pour le calcul. Le principe de ce traitement n'est pas nouveau, puisqu'il s'agit simplement de déconvoluer du signal toutes les informations que l'on peut connaître, mais les outils développés ici permettront d'effectuer ce traitement dans les milieux très hétérogènes.

Recherches • Les méthodes de calcul développées nous permettent dès maintenant d'envisager l'installation d'une génération de programmes bien adaptés au calcul de sismogrammes en champs proches et lointains pour des régions sources et réceptrices dont les structures 2D peuvent être très complexes et pour lesquelles on pourra tenir compte simultanément de la topographie et des structures sous-jacentes. Les études présentées jusqu'ici se sont limitées à l'utilisation de sources de type explosion ou onde plane. Nous avons pu ainsi par la simplicité de leurs diagrammes de radiations en distinguer les effets pour mieux analyser les champs diffractés sur les hétérogénéités.

Les méthodes développées ne sont pas pour autant limitées à ces seules sources. Ainsi, après avoir analysé pour des sources ponctuelles les différentes corrélations entre la forme des champs de déplacement (*resp.* de vitesses et d'accélérations), la position des sources et la géométrie des bassins, nous pouvons maintenant aborder la modélisation de sources étendues dans des milieux hétérogènes. Dès lors, les problèmes peuvent être classés en deux catégories: l'inversion des sources sismiques dont nous venons de décrire le principe et l'analyse du milieu de propagation pour en prédire la réponse lorsqu'il est sollicité par un champ d'onde donné.

La modélisation ne peut se priver de l'observation géophysique du terrain. Que ce soit pour l'étude du fonctionnement des sources qui impose de s'affranchir de la propagation ou que ce soit pour l'analyse et la prédiction des effets de sites: il faut donc absolument connaître et ce le plus précisément possible la structure des milieux de propagation. Nous soulignerons enfin l'apport essentiel de la simulation numérique qui permet d'expliquer les phénomènes induits sur les champs d'ondes par la diffraction tout en ayant le contrôle des modèles de propagation.

Bibliographie

Aki, K., M. Bouchon, and P. Reasenberg (1974). Seismic source for an underground nuclear explosion. *Bull. Seism. Soc. Am.* **64**, 131-148

Aki, K. and K. L. Larner (1970). Surface motion of a layered medium having an irregular interface due to incident plane *SH* waves. J. Geophys. Res. **75**, 933-954

Aki, K. and P. G. Richards (1980). *Quantitative Seismology: Theory and Methods.* **Vol. 1**, W. H. Freeman, San Fransisco, California, 557 pp

Bache, T. C. (1982). Estimating the yield of underground nuclear explosions. *Bull. Seism. Soc. Am.* **72**, S131-S168

Bard, P.-Y. (1982). Diffracted waves and displacement field over two-dimensional elevated topographies. *Geophys. J. Roy. astr. Soc.* **71**, 731-760

Bard, P.-Y. and M. Bouchon (1980a). The seismic response of sediment-filled valleys. Part 1. The case of incident *SH*-waves, *Bull. Seism. Soc. Am.* **70**, 1263-1286

Bard, P.-Y. and M. Bouchon (1980b). The seismic response of sediment-filled valleys. Part 2. The case of incident *P*- and *SV*-waves, *Bull. Seism. Soc. Am.* **70**, 1921-1941

Bard, P.-Y. and M. Bouchon (1985). The two-dimensional resonance of sediment-filled valleys. *Bull. Seism. Soc. Am.* **75**, 519-541

Bard, P.-Y. and J. C. Gariel (1986). The seismic response of two-dimensional sedimentary deposits with large vertical velocity gradients. *Bull. Seism. Soc. Am.* **76**, 343-366

Boardman, C. R., D. D. Rabb, and R. D. McArthur (1964). Responses of four rock mediums to contained nuclear explosions. *J. Geophys. Res.* **69**, 3457-3469

Boore, D. M. (1972). A note on the effect of simple topography on seismic *SH* waves. *Bull. Seism. Soc. Am.* **62**, 275-284

Bouchon, M. (1973). Effect of topography on surface motion. *Bull. Seism. Soc. Am.* **63**, 615-632

Bouchon, M. (1976). Teleseismic body wave radiation from a seismic source in a layered medium. *Geophys. J. Roy. astr. Soc.* **47**, 515-530

Bouchon, M. and K. Aki (1977). Discrete wave-number representation of seismic source wave fields. *Bull. Seism. Soc. Am.* **67**, 259-277

Bouchon, M. (1978). The importance of the surface or interface *P* wave in near-earthquake studies. *Bull. Seism. Soc. Am.* **68**, 1293-1311

Bouchon, M. (1985). A simple complete numerical solution to the problem of

diffraction of *SH* waves by an irregular surface. *J. Acoust. Soc. Am.* **77**, 1-5

Bouchon, M. (1987). Diffraction of elastic waves by cracks or cavities using the discrete wavenumber method. *J. Acoust. Soc. Am.* **81**, 1671-1676

Bouchon, M., M. Campillo, and S. Gaffet (1989). A boundary integral equation-discrete wavenumber representation method to study wave propagation in multilayered media having irregular interfaces, *Geophysics* **54**, 1134-1140

Campillo, M. (1987). Modeling of *SH*-wave propagation in an irregularly layered medium. Application to seismic profiles near a dome. *Geophys. Prosp.* **35**, 236-249

Campillo, M. (1987). L_g-wave propagation in a laterally varying crust and the distribution of the apparent quality factor in central France. *J. Geophys. Res.* **92**, 12604-12614

Campillo, M. and M. Bouchon (1985). Synthetic *SH* seismograms in a laterally varying medium by the discrete wavenumber method. *Geophys. J. Roy. astr. Soc.* **83**, 307-317

Cleary, J. R., D. W. Wing, and R. A. W. Haddon (1975). *P*-wave in the earth's crust and upper mantle. *Geophys. J.* **43**, 861-872

Closmann, P. J. (1969). On the prediction of cavity radius produced by an underground nuclear explosion. *J. Geophys. Res.* **74**, 3935-3939

Cormier, V. F. (1982). The effect of attenuation on seismic body waves. *Bull. Seism. Soc. Am.* **72**, S169-S200

Der, Z. A. and A. C. Lees (1985). Methodologies for estimating $t^*(f)$ from short period body waves and regional variations of $t^*(f)$ in the United States. *Geophys. J. Roy. astr. Soc.* **82**, 125-140

England, R., F. J. Sabina, and I. Herrera (1980). Scattering of *SH* waves by surface cavities of arbitrary shape using boundary methods. *Phys. Earth Planet. Inter.* **21**, 148-157

Ferguson, J. F. (1988). Body-wave magnitude variation at Yucca Flat, Nevada, *Bull. Seism. Soc. Am.* **78**, 863-872.

Ferguson, J. F., R. N. Felch, C. L. V. Aiken, J. S. Oldow, and H. Dockery (1988). Models of the Bouguer gravity and geologic structure at Yucca Flat, Nevada. *Geophysics* **53**, 231-244

Frasier, C. W. and J. Filson (1972). A direct measurement of earth's short-period attenuation along a teleseismic ray path. *J. Geophys. Res.* **77**, 3782-3787

Futterman, W. I. (1962). Dispersive body waves. *J. Geophys. Res.* **67**, 5279-5291

Gaffet, S. and M. Bouchon (1989). Effects of two-dimensional topographies using the discrete wavenumber-boundary integral equation method in *P-SV* cases, *J. Acoust. Soc. Am.* **85**, 2277-2283

Gaffet, S. and M. Bouchon (1990). Source location and boundary shape effects on the *P-SV* near displacement field using a boundary integral equation-discrete wavenumber representation method. *to be submitted for publication*

Hasegawa, H. S. (1971). Analysis of teleseismic signals from underground nuclear explosions originating in four geological environments. *Geophys. J. Roy. astr. Soc.* **24**, 365-381

Hasegawa, H. S. (1972). Analysis of amplitudes spectra of *P* waves earthquakes and underground explosions. *J. Geophys. Res.* **77**, 3081-3096

Haskell, N. A. (1953). The dispersion of surface waves in multilayered media. *Bull. Seism. Soc. Am.* **43**, 17-34

Haskell, N. A. (1967). Analytic approximation for the elastic radiation from a contained underground explosion. *J. Geophys. Res.* **72**, 2583-2587

Helmberger, D. V. and D. M. Hadley (1981). Seismic source functions and attenuation from local and teleseismic observations of the N. T. S. events JORUM and HANDLEY. *Bull. Seism. Soc. Am.* **71**, 51-67

Ilan, A. (1977). Finite-difference modelling for *P*-pulse propagation in elastic media with arbitrary polygonal surface. *J. Geophys.* **43**, 41-58

Johnson, L. R. (1988). Source characteristics of two underground nuclear explosions. *Geophys. J. Roy. astr. Soc.* **95**, 15-30

Kawase, H. (1988). Time-domain response of a semi-circular canyon for incident *SV*, *P*, and Rayleigh waves calculated by the discrete wavenumber boundary element method. *Bull. Seism. Soc. Am.* **78**, 1415-1437

Kawase, H. and K. Aki (1989). A study on the response of a soft basin for incident *S*, *P*, and Rayleigh waves with special reference to the long duration observed in Mexico city. *Bull. Seism. Soc. Am.* **79**, 1361-1382

Key, F. A. (1967). Signal generated noise recorded at the Eskdalemuir seismometer array station. *Bull. Seism. Soc. Am.* **57**, 27-37

Lamb, H. (1904). On the propagations of tremors at the surface of an elastic solid. *Phil. Trans. Roy. Soc. London Ser.* **A203**, 1-42

Lapwood, E. R. (1949). The disturbance due to a line source in a semi-infinite elastic medium. *Phil. Trans. Roy. Soc. London Ser.* **A242**, 63-100

Latter, A. L., R. E. Lelevier, E. A. Martinelli, and W. G. McMillan (1961). A

method of concealing underground nuclear explosions. *J. Geophys. Res.* **66**, 943-946

Lay, T. (1987a). Analysis of near-source contributions to early *P*-wave coda for underground explosions. II. Frequency dependence. *Bull. Seism. Soc. Am.* **77**, 1252-1273

Lay, T. (1987b). Analysis of near-source contributions to early *P*-wave coda for underground explosions. III. Inversion for isotropic scatterers. *Bull. Seism. Soc. Am.* **77**, 1767-1783

Lay, T. and J. L. Welc (1987). Analysis of near-source contributions to early *P*-wave coda for underground explosions. I. Waveform complexity. *Bull. Seism. Soc. Am.* **77**, 1017-1040

Lemenager, C. (1982). Applications de techniques numériques du traitement du signal à la sismologie. *Thèse D. I., Paris VI*, 150pp

McLaughlin, K. L., L. M. Anderson, and A. C. Lees (1987). Effects of local geologic structures on Yucca Flat, Nevada Test Site, explosion waveforms: two dimensional linear finite difference simulations. *Bull. Seism. Soc. Am.* **77**, 1211-1222

McLaughlin, K. L. and R.-S. Jih (1988). Scattering from near source topography: teleseismic observations and numerical simulations. *Bull. Seism. Soc. Am.* **78**, 1399-1414

Mueller, R. A. and J. R. Murphy (1971). Seismic characteristics of underground nuclear detonations. Part I: seismic spectrum scaling. *Bull. Seism. Soc. Am.* **61**, 1675-1692

Murphy, J. R. (1972). Calculated compressional-wave arrivals from underground nuclear detonations. *Bull. Seism. Soc. Am.* **62**, 991-1016

Murphy, J. R. (1977). Seismic source functions and magnitude determinations for underground detonations. *Bull. Seism. Soc. Am.* **67**, 135-158

Murphy, J. R. and R. A. Mueller (1971). Seismic characteristics of underground nuclear detonations. Part II: elastic energy and magnitude determinations. *Bull. Seism. Soc. Am.* **61**, 1693-1704

Orphal, D. L. (1970). The cavity formed by a contained underground nuclear detonation. *Report* NVO-1163-TM-15, Environmental Research Corporation

Paul, A. and M. Campillo (1988). Diffraction and conversion of elastic waves at a corrugated interface. *Geophysics* **53**, 1415-1424

Pho, H.-T. and L. Behe (1972). Extended distances and angles of incidence of *P* waves. *Bull. Seism. Soc. Am.* **62**, 885-902

Peek, R. and E. Kausel (1983). Discussion of scattering of *SH* waves by subsurface

topography. *J. Eng. Mech. Div.*, **ASCE**, 932-934

Power, F. W. (1974). Inelastic calculations in tuff and spectrum scaling considerations. *Report* NVO-1163-241, Environmental Research Corporation

Sánchez-Sesma, F. J., F. J. Chávez-García, and M. A. Bravo (1988). Seismic response of a class of alluvial valleys for incident *SH* waves. *Bull. Seism. Soc. Am.* **78**, 83-95.

Sánchez-Sesma, F. J. and J. A. Esquivel (1979). Ground motion on alluvial valleys under incident plane *SH* waves. *Bull. Seism. Soc. Am.* **69**, 1107-1120

Sánchez-Sesma, F. J. and E. Rosenblueth (1979). Ground motion at canyons of arbitrary shape under incident *SH* waves. *Int. J. Earthquake Eng. Struct. Dyn.* **7**, 441-450

Sánchez-Sesma, F. J. (1981). A boundary method applied to elastic scattering problems. *Arch. Mech.* **33**, 167-179

Sánchez-Sesma, F. J., I. Herrera, and J. Aviles (1982). A boundary method for elastic wave diffraction. Application to scattering of *SH* waves by surface irregularities. *Bull. Seism. Soc. Am.* **72**, 473-490

Shah, A. H., K. C. Wong and S. K. Datta (1982). Diffraction of plane *SH* waves in a half-space. *Int. J. Earthquake Eng. Struct. Dyn.* **10**, 519-528

Sills, L. B. (1978). Scattering of horizontally polarized shear waves by surface irregularities. *Geophys. J. Roy. astr. Soc.* **54**, 319-348

Smith, W. D. (1975). The application of finite element analysis to body wave propagation problems. *Geophys. J. Roy. astr. Soc.* **42**, 747-768

Taylor, S. R. (1983). Three-dimensional crust and upper mantle structure at the Nevada Test Site. *J. Geophys. Res.* **88**, 2220-2232

Thomson, W. T. (1950). Transmission of elastic waves through the stratified solid medium. *J. Appl. Phys.* **21**, 89-93

Tucker, B. E. and J. L. King (1984). Dependence of sediment-filled valley response on input amplitude and valley properties. *Bull. Seism. Soc. Am.* **74**, 153-165

Tucker, B. E., J. L. King, D. Hatzfeld, and I. L. Nersesov (1984). Observations of hard-rock site effects. *Bull. Seism. Soc. Am.* **74**, 121-136

Viecelli, J. A. (1973). Spallation and the generation of surface waves by an underground explosion. *J. Geophys. Res.* **78**,2475-2487

von Seggern, D. H. and R. Blandford (1972). Source time functions and spectra for underground nuclear explosions. *Geophys. J.* **31**, 83-98

Werth, G. C. and R. F. Herbst (1963). Comparisons of amplitudes of seismic waves

from nuclear explosions in four medium. *J. Geophys. Res.* **68**, 1463-1475

Wong, H. L. and P. C. Jennings (1975). Effect of canyon topographies on strong ground motion. *Bull. Seism. Soc. Am.* **65**, 1239-1257

Zahradnik, J. and L. Urban (1984). Effect of a simple mountain range on underground seismic motion. *Geophys. J. Roy. astr. Soc.* **79**, 167-183

THÈSE de DOCTORAT
de l'UNIVERSITÉ JOSEPH FOURIER
de GRENOBLE

Titre de l'ouvrage:

SIMULATION DES MOUVEMENTS DU SOL À DISTANCES RÉGIONALES ET TÉLÉSISMIQUES EN MILIEU HÉTÉROGÈNE - MÉTHODE ET APPLICATIONS -

Nom de l'auteur: **Stéphane GAFFET**

Établissements:

- Observatoire de Grenoble et Institut de Recherches Interdisciplinaires de Géologie et de Mécanique.
- Laboratoire de Détection et de Géophysique du Commissariat à l'Energie Atomique de Bruyères-le-Chatel.

RÉSUMÉ

Une formulation détaillée de la méthode de représentation des champs d'ondes sismiques, est donnée dans les cas *P*, *SV*, et *SH*, pour des milieux 2D dont la stratification est formée de couches latéralement irrégulières. Cette représentation est basée sur l'échantillonnage de l'espace des nombres d'onde et sur la résolution des conditions aux limites des champs de contraintes et de déplacements aux différentes interfaces. Cette méthode est appliquée au calcul des mouvements du sol à des distances de quelques kilomètres de la source et, à l'aide du théorème de réciprocité, à la simulation de ces mouvements pour des distances télésismiques.

L'influence des différentes structures géologiques (*e.g.* topographies irrégulières, bassins sédimentaires) est mise en évidence sur les amplifications et les atténuations des déplacements du sol. Les effets produits sur les champs de déplacements sont analysés en fonction de la position de la source par rapport aux irrégularités du milieu de propagation. Les variations de ces effets sont également étudiées lorsque l'on change la forme des hétérogénéités.

Sont étudiés à distances régionales: un mécanisme de défocalisation de l'énergie sur une structure anticlinale, l'allongement de la durée des mouvements du sol par rétropropagation des champs d'ondes dans un bassin sédimentaire, l'influence de la raideur des reliefs et de la profondeur de la source sur les champs d'ondes diffractés par un explosion. A distances télésismiques, une étude est menée qui précise l'incidence des structures hétérogènes se trouvant dans la région de la source, sur l'estimation de la magnitude.

MOTS-CLÉS

sismologie; sismogramme synthétique; explosion; diffraction; amplifications; onde de surface; effet de site; influence régionale; influence télésismique.